POLITECNICO
MILANO 1863

POLITECNICO DI MILANO
DEPARTMENT OF ELECTRONICS, INFORMATION AND BIOENGINEERING
DOCTORAL PROGRAMME IN BIOENGINEERING

XXIX CYCLE

CONE BEAM CT AND PROTON CT FOR ADAPTIVE RADIO AND PROTON THERAPY

Doctoral Dissertation of:
F. Roberto Cassetta Jr.

Advisors:
Professor Guido Baroni and Marco Riboldi

External Advisor:
Professor Jef Vandemeulebroucke

Tutor:
Professor Gabriele Dubini

2017

Para meus pais.

To my parents.

Acknowledgments

This work has been funded by the grant 9374/13-2 of Coordenação de Aperfeiçoamento de Pessoal de Nível Superior(CAPES).

I would like to express the deepest appreciation to my two main supervisors Professor Marco Riboldi and Professor Guido Baroni. To Professor Marco Riboldi for all the patience and support throughout these years. To Professor Guido Baroni for giving me the greatest opportunity of my life so far.

I cannot express how much I am grateful for all the teaching and opportunities given by professor Reinhard Schulte, one of the most brilliant and influent professionals I could have ever met.

I appreciate and acknowledge all the help given by professor Marco Schwarz, Dr. Paulo Novaes, Kleber Leandro, the staff of Hospital Vitória (Santos-Brazil) and Hospital Albert Einstein (São Paulo-Brazil). I would like to thank my colleagues Pierluigi Piersimoni, Giovanni Fattori, Marta Dias among others who shared their time and knowledge to push me forward.

Thanks to my friends and those who did not contribute directly to my work but were supporting me and making my life more cheerful.

Finally, to my family. Às minha irmãs, pela torcida e por acreditarem em meu sucesso. Aos meus pais, sem dúvida as pessoas mais importantes da minha vida. Espero sempre poder recompensar todos os sacrífícios que fizeram por mim.

Contents

List of Figures

List of Tables

Abstract

Introduction: Continuous technological developments in radio and proton therapy create new and better solutions for cancer treatment. The introduction of new image-guidance and adaptive therapy methods requires extreme caution and extensive verification should be made, accounting for expected results, possible gains over induced damage and implementation challenges.

Methods: This work is focused on image-guidance methods in radio and proton therapy, with specific emphasis on anatomical changes on patients during treatment. Automated image registration methods have been implemented and validated, in order to show the full potential of CBCT image registration. Geometric and dosimetric verification has been carried out, thus checking the feasibility of treatment adaptation relying on automated image registration. In addition, proton CT is investigated and verified as a low-dose method for patient positioning in proton therapy.

Results: Deformable image registration (DIR) followed by dose recalculation was evaluated for prostate cancer patients. Variations in patient anatomy were estimated (distances measured between landmarks) and corrected with DIR, resulting in a mean landmarks distance reduction from 3,79 to 2,00 mm. In 8 out of 9 patients an increase in rectum dose was observed, where, for 3 of them, important constraints of dose/volume were violated, which could result in acute reaction on patients? organs at risk. The proposed automatic contour propagation method by means of DIR was tested in rectal cancer patients, treated with proton therapy, where repeated in-room CTs were available. The DIR validations for these patients were carried out relying also on dose comparison.

The gamma test presented an improvement on the pass fraction, on the most critical case, from 88,40% to 99,87%. The automatically generated contours required only few corrections which, nevertheless, would have small influence on final DVH for online analysis. The implementation of adaptive strategies would collaborate for healthy organs sparing and PTV coverage verification. Low-dose positioning methods with proton CT images were evaluated and a reduction of up to 55 times in comparison to a conventional CBCT was obtained. Proton CT images were demonstrated to be suitable for image registration at sub-millimeter confidence in patient positioning.

Discussion: Image registration algorithms based on open-source libraries were developed and tested for the realization of adaptive therapy strategies. The proposed methods facilitate daily dose calculation and plan verification (online or offline), thus providing higher precision and effectiveness of the treatment.

Summary

THIS PhD thesis presents an overview, in 6 chapters, of common methods used for patient positioning, evaluates them and proposes new strategies for image-guidance and adaptive radio and proton therapy.

The first chapter is an introduction and motivation for particle therapy, mentioning favorable points and difficulties for proton therapy expansion. The basic clinical workflow is described, including proton therapy planning (proton interactions with matter basic formulas included), patient positioning, image registration and sources of uncertainty during the whole process. The expected method for patient imaging, proton CT, is summarized.

The second chapter evaluates currently used methods for image registration. Technological limitations of some widely used methods are discussed, then each one is tested and their possibilities discussed aiming at the best possible usage. A hypofractionation protocol for prostate elderly patients was tested first. The main idea was to verify the applied corrections provided by ExacTrac to ensure precision in patient setup and allow reduced PTV margins for hypofractionated radiotherapy treatment. Orthogonal projections combined with optical tracking system were verified for patient positioning for head and neck proton therapy patients from CNAO (Pavia-IT). The usefulness of optical tracking system implementation was discussed. Rigid registration for CT-CBCT pairs were tested for the C-arm CBCT machine installed at CNAO. Phantom CBCT images were transformed with 32 misplacement vectors, combining translations and rotations, and an in-house developed software was

tested for initial position recovery. Also, an algorithm for deformable image registration between limited field of view CBCT and CT was tested for prostate patients.

The third chapter introduces the adaptive radio and proton therapy concept. The main idea is to discuss and develop strategies to take into account anatomy changes in patients and evaluate if the treatment plan is still adequate. The first part is dedicated to prostate patients. A CBCT-CT deformable image registration algorithm was developed to create a planning CT with updated anatomy (virtual CT) and propagated contours. Treatment plans for photons and protons were created and recalculated over obtained virtual CTs to estimate what could happen in a real scenario, where structural changes in patients? bodies occur and a new dose distribution is obtained. The second part proposes the use of deformable image registration for contour propagation to be used on CT-on-rail of rectum patients on proton therapy. The efficiency of the deformable image registration method was evaluated by recalculating the dose over the virtual CT and comparing it to the dose obtained on the Ct-on-rail. The comparisons were done with gamma index measurements.

The fourth chapter discusses image processing and registration algorithms for proton CT. Pre and post processing methods for this new modality of imaging, still at an experimental stage, were tested aiming image quality improvement.

On the fifth chapter proton CT images, with different dose levels, were tested for patient positioning simulations, using two different developed algorithms for rigid and deformable image registration of a pediatric head phantom.

The last chapter discuss the results shown on this thesis and presents ideas to be developed in the future.

CHAPTER 1

Introduction and motivation for particle therapy

1.1 Cancer and particle therapy overview

Cancer is a generic name for various kinds of diseases, also known as tumor or neoplasm, whose main characteristic is the rapid growth of abnormal cells within the body. Such a growth may disrupt vital functions and also spread to other regions, a process known as metastasis, which is an aggravating fact that leads many patients to death. Cancer is one of the major causes of death worldwide, in 2015 it was associated with 8.8 million cases, which is about 17% of all deaths that year. In 2012, 14 million new cases of cancer were diagnosed worldwide [WHO17].

The process begins with a single cell, which goes through several stages of transformation to become a cancer cell. These changes may occur due to the interaction of genetic factors of the individual with some external agents, such as radiation (damage processes and cellular DNA repair can be seen in detail in the work of Alpen [Alp90]); tobacco smoke components; water and food contaminants; and some viruses, bacteria or parasites. Aging is also a factor that increases the risk of developing

the disease, in addition to pre-existing risks and less effectiveness in the cellular repair process (World Health Organization). Unhealthy lifestyle can also contribute to an increased risk of cancer.

Radiation therapy is an important modality of cancer treatment alongside surgery and chemotherapy. The main focus of this modality is the local control of the primary tumor. Treatment with ionizing radiation has been refined since its first use in the early twentieth century. It is important to find ways to reduce excess dose to the patient, so physicians and physicists evaluate the best way to conduct the prescribed treatment, relying on accurate treatment planning. This planning process aims at optimizing patient positioning and compensation techniques in order to reduce dose deposition in healthy tissues [HBS12a, HBS12b, BYWW$^+$12, MST$^+$11].

Cancer treatment with accelerated particles has brought very promising results, especially for sparing critical structures adjacent to the tumor, mostly for eyes, brain and spinal canal due to the beam conformality and its null exit dose [NHP$^+$12, LDU$^+$04, LHS$^+$00, Mah14, SLM$^+$14, FND$^+$15, MHN$^+$14, RCZ$^+$14]. But it should be noted that a great effort is required to achieve accurate dose delivery, due to uncertainties in the particle track inside the patient and in the final dose depth deposition.

With particle therapy improvements, an increase in the quality of life of the patients is expected, especially for pediatric patients, in which later side effects, as secondary malignancies and susceptibility to radiation on their growing organs, could affect their development [YSF$^+$05, RDM$^+$12, KKA$^+$07, RT14, CYM$^+$14]. This modality of therapy is not yet widely spread as the conventional radiotherapy with photons, although it has been experiencing a significant growth in the last decade as seen in figure 1.1.

The therapy with heavy charged particles is known to present better dose distribution and confinement in the volume of the tumor compared to conventional radiotherapy, thus better sparing patient structures around the lesion [SDG$^+$10]. One special feature of heavy charged particle beams is the fact that, compared to conventional radiotherapy, they have a reduced entrance dose, which implies reduced ionization in the tissues located before the region to be treated (Figure 1.2) and an almost

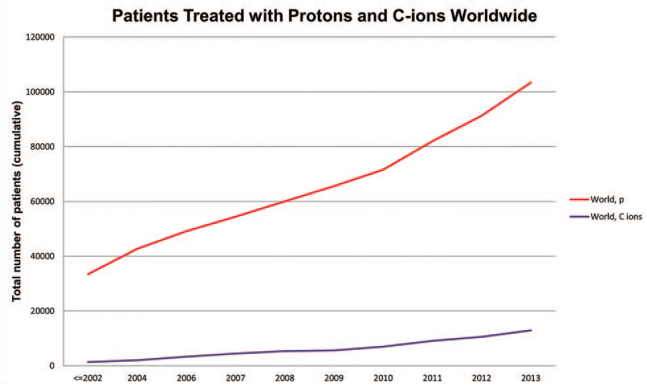

Figure 1.1: *Particle Therapy treatments growth over the last decade (adapted from: [Jer14]).*

immediate dose deposition going to zero.

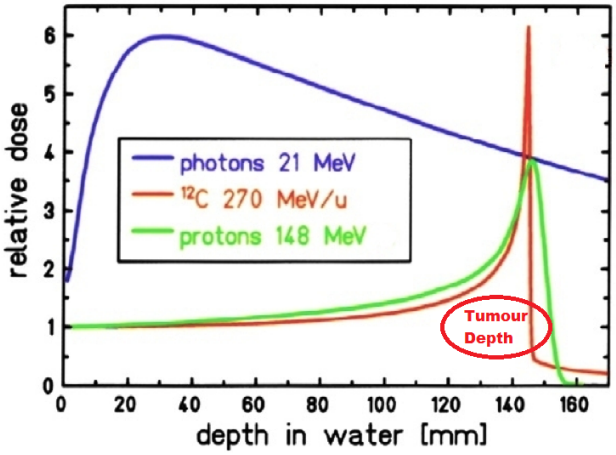

Figure 1.2: *Dose comparison among beam types. Adapted from [FKAEC09].*

1.1.1 Clinical applications

Even if constant advances in radiotherapy have been decreasing the disparity between photon and protons treatment results, these advances encounter an intrinsic limitation due to photon physical properties and can be overcome with advancements in proton therapy techniques [Pag12]. The reported benefits related to proton therapy, which is the most widespread type of treatment with accelerated particles, are significant. Those benefits become even more relevant when analyzing the reduction of side effects and improvement of the quality of life in pediatric patients, since

those are more likely to develop secondary malignancies and organ growth and function might be compromised by excessive dose [Buc15,LDU+04, HUG04,LHS+00,YSF+05,RDM+12,KKA+07,NHP+12]. Therefore the reduction of the integral dose obtained with particle therapy contributes to stochastic effects reduction.

For male adults, the most common type of cancer treated with proton therapy in the United States is prostate cancer. A comparison between uniform scanning proton therapy (USPT) and volumetric modulated arc therapy (VMAT) shows that the former performs significantly better at sparing adjacent regions like rectum and bladder compared to the latter, for the same covered planning target volume (PTV) region [RCZ+14, PMC+13]. Intra-ocular malignancies present good response to proton therapy as well. Those can be treated either by brachytherapy or external beam radiotherapy. Other factors like tumor region, treatment availability and medical experience might be considered before deciding the treatment course.

The target dose conformity is improved for particle therapy, thus for head and neck patients the integral dose will most likely be considerably reduced, avoiding giving dose to most important structures of the patient (figure 1.3). For malignancies such as medulloblastoma, a craniospinal irradiation is often used and irradiating a large extension of the patient tissues could result in severe effects if treated with conventional radiotherapy instead of particles [SAB+04, LBF+05, FRO09].

With constant techniques development, good results can be obtained with different treatment modalities, and the physicians can evaluate whether a method is more suitable than other for each situation [GHG+14], as for prostate patients where the toxicity and overall results of treating with protons or photons might be equivalent for most cases. Even if protons and carbon ions are known for good dose distribution and beam conformality, carbons ions are preferred to treat photon-resistant tumors due their high-linear energy transfer radiation characteristics [SKB+14, DFIF14].

The elevated cost of the equipment [WS01] and its maintenance is one of the limiting factors of wider availability of this form of treatment. The accelerator generally takes more physical space, because the linear accel-

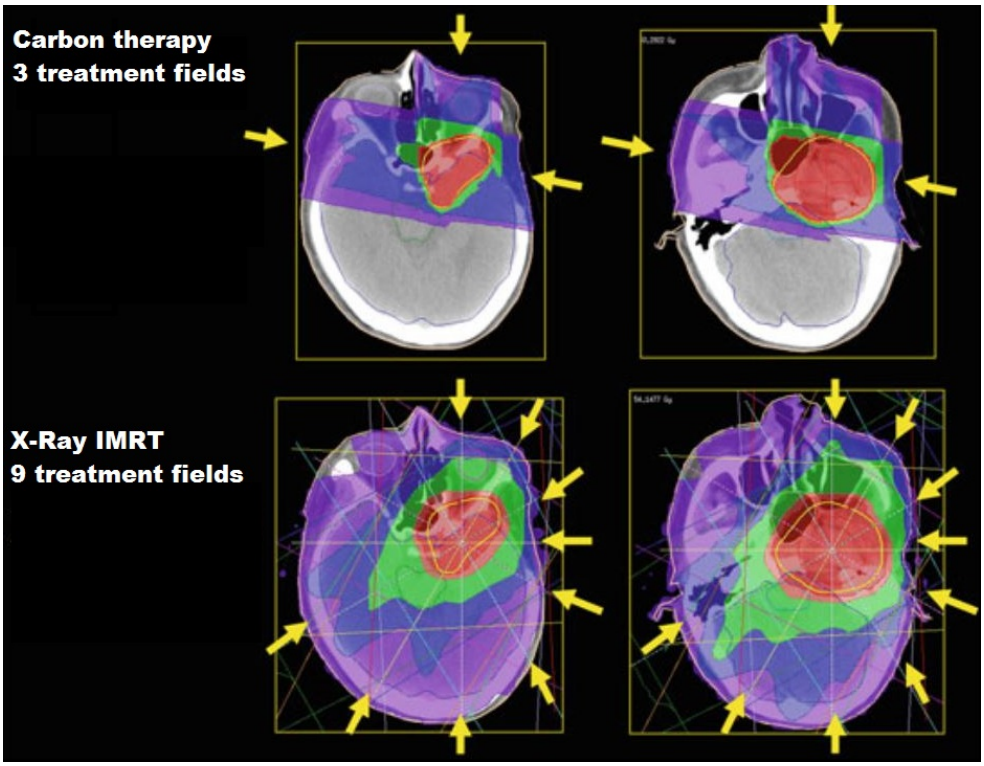

Figure 1.3: *Example of dose distribution comparison among carbon ion therapy and X-ray radiotherapy. Figure adapted from [TKSN14].*

erators currently used in radiotherapy with photons and electrons do not provide a sufficiently strong electric field to accelerate heavy particles and occupy adequate space for clinical use. A single particle accelerator is able to send treatment beams to different rooms, which are deflected by magnetic fields and electronic security systems that guarantee admission only when necessary, and a loss of intensity during transportation may be up to 5 % according to Khan [KHA09].

The absence or even the elevated costs of beam time of high energy particle accelerators demand studies mainly based on computer simulations. There are codes for simulations with accelerated particles available at CERN, prepared especially for GEANT4 (Geometry and Tracking) [AAA$^+$03, FS04, ZP08] and FLUKA [BCC$^+$14], which allow simulations of heavy particles interactions with matter and obtaining results for specific studies before experimental procedures and prototypes modeling.

1.1.2 Treatment planning in proton therapy

Due to the nature of heavy charged particles, it is observed that the lower the particle speed, the greater the energy transfer to the patient tissue. Thus there is higher energy deposit in the region located at the maximum range of the beam, when it is completely stopped by the medium. This dose peak around the maximum reach of the beam is known as the Bragg peak. Due to lower interaction of heavy charged particles with matter when they have high kinetic energy, it is possible to spare healthy regions proximal to the tumor.

The treatment planning procedure aims at the most suitable way to deliver the prescribed dose to the tumor. A combination of different energies (different depths of the Bragg peak) is intended to cover this region, i.e. the treatment beam maximum range is restricted to the tumor position. The sharp dose fall-off will be determinant for not affecting regions beyond the cancer cells extension, as does the photon treatment (Figure 1.4), therefore possibly minimizing future sequels [BC04].

Dose calculations are based on patient data structures, which are rescaled based on the water equivalent path, which is the amount of water that

would present the same energy loss for the treatment beam [GRE11]. The dose is then calculated by integrating the stopping power in the direction of an infinitesimal proton beam [PET92].

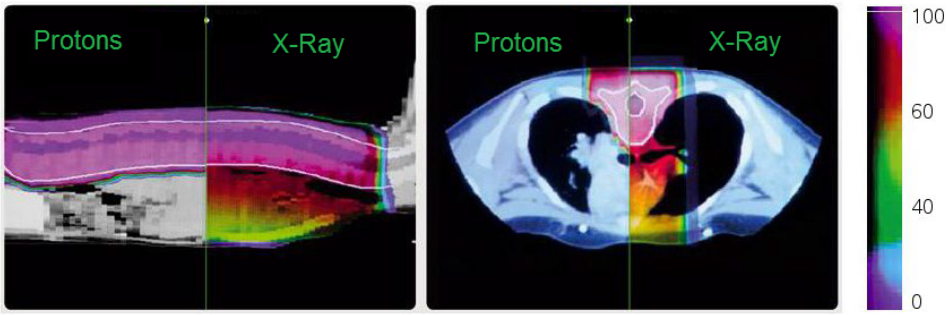

Figure 1.4: *Comparison of absorbed dose for X-ray and protons by a pediatric patient in treatment planning stage. Adapted from [GRE11]*

With images obtained from the patient, the equivalent thickness of water for each beam is calculated, which would be the amount of water that would have the same response to radiation as the human tissue to be treated [Pag12].

Proton therapy allows dose delivery in a sensitive region sparing important structures of the patient, because it requires fewer radiation fields, in addition to small dose deposition before the tumor [NHP+12] and this energy deposit in the tissues rapidly decreases to zero after the Bragg peak. By penetrating the patient, the amount of deposited dose depends on the initial energy of the beam, as protons only have great interaction with the decrease of their speed; this initial dose deposition will be reduced for high energy beams. High energetic protons, with long range, give rise to broader and low intensity Bragg peaks [CJCOA11].

The treatment planning for proton therapy must be based on images that show the detailed stopping power of the region. According to Wang et al. [WMT12], the conversion in stopping power from conventional computed tomography (CT) could result in errors around 3% in the calculation of the range of protons in the calibration process. This is due to the dependence of Z and Z/A of the photon and proton in their interactions, making the relationship between Hounsfield Units and RSP (relative stopping power) not constant. According to Penfold [PSM+10],

one can search for solutions to this problem by proposing the direct analysis of the proton beam. This author proposes a method for beam path prediction when traversing the matter called most likely path. The MLP (Most Likely Path) uses the trajectory of each particle as line integral for obtaining efficient algorithms to be used in the reconstruction of tomographic images acquired with proton beams. As seen in the work of Paganetti [Pag12], during the treatment planning, uncertainties in the range of the beam usually vary about $\pm$ 1.3 mm.

The treatment plan goes typically under quality check procedures by means of direct dose measurement in a phantom (figure 1.5). These measurements are compared with the planned dose estimation before starting the treatment.

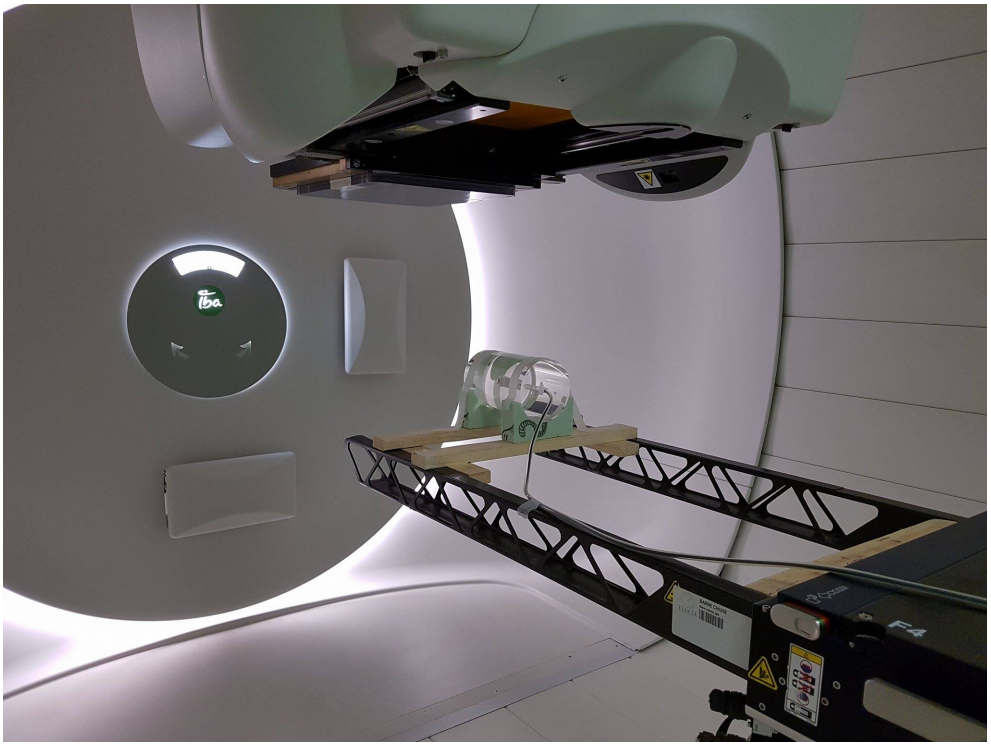

Figure 1.5: *Example of quality check for proton treatment. Image from Proton Therapy Centre (PTC) Trento Hospital*

Planning the treatment is an essential part of the therapy for optimizing the tumor irradiation process and sparing adjacent healthy tissues. One must seek the best possible plan given the limitations of the equipment, and clinical conditions of the patient.

1.2 Heavy charged particles interaction with matter

When traveling through tissues, the heavy particle beam will interact mostly with electrons through Coulomb force (Multiple Coulomb Scattering) (a complete theory can be seen in [MOL47] and [DEA94]). Collisions with target nuclei are possible, although less frequent. The probability of interactions with the nuclei compared to the probability of ionizing interactions is smaller than 5% for a 50 MeV beam of protons penetrating into a water target, and this value goes lower than 1% when the beam energy is increased to 200 MeV [FS04]. These interactions are considered to be just a small portion of the total electromagnetic interplay.

The cross section, i.e. the effective area of interaction between the particles, is used to determine the linear energy transfer to the tissue according to the beam penetration. The differential angular distribution of cross section related to the energy of the electrons ejected obeys the Rutherford principle for small angles, which means that the variation of the effective shock area in relation to the kinetic energy of electrons accelerated by interactions follows Rutherford's theory (equation 1.1).

$$d\sigma/dT \approx 1/\theta^4 \tag{1.1}$$

- σ ionization cross section
- T kinetic energy of ejected electron
- θ scattering angle of electron

The inelastic collisions in which the heavy particles transfer part of its kinetic energy to the electrons produce ionization and excitation in atoms: these processes are the most responsible for energy deposition in the tissues of the patient. This deposited energy by the incident beam is known as dose, and it is estimated and prescribed for cancer treatment.

The previously mentioned collisions are the main responsible in the heavy particle slowing down process, which may lead to secondary electrons production. The charge transfer occurs when a proton acquires an electron of the medium, and then the formed hydrogen can dissociate and ionize its surroundings [CSZ$^+$09].

For being heavier than the electrons, particle beams are scattered in

smaller angles, thus maintaining a more concise footprint. This beam transfers part of its energy (E) along the traversed path (x), which can be calculated in the form of LET (linear energy transfer) [KHA09]. This capacity of the medium to slow down the beam particles is also known as Stopping Power.

One can calculate the dose delivered to the patient using the particle beam flux and the Mass stopping power (Equation 1.2), which is the linear energy transfer divided by the density of the medium. Although this equation could be very useful for estimations, it should not be used to directly calculate the dose absorbed by the patient. For such endeavor, the use of a carefully calibrated dosimeter is recommended [Pag12]. A detailed analysis of the stopping power can be found in the work of Ziegler [ZIE99].

$$D = \Phi \frac{-\mathrm{dE}}{\mathrm{d}x} \frac{1}{\rho} = \Phi \frac{S}{\rho} \tag{1.2}$$

D dose
E energy
x distance traversed by the particle
ρ medium density
Φ particle flux
S *stopping power*

1.2.1 Stopping power

The stopping power can be calculated by Bethe-Bloch theory [BET30], described by equation 1.4. The value of the maximum energy transfer to a free electron $Tmax$ is given by the following relationship:

$$T_{max} = \frac{2mc^2(\gamma^2 - 1)}{1 + 2\gamma(m/M) + (m/M)^2}, \tag{1.3}$$

where m is the electron mass and M is the mass of the incident particle. The method of calculation of the heavy charged particle energy loss in the medium is presented by the Bethe-Bloch theory (equation 1.4).

$$\left.\frac{dE}{dx}\right|_{T<T_{cut}} = 2\pi r_e^2 mc^2 n_{el} \frac{(z_p)^2}{\beta^2}\left[\ln\left(\frac{2mc^2\beta^2\gamma^2 T_{up}}{I^2}\right) - \beta^2\left(1+\frac{T_{up}}{T_{max}}\right) - \delta - \frac{2C_e}{Z}\right] \tag{1.4}$$

r_e	electron radius $e^2/(4\pi\epsilon_0 mc^2)$
mc^2	electron rest mass
n_{el}	electron density of the material
I	mean excitation potential
γ	Lorentz transform factor
β^2	v/c
T_{up}	$\min(T_{cut}, T_{max})$
δ	density effect function
C_e	shell correction function

where Zp is the charge of the particle beam. δ is a correction factor for the energy loss due to ionization by the density effect. This effect is noticed when the medium deals with high energies and becomes polarized with the increasing particle velocity of the beam, as the rapid passage of particles will be felt by a large number of particles almost simultaneously. As a result, the atoms in the medium can no longer be regarded as isolated.

The electron density in an element can be expressed as:

$$n_{el} = Z\, n_{at} = Z\,\frac{\mathcal{N}_{av}\rho}{A} \tag{1.5}$$

($\mathcal{N}_{av}$: Avogadro constant, ρ: material density, A: molar mass).

In a composite material, density could be expressed as:

$$n_{el} = \sum_i Z_i\, n_{ati} = \sum_i Z_i\,\frac{\mathcal{N}_{av} w_i \rho}{A_i} \tag{1.6}$$

w_i is the ratio between the mass of i^{th} element, with the molar mass A_i.

Considering the effect of low-energy layers (detailed examination is available in Ziegler's work [ZIE99]), which represents the fact that for low-energy light elements and for all energies within the clinical range, the probability of colliding with electrons of inner layers (K, L, ...) is

negligible, as seen for a 100 MeV beam, when the stopping power is corrected only around 1% [GRE11].

Although less frequently occurring, interactions with the nucleus seem more significant with increasing beam energy, on a cumulative basis, and because a greater penetration of the beam increases the possibility of such interaction, thus becoming important when planning the treatment, because this interactions can cause a decrease in the height of the Bragg peak [FS04].

1.3 Patient positioning in radio and particle therapy

The development of image-based positioning techniques is crucial to minimize the margin error of the radiotherapy treatment, avoiding the delivery of an excessive dose to healthy organs around the tumor and ensuring the prescribed dose deposition within the target volume. In order to fully exploit the potentials of radiotherapy, millimetric precision is desired to optimize the dose deposition. For in-room patient positioning, several techniques are combined to reduce setup errors during treatment preparation and execution. Lasers set on the treatment room walls allow skin-marks alignment; furthermore, X-ray projections, infrared cameras and/or 3D imaging techniques can be used to check for any required correction before or during the fraction delivery.

1.3.1 Sources of uncertainty

Uncertainties mitigation strategies during planning and execution are fundamental for accomplishing a successful treatment. Radiotherapy and particle therapy share a significant amount of uncertainties sources, nevertheless different approaches might be required given the possibility of more serious consequences due to differences in dose distribution derived from particle treatments.

Besides the previously mentioned errors derived from HU to RSP conversion, genetics, physiological aspects, patient positioning and patient's compliance for treatment instructions might alter the results conspicuously. Therefore, the prescribed doses and fractionation based on averages of a large cohort of patients responses to the treatment could

introduce significant uncertainties.

The tumor is usually considered as an homogeneous mass, although it might present heterogeneous tissues and biological activity, which is not detected by conventional CT imaging. Defining a BTV (Biological Target Volume) (Ling et al. 2000), by using different image modalities such as PET and MRI, would increase the knowledge about radiation response of the tissue and support treatment planning strategies. BTV definition and delineation protocols should also reduce potential inconsistencies between targets perceptions by different physicians.

The TPS (treatment planning system) is a fundamental tool for radio and particle therapy, since it allows the visualization and optimization of dose distribution while balancing the PTV-OAR trade-off. In order to estimate the dose interaction with human tissues several types of algorithms can be used, which in turn might rely on different mathematical methods and take into account physical processes that lead to diverse results. Due to the constant increase in computational power and its larger reliability (many times considered as a gold standard), Monte Carlo methods are likely to be incorporated in clinical routine.

.

1.3.2 Image registration

Image registration plays a key role in patient positioning, since it is applied to provide information regarding the geometrical reproducibility of the treatment planning patient setup at each treatment fraction. Image registration is used to determine the spatial transformation for the alignment of two images by mapping corresponding anatomical structures.

The Image Registration (IR) basically requires a metric, an optimizer, a transform, an interpolator and two inputs, a fixed and a moving image. The metric provides a measure of the similarity between the transformed moving image and the fixed image. The optimizer works to improve the similarity measured by the metrics with respect to the spatial transformation parameters. A basic registration framework is depicted in figure 1.6.

The spatial transform contains the mapping of points from the fixed

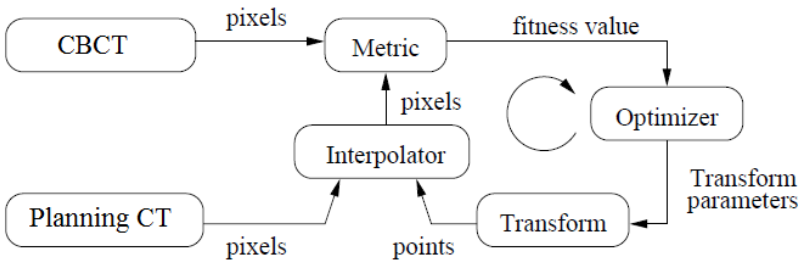

Figure 1.6: *Example of a basic registration framework. Adapted from [JMIC13].*

image space to the moving image space. IR could be considered then as an optimizing task, which entails finding a spatial transform that will map homologous points resulting in the alignment of the two images.

The rigid registration modality consists in finding a rigid transform that will only rotate and translate the moving image in order to align it to the fixed one. It is therefore possible to obtain a correction vector to be applied to the treatment couch to achieve setup reproducibility. Deformable Image Registration (DIR) has the potential for an important role in modern radio and particle therapy. It finds a non-rigid transformation to be applied to the planning CT regarding any intra-fractional geometric change in patient's anatomy, thus allowing treatment margins reduction and daily dose verification [VAA15, VMM+14].

1.3.3 Orthogonal X-ray projections (2D-3D method)

Most of radiotherapy and particle therapy centers apply 2D-3D image registration methods [LKP11, MTC+09] for patient setup verification. This method is based on two orthogonal 2D X-ray projections of the patient, which are compared with digitally reconstructed radiographies (DRR) obtained from the patient's planning CT. The chosen metric between these two projections and the generated DRRs is iteratively computed and optimized, in order to obtain the parameters of a rigid spatial transformation which is applied to the treatment couch to reduce to a minimum the patient setup discrepancies between the actual position and the position at the planning CT scan. An example of image registration with orthogonal kV and MV projections from the on-board imager with DRRs from treatment planning system can be seen in figure 1.7

and figure 1.8, respectively.

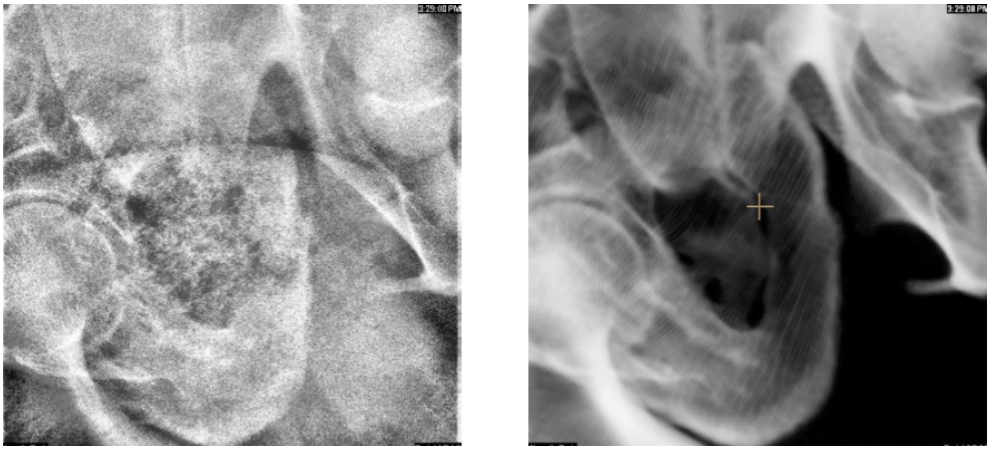

Figure 1.7: *2D orthogonal kV projections (left) and DRR from planning CT for a prostate cancer patient (Images from Hospital Vitoria-BR).*

1.3.4 Cone Beam Computed Tomography (3D-3D method)

The Cone Beam Computed Tomography (CBCT) is a technique based on divergent X-rays, which gives the beam a cone shape. At the Centro Nazionale di Adroterapia Oncologica (CNAO, Pavia-IT) the scanner rotates around the patient while acquiring around 600 projections (figure 1.9), which are used by Feldkamp-Davis-Kress method (FDK), obtaining a barrel-shaped effective volume. Volumetric images are capable of identifying both bony structures and soft tissues. Tumors localized in soft tissues can be easily misplaced between treatment fractions, therefore treatment setup verification based on bone alignment may not be much effective, resulting in larger error margins and uncertainties in overall dose distribution. Thus, the use of volumetric images for pre-treatment verification allows better image guided radiotherapy (IGRT) for prostate and lung cancer cases than does 2D patient alignment modality [LZZ$^+$08] since the CBCT has the potential to give detailed soft tissue information of the patient.

CBCT can be registered with the planning CT in order to verify any possible variation on patient's structural anatomy. Although it has lower image quality, the CBCT has the advantages of lower doses given to the patient and the possibility of imaging on the treatment couch. These

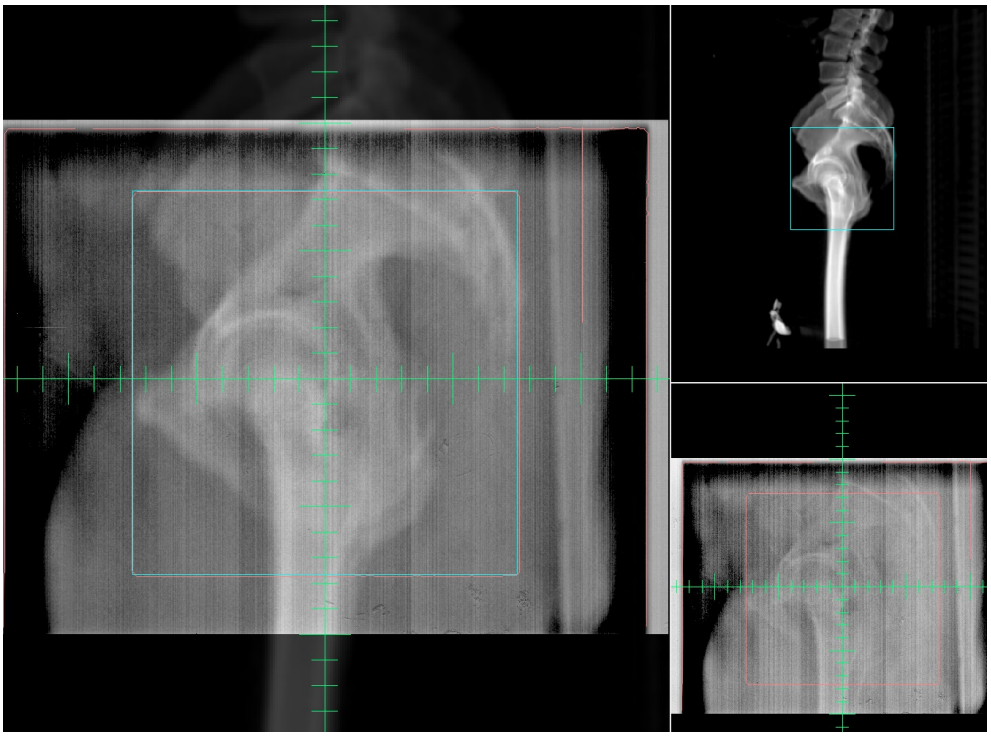

Figure 1.8: *DRRs from treatment planning system overlaid with 2D orthogonal mega voltage projections for a prostate patient (Images from Hospital Vitoria-BR).*

measures contribute to an updated treatment plan [LNJ+13] following the adaptive radiotherapy (ART) (Yan et al 1997) main idea. Some of these procedures may consist in dose of the day calculation and deciding if there is the necessity of a new CT image acquisition for treatment re-planning purposes [YLA+14].

1.3.5 Image-guided proton therapy

To take into account uncertainties of the Bragg peak positioning regarding its dependency on the CT-based stopping power remapping, repeated CT scans are required [LDZ+15] to obtain an updated anatomy scan, resulting, at least, in more dose delivered to the patient. Due to differences between the patient position during the CT and when laid on the treatment couch, in-room image acquisition maybe more advantageous to depict stopping power maps mimicking the treatment conditions.

For in-room patient positioning, some techniques are combined to reduce the error during treatment execution. Lasers fixed on treatment

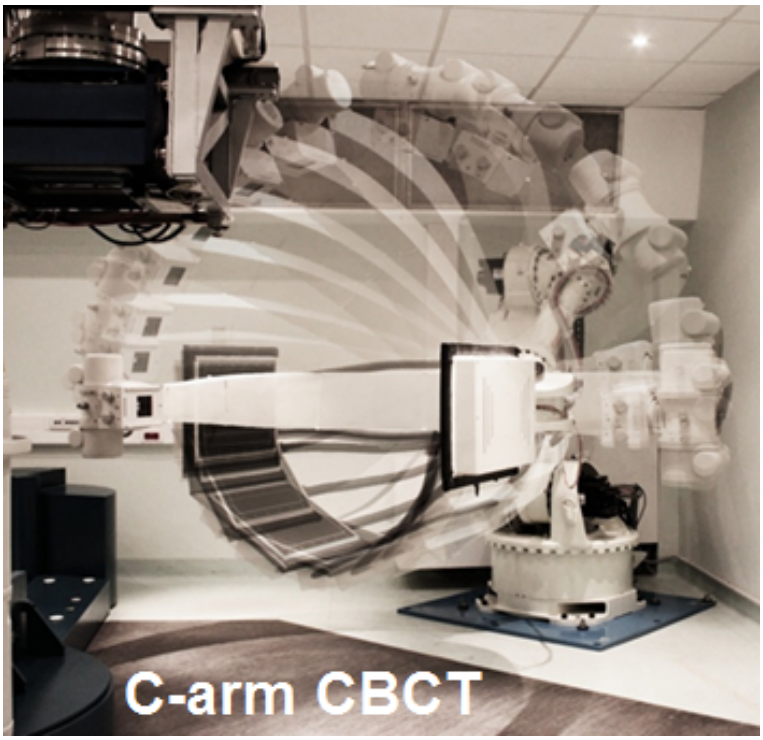

Figure 1.9: *CBCT at CNAO treatment room. Adapted from [Fat13].*

room walls allow skin-marks alignment, then to check for any required correction before or during the fraction delivery, X-ray projections, infrared cameras or 3D images can be used.

Laser and infrared alignment are non-ionizing methods for patient setup, nevertheless they just account for the external geometry of the patient, thus the use of X-ray 2D or 3D images grants further accuracy. Contrasting the higher dose and the complexity of CT-on-rail, Cone beam CT (CBCT) and proton CT (pCT) show themselves as interesting candidates for further investigation and development. Nevertheless few particle therapy centers already use cone beam CT and a proton CT scanner is not available for clinical usage yet.

1.3.5.1 Proton computed tomography

While proton beam characteristics allow better beam conformity of the dose distribution, uncertainties in patient positioning can compromise treatment effectiveness. Therefore, there are ongoing efforts to develop and improve image guidance for proton therapy.

Currently, particle therapy treatment planning is made based on conventional X-ray tomography of the patient, then the CT numbers obtained are converted into RSP (relative stopping power) by means of a calibration curve. This conversion can lead to uncertainties around 3 to 5% [WMT12, SCH11], which could drastically interfere in the outcomes of the treatment. Image guidance in proton therapy is specially important due to the behavior of the proton beam when it traverses different materials (figure 1.10), resulting in different dose distribution than planned. Precise proton range estimation is required and the usual stoichiometric calibration of HU with tissue substitute materials is not adequate. Two materials could have the same HU but different stopping power, which may result in a erroneous dose distribution.

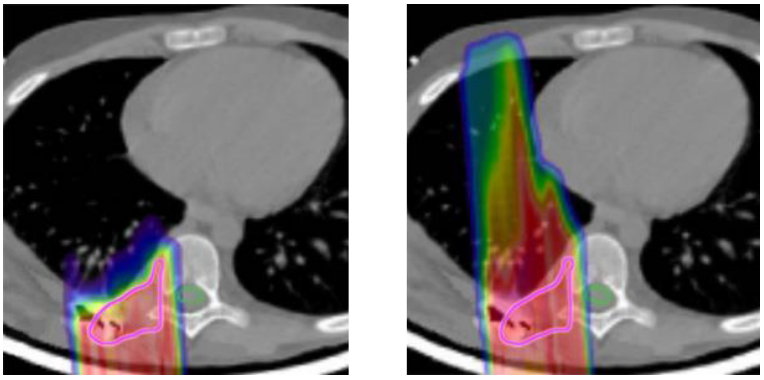

Figure 1.10: *Same observed treatment on the left applied to a different anatomy on the right, resulting in overshooting. Adapted from [Cle12].*

One way to overcome such an issue is to create an imaging system with its own detectors, which allow the reconstruction of proton-based tomographic images, thus measure the RSP directly. Using the same elements of the treatment beam for imaging allows better knowledge of beams interactions with matter, thus eliminating the errors from CT numbers to RSP conversion due to conventional CT usage. Therefore proton CT (pCT) has been proposed as a method for reducing this uncertainty and a scanner prototype has been developed (figure 1.11) [CBH$^+$13, SJM$^+$13]. Besides treatment planning, proton CT could also be useful for image guidance in the treatment room, due to its image quality and low dose to the patient.

The basic proton interactions with tissue do not change their physical

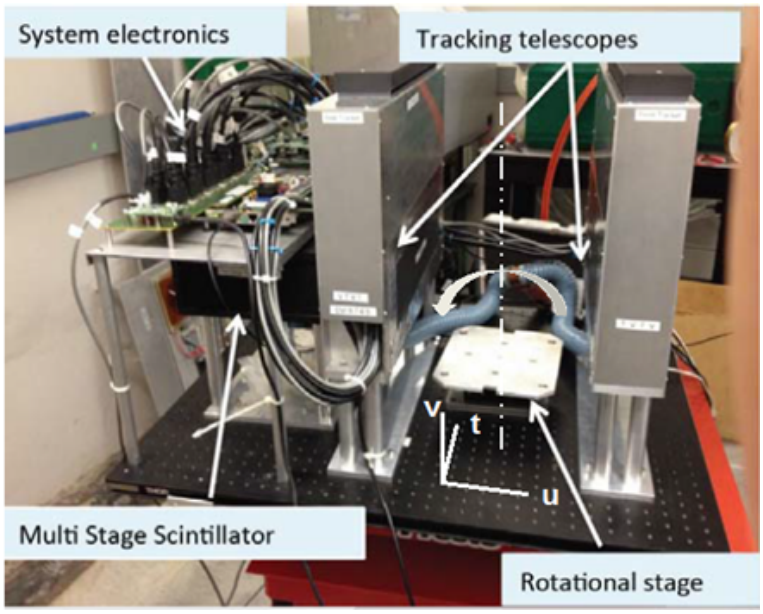

Figure 1.11: *pCT phase II scanner (Courtesy of pCT group).*

characteristics, only a few changes on its trajectory (therefore exit angle) and energy may occur (provided it has not undergone nuclear collision). Then using such information, one can trace back the linear energy loss and the distribution of the medium densities, making the planning dose calculation more accurate [SBB$^+$03] and so, one can make the most of the potential of proton therapy. Increased energy results in a narrower exit beam in the region preceding the Bragg peak, which directly affects the quality of the reconstructed pCT image as it enhances spatial resolution [DPS$^+$11]. One of the main obstacles to be dealt with is the degraded spatial resolution due to Multiple Coulomb Scattering (MCS) inside the imaged object. Methods like the Most Likely Path (MLP) [PSCR10] are proposed to be implemented inside the reconstruction algorithm to predict the particle trajectories based on information obtained before and after the object. Iterative algorithms are used to reconstruct 3D pCT images from radiological projections. The iterations works on improving the estimation of the reconstructed object, and the algorithms differ on how they assess the similarity between measured and simulated projections and how they search for improvement. Accurate modeling of the physical processes should be incorporated without compromising the code's time-efficiency for clinical implementation. Analytical algorithms are

less time and memory consuming, although iterative algorithms have a great potential of producing smaller voxels with better spatial resolution, specially when using the iterative algebraic reconstruction technique (ART) [PSM+10]. With the continuous development of parallel processing, a clinical setting for proton CT may become feasible.

Studies on the trajectory of protons aim at improving the quality of reconstructed images . The difference of the trajectories considered during image reconstruction, as shown in Figure 1.12, affect the reconstructed images outcome in Figure 1.13, showing that MLP results in better image quality over considering straight lines as the filtered back-projection (FBP), which is an analytical method.

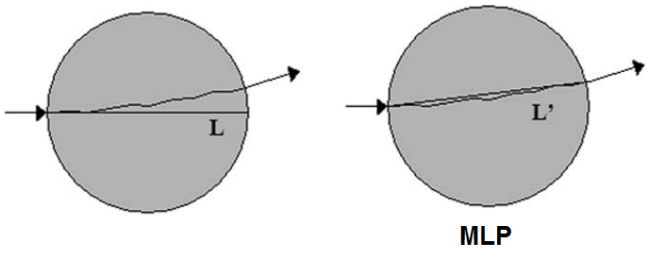

Figure 1.12: *Proton estimated trajectory considering: only the entry position (left), entry and exit position (right). Adapted from [SBL+04a].*

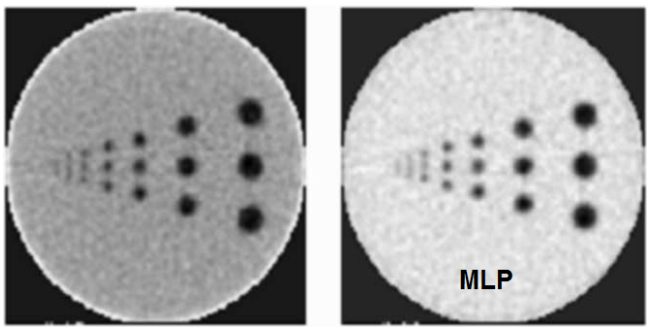

Figure 1.13: *Images reconstructed from the trajectories choices exemplified in Figure 1.12. Although the spatial resolution is similar, there are distortions in the left image density in the object limits, which are not seen in the other image. Adapted from [SBL+04a].*

Significant advances in proton imaging have been published [SJM+13, PBG+16, PC15], but it is not available for clinical use yet. The implementation of pCT in clinical practice still requires higher resolution im-

ages and faster data processing. It is necessary, therefore, to develop appropriate techniques to maximize the spatial resolution, providing pCT images with the highest quality standards [SBL$^+$04a].

Among the difficulties pCT may find, Wang et al. [WMT12] discuss the high energy required for acquiring images keeping the patient pelvis within the pre-Bragg region (before the maximum range of the beam), which may imply a significantly more powerful beam and a more elaborate structure for controlling it.

CHAPTER 2

Evaluation of patient positioning methods

In this chapter, the efficiency assessment of a few positioning methods is presented.

The effectiveness of the clinical treatment relies on daily reproducibility of the plan. Accordingly to treated site, patient health condition and available technology, different positioning techniques can be applied. Image-guidance allows reduction of errors, which is fundamental for achieving positive outcomes. Random and systematic errors, i.e., those derived from organ delineation, organ motion, setup verification and imaging modality, have to be addressed when defining the safety margins in the PTV (planning target volume) [RRLV02, Van04, SH02, Gle14].

Within the context of image-guidance, a fundamental step for adequate patient positioning is the image registration (IR) process. The IR process is important to visualize the relationship between two images, for example, planning CT and in-room X-ray projections (2D-3D IR). In image-guided radio and particle therapy, IR main objective is to find a correction vector to be applied to the treatment couch [SBMT09]. Skin marks, in-room laser and infrared cameras alignment are largely used non-ionizing methods for patient setup verification. Although helpful,

these methods do not consider internal changes in patients body or inside immobilization devices, when applied. Furthermore, deformable IR (DIR) allows planning CT deformation for dose recalculation and analysis within patient geometry-of-the-day after a deformable registration procedure.

Each modality of IR presents capabilities and limitations, for example:

- Internal fiducial markers could lead to more precise positioning when using X-ray radiography, nevertheless, costs and difficulties associated with their placement make bone anatomy and greater safety margins a more common choice. Fiducials make prostate localization easier, although the spatial relationship between the target and organs-at-risk cannot be verified [APA12];

- Megavoltage (MV) portal images are easily acquired using the linear accelerator gantry with the patient in treatment position. The contrast limits its usage to bone alignment and rotations are not typically corrected with this method;

- X-ray kV projections feature better quality than MV images. Orthogonal projections are compared to digitally reconstructed radiographies (DRRs) from the planning CT and corrections are applied to the treatment couch. Projections images do not provide soft tissues informations as volumetric images do, such as CBCT. One of the main limitations of bone-based IR is that it does not take into account changes in internal anatomy during the treatment.

- Deformable image registration can help to evaluate the dose distribution by updating patient anatomy; nevertheless, online plan verification and adaptation can be time consuming. To consider all volumetric information for deformable image registration procedures, a greater computational effort is required. Limited-fov (Field-of-view) CBCT could assist the verification of organs displacement or filling, but, for particle therapy, not considering all the beam path could lead to erroneous dose estimation. Therefore, large fov CBCT and CT-on-rail are more suitable for adaptive therapy.

An extended review of image-guidance methods can be found in Timmerman and Liu's book [TX10].

2.1 ExacTrac for patient setup in hypofractionated prostate radiotherapy

Offline positioning procedures based on megavoltage portal images are commonly used for prostate treatment, by gathering information about systematic and random errors to make an estimation of how the rest of the treatment should be carried out [LBH$^+$06]. By means of the Van Herk et al. [Van04] method, Gleeson [Gle14] calculated new PTV margins and demonstrated that online bony anatomy verification can ensure reduced margins when compared to offline verifications using megavoltage EPIs (electronic portal images).Therefore, including in-room X-ray projections cam potentially improve corrections in patient positioning, if compared to skin marks or portal imaging alignment. Thus, improvements in treatment precision, which might allow margins reduction, are expected. Image-guided radiotherapy (IGRT) is important for increased accuracy in patient setup, assuring prescribed dose deposition for local tumor control. This is extremely relevant with a reduced number of fractions, as the dose is elevated and uncertainties may result in significant toxicity [MTC$^+$09].

Hypofractionated radiotherapy has been studied for prostate cases and shows high long-term survival rates [NSF15]. Hypofractionation for geriatric patients allows treatment length reduction from up to 9 to 5 weeks, which contributes for the patient general well-being. Cancer incidence is higher for elderly patients. Due increased longevity, new methods are discussed in order to meet the needs of geriatric cancer patients. Radiotherapy is indicated for over 50% of elderly patients, independently of its association with surgery or chemotherapy [ALM08]. The constant development of treatment methods allows personalized approaches and more effective outcomes.

By the end of 2013 a hypofractionated protocol for low an intermediate-risk prostate cancer patients, which intends to deliver 66 Gy in 22 fractions of 3 Gy, was implemented at Hospital Vitoria (Santos, Brazil). This

study reports the quantitative assessment of patient setup accuracy on a population of 21 patients who underwent this hypofractionated therapy scheme. For image guidance, the BrainLAB AG ExacTrac system (X-ray orthogonal projections acquisition) was applied systematically. The short-term clinical follow-up features satisfactory results in accordance to similar studies carried out in other institutions [PFC+13].

2.1.1 Materials and methods

For the setup corrections analysis, data from 21 hypofractionated treatment patients were analyzed. Three patients were between 64 and 68 years old, the others were from 70 to 87 years old. Treatment planning was performed on the basis of CT imaging featuring a voxel size of 0.84 mm, 0.84 mm and 2.5 mm for right-left, anterior-posterior and superior-inferior axes, respectively. The PTV margin was 7 mm in all directions. Before each treatment fraction, the patient was positioned on the treatment couch and had his skin markers aligned with in-room lasers. After this initial setup, orthogonal kV X-ray projections were acquired to be compared with digitally reconstructed radiographs from the patients CTs. The rigid image registration (IR) procedure estimated the parameters of a 6 DoF (degree of freedom) correction, based on bony anatomy alignment, which was visually assessed. For these patients, since the prostate is not visible in 2D radiography (figure 2.1) or portal images, the bony structure of the pelvis was used as a surrogate. Although the pelvis is well visible in kV X-ray images, the position of the prostate relative to this bony structure might not be maintained, thus requiring to account for this uncertainties when the margins of the planning target volume (PTV) are defined.

The patients were treated with the Varian high-energy medical linear accelerator Clinac iX 5187, integrated with the BrainLAB AG ExacTrac 5.5.6 system for image guidance (figure 2.2). After the treatment, a positioning report was generated; it contains all the 6 DoF corrections applied to the treatment couch for each patient. The corrections of the first day of treatment were discarded due to CT coordinates to isocenter shifts for initial patient setup.

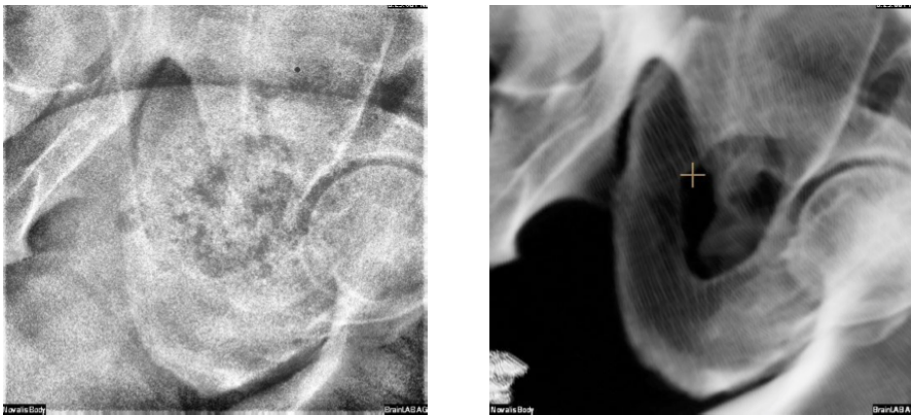

Figure 2.1: *ExacTrac image acquired (left) to serve as fixed image for alignment with DRR (right) from planning CT during prostate patient setup.*

Standard prostate PTV margins of 10 mm, except for posterior direction where 7 mm is used for rectum sparing, were created to verify how much healthy tissues are removed from PTV when reducing the margins from this standard to the 7 mm margins used in this study.

2.1.2 Results

In total, 442 6 DoF correction vectors (translations and rotations) were analyzed. The mean and standard deviation (std) values for the 442 corrections applied to the treatment couch are presented in tables 7.1 and 7.2, whereas the distribution of these values is presented in figure 2.3. Results are reported as translations (t) and rotations (r) for each anatomical direction.

Corrections	Translation RL (mm)	Translation SI (mm)	Translation AP (mm)
Mean	1.72	0.44	-1.15
Std	5.55	3.50	3.14

Table 2.1: *Mean and Standard Deviation values of correction vectors for translations applied for patient setup.*

The Volumes of PTV structures and their differences accordingly to chosen margin are presented on table 2.3.

Corrections	Rotation RL (degrees)	Rotation SI (degrees)	Rotation AP (degrees)
Mean	0.57	0.27	0.01
Std	1.30	1.00	1.01

Table 2.2: *Mean and Standard Deviation values of correction vectors for rotations applied for patient setup.*

Table 2.3: *Volumes of PTV structures for different margins (in cm^3).*

Patient	PTV 10 mm	PTV 7 mm	Difference	CTV
1	172,76	127,41	45,35	37,84
2	181,23	139,87	41,36	50,09
3	185,96	139,24	46,72	52,67
4	184,90	141,03	43,87	46,95
5	214,22	162,42	51,80	56,07
6	133,64	101,42	32,22	33,44
7	190,15	140,22	49,93	47,11
8	155,37	120,19	35,18	42,83
9	192,03	149,53	42,50	50,45
10	136,36	104,55	31,81	34,56
11	222,97	167,93	55,04	68,03
12	176,39	137,63	38,76	48,53
13	172,54	129,33	43,21	41,73
14	256,25	206,52	49,73	79,76
15	130,53	96,53	34,00	33,04
16	241,53	184,86	56,67	65,00
17	217,21	169,54	47,67	67,52
18	194,71	148,87	45,84	60,12
19	221,02	175,79	45,23	70,70
20	168,81	127,45	41,36	46,10
21	223,18	159,59	63,59	72,73

Figure 2.2: *Example of ExacTrac©Image-Guided Radiation Therapy applied for prostate patients.*

2.1.3 Discussion

This study reports that daily patient setup corrections in prostate patients were for the most part below the EPI-based action level (5 mm), thus suggesting that the systematic application of image guidance methods based on bony anatomy in 3D might provide a considerable gain with respect to more conventional techniques.

The applied corrections represent an incremental adjustment after skin-based laser alignment, which means that ExacTrac potentially reduces the residual setup errors of this method.

The ExacTrac system verifies the position of the patient and applies a correction vector daily, reducing the bony alignment uncertainty to sub-millimetric magnitude, which is certainly an important requisite in the framework of an hypofractionated radiotherapy protocol. It is worth noting that the simple application of an EPI-based setup assessment would have triggered an action in presence of planar (2D) discrepancies above 5 mm and would have hindered to take into account rotational mismatches, which could alter significantly the dose distribution, thus compromising the treatment outcome and not exploiting the full potential of intensity

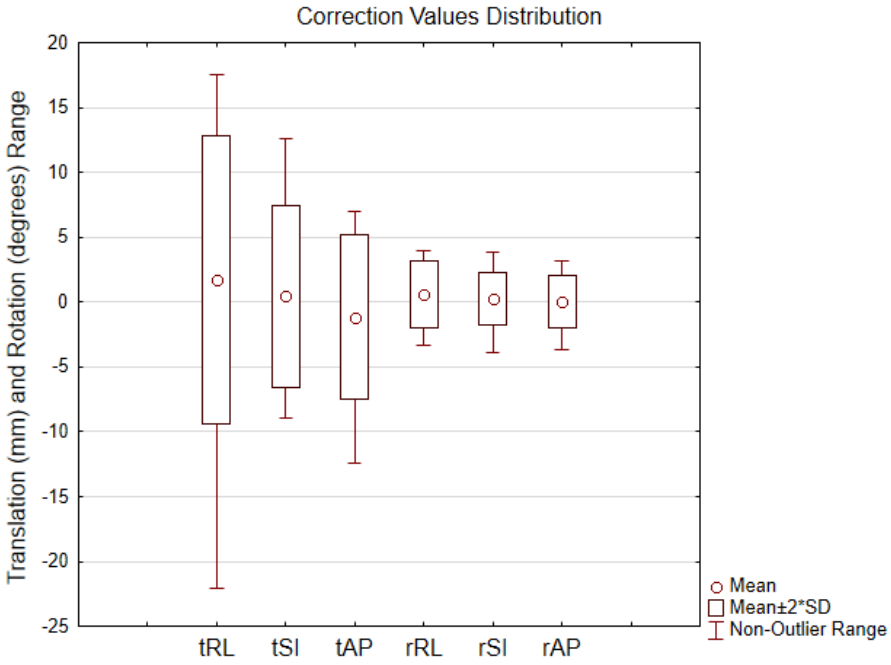

Figure 2.3: *Distribution of correction vectors values applied for patient setup.*

modulated radiotherapy (IMRT).

The size of the corrections provided by the ExacTrac system suggests that skin-marks-based patient alignment might not be sufficient to grant the required level of setup accuracy in hypofractionated radiotherapy. The large corrections found especially for translations along the RL direction might be explained by patients high body mass, which made particularly difficult to obtain an acceptable setup based on skins-markers and laser alignment.

Orthogonal 2D kV projections feature higher image quality, spatial resolution and signal to noise ratio than portal images. This allows one to exploit automatic image registration procedures for the estimation of 6 DoF corrections to be applied for patient setup refinement. The reduction of the margins (from usual 10mm to 7 mm) resulted in volumes of spared healthy tissues often comparable to the size of the target volumes (CTV).

Further margin reductions require fiducial implants [LBH+06,NHD+02] or daily volumetric images with soft tissue contrast for more precise prostate localization. A similar study from [PFC+13] reported positive results for long-term follow-up for similar treatment but with in-

creased precision in prostate localization by using two-dimensional ultrasound system (BAT system, NOMOS Corporation, Cranberry Township, PA) [PPP+07].

2.2 Orthogonal projections and optical tracking system

At CNAO (Pavia-IT), orthogonal X-ray imaging and OTS (optical tracking system) have been combined for an optimized framework in image-guided therapy. X-ray projections are acquired in order to be compared with the planning CT, obtaining a six degrees of freedom (6DoF) corrections (translation and rotation) to be applied to the treatment couch. Fiducial markers, placed over the H&N (head and neck) patients' mask, are continuously monitored with infrared cameras, thus providing the evaluation and reduction of setup errors before X-ray corrections. IR procedures benefit from previous alignment and OT does so, bringing the patient close to the optimal condition. OTS is more effective and less time consuming than manual alignment, making IR potentially faster and more effective.

We compared the corrections applied to the treatment couch after X-ray verification, with and without the previous use of the OTS in order to verify if OTS implementation could benefit the IR process by reducing initial setup errors.

2.2.1 Materials and methods

Were evaluated 170 corrections from different H&N patients treated with particle therapy. Half of the collected corrections were obtained after combining both systems. The corrections applied to the robotic couch, are separated in rotational (Pitch, Roll and Yaw) and translational (Lateral (LL), Cranialcaudal (CC) and Anteroposterior (AP)).

2.2.2 Results

Corrections distributions are shown in figures 2.4 and 2.5. The mean values of corrections obtained without OTS pre-alignment for rotations were 0,2 $\pm$0,8; -0,4 $\pm$0,5; 0,8 $\pm$0,9 (degrees) and for translations, 0,7

±1,0; -1,5 ±1,5; -0,9 ±1,4 (mm) for LL, CC and AP directions respectively. After using OTS, the mean values of corrections obtained for rotations were 0,4 ±0,7; -0,3 ±0,6; -0,1 ±0,5 (degrees) and for translations, -0,6 ±1,6; -0,04 ±5,3; 3,2 ±3,4 (mm) for LL, CC and AP directions respectively.

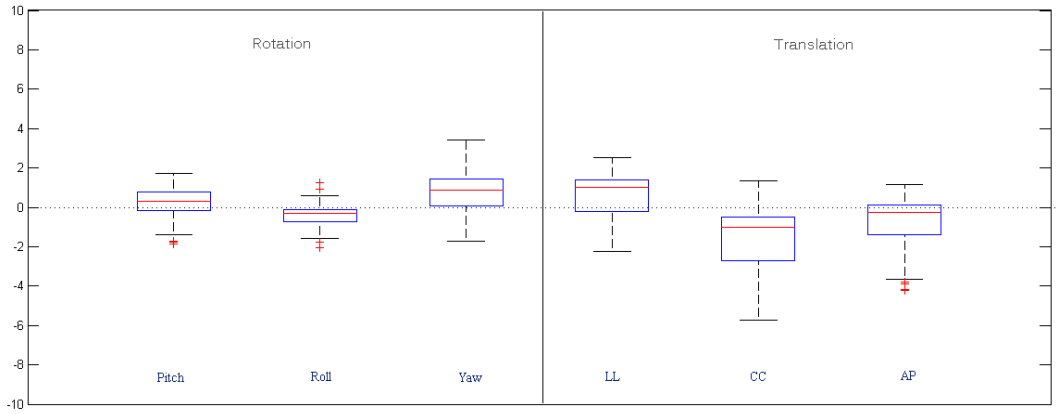

Figure 2.4: *Corrections distribution after 2D-3D rigid registration, without OTS pre-alignment.*

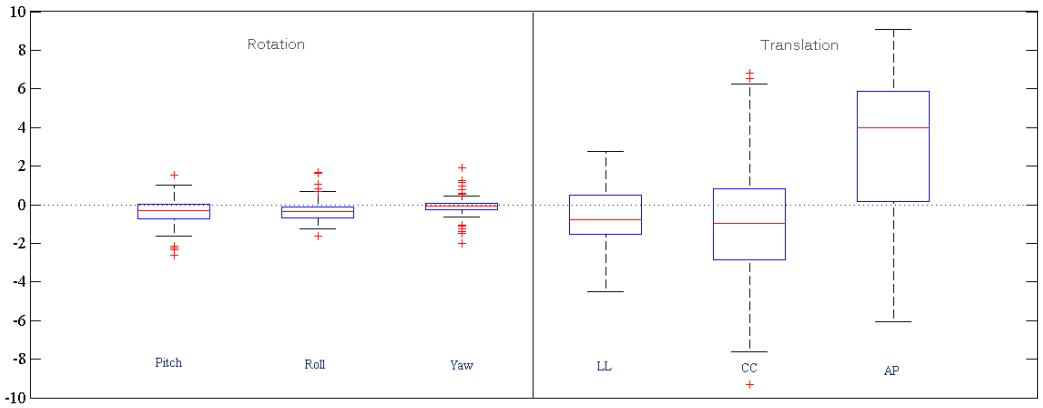

Figure 2.5: *Corrections distribution after 2D-3D rigid registration, with OTS pre-alignment.*

2.2.3 Discussion

Peng et al. [PKL+10] found mean differences on the pretreatment displacements of 1.3 mm and 1° between the studied OTS and a CBCT

system. Our Results show similar corrections magnitude and errors reduction for rotations after patient initial setup with the OTS. OTS grants errors reductions regarding the fiducials, which are placed on the immobilization mask. Source of OTS uncertainties are the reproducibility of the configuration and position of this contention device and the fact that only X-ray projections would detect independent patient misplacement inside the mask. This might explain the random errors found by X-ray imaging analysis after OTS initial alignment. OTS still makes possible considerable time reduction in patient positioning due to automatic alignment before IR. Thus, initial correction based on OTS information might improve patient positioning, besides real-time monitoring benefit [DTF+13, FRP+14]. Furthermore, reduction of rotational positioning errors seems possible relying on OTS corrections.

2.3 Rigid CT-CBCT registration

A patient positioning software based on CT-CBCT 3D image registration (XPPV) developed by Fattori [FRP+14] for CNAO clinical usage was evaluated for its capability to recover a set of 32 known transformations imposed to the anthropomorphic Alderson RANDO Man (Radiology Support Devices, USA) phantom fixed on the treatment couch (figures 2.6 and 2.7).

The registration software is based on Insight Toolkit (ITK) [YAL+02] generic programming library. The metric used is the normalized mutual information metric to be minimized by the Amoeba optimizer. The parallel implementation guarantees low execution time (below 1 min) in CNAO clinical installation.

2.3.1 Materials and methods

The CBCT images were acquired with a six joints articulated robot (Kawasaki ZX-300S) installed on the treatment room floor and equipped with a custom C-arm, featuring a diagnostic kV X-ray tube (Varian A-277) and an amorphous-silicon flat panel detector (Varian PaxScan 4030D).

The raw data of the pelvis phantom acquired at CNAO with Cone Beam Computed Tomography modality were reconstructed with PLAS-

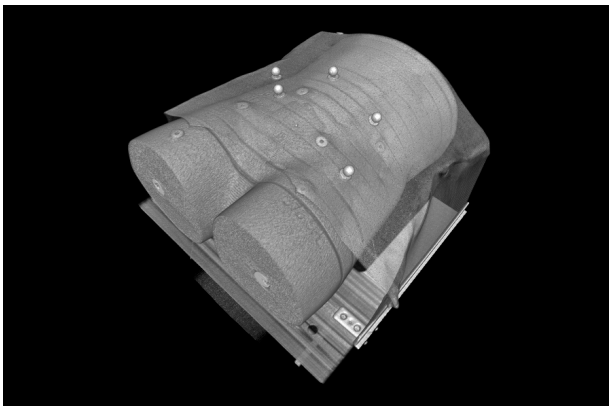

Figure 2.6: *CT image of the Rando phantom used in this study positioned in the treatment couch.*

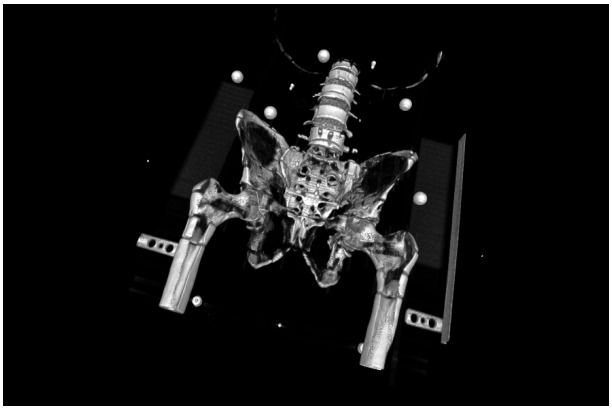

Figure 2.7: *Bones and markers of the Rando Phantom used for image registration.*

TIMATCH with physical size of 250 mm on right-left axis, 250 mm on anteroposterior axis and 340 mm on craniocaudal axis. The voxel size was set to 1.0 mm in all three directions.

To evaluate the registration efficiency of XPPV software, 32 transformed images were registered with the reference CT. To create those images, random transform values were obtained based on orthogonal sampling theory. With this procedure, 32 strings with 6 elements (3 translational and 3 rotational) were created. The translational range was set to $\pm$ 10 millimeters and the rotational range to $\pm$ 3 degrees.

To create the 32 shifted CBCT images AMIRA 5.2 was used. The original images were transformed accordingly with each of the 32 transform strings, and then re-sampled with Lanczos filter and reference mode.

Initial manual alignment was performed before XPPV automatic IR,

as usually done clinically.

2.3.2 Results and discussion

The residuals errors distribution after registering these 32 transformed images with the reference CT are shown in figure 2.8

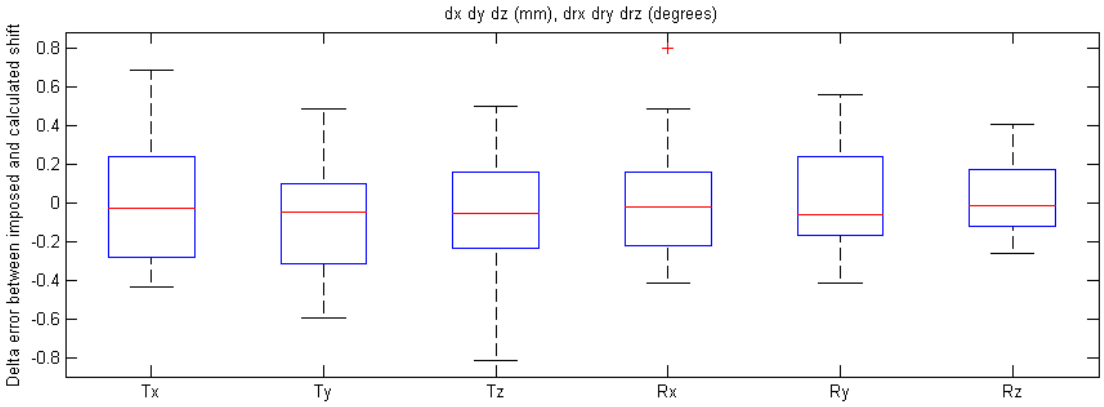

Figure 2.8: *Residual errors distribution for the 3 translation (Tx, Ty and Tz) and 3 rotation axis (Rx, Ry and Rz).*

The XPPV evaluation was based on the capability of the algorithm to recover an imposed transform based on gray levels information of the pixels, with an initial operator contribution. Syker et al. [SBMT09] demonstrated standard deviation of translational IR errors of 0.5 mm by using patients images and the commercial chamfer-matching algorithm (Elekta, Crawley, UK). Another study using phantom images acquired with CBCT presented IR errors as the root mean square of Euclidean distances between contours of 3.5$\pm$1.2mm [WSPB10]. This study evaluated XPPV software and presents residual errors within $\pm$ 1 mm and $\pm$ 1 degree threshold after registration of 32 different transformed CBCT images, thus demonstrating the patient positioning tool's efficiency and robustness. Nevertheless, visual assessment prior to treatment is required due to the fact that small rotation errors, as those found in this study, could lead to large misalignments for regions of interest far from the center of rotation.

2.4 Deformable Registration Algorithm for CT-CBCT registration for limited FoV CBCT

In this study, a CT to CBCT deformable registration method, for limited FoV (field of view) CBCT (figure 2.9), based on the the Insight Segmentation and Registration Toolkit (ITK) [YAL+02] is presented.

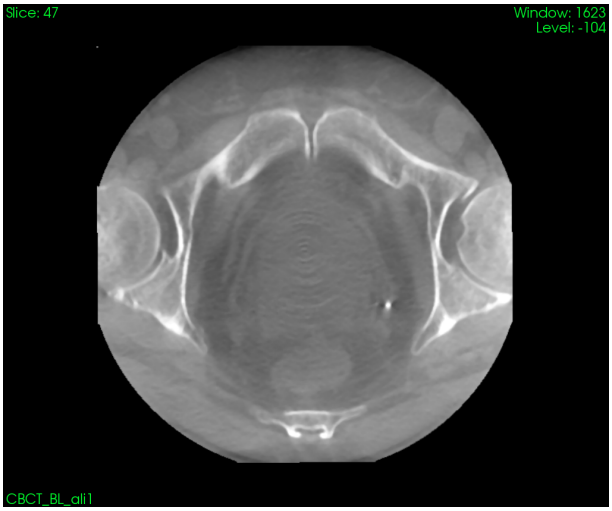

Figure 2.9: *Limited FoV CBCT used for this Study.*

An ITK based C++ algorithm was developed by the author in order to explore the soft tissue information of the CT-CBCT images to perform quality deformable registration, making efforts to overcome the poor signal-to-noise ratio and the limited FoV that limits the CBCT usage.

Head and neck (H&N) cases have been studied and considered for the implementation of deformable registrations using Cone beam Computed Tomography. Previous works with H&N phantom shows that deformable registration relying on CBCT-CT information could be useful for daily proton dose recalculation [VAA15, LDZ+15].

As the prostate moves or presents deformations independently of the surroundings bone structure, taking into account soft tissue information could lead to a more precise treatment, since pelvic bone-based alignments may under-dose the prostate in one-third of the fractions [FHS+13].

2.4.1 Materials and methods

The aforementioned algorithm provides a method of deformable image registration (DIR) between CT-CBCT images of the same patient. The first steps of the algorithm were to rescale the intensity of the CBCT image and then apply a histogram-matching filter between both images, which contributes for the feature extraction steps, used for DIR quality assessment. Mattes mutual information [MH01], often applied for multi-modality images, was used as the metric. This metric tends to map homogeneous regions from the moving image into homogeneous regions of the fixed image. The mutual information is a statistical comparison of the images based on their intensity distribution and shows robustness even with image noise and heterogeneous image superposition. For minimizing the metric, the regular step gradient descent optimizer was applied, which set the parameters in the direction of the gradient to calculate the step size. To handle the deformable transforms application, the B-Spline interpolator was used.

The planning CT and 5 CBCT images of 2 prostate cancer patients treated with ultra-hypofractionated IGRT at the European Institute of Oncology (Milan, Italy) were included in this study. The CT image resolution was 1.25x1.25 mm^2 in-plane and 2.5 mm in the cranio-caudal direction, whereas the voxel size of CBCT reconstruction was set to 0.39x0.39x2.0 mm^3.

In order to evaluate the registration method, a 6 DoF (degree of freedom) rigid registration was performed for every CT-CBCT pair by means of Amira 5.2.0 affine registration module. Normalized mutual information was chosen for the metric, due its good performance for images from different modalities, and extensive direction was set for optimizer as it is well suited for coarse resolution levels (Amira Guide, www.visageimaging.com). To quantify the improvement in the patient positioning outcome of our method, over the rigid positioning one, the mutual information between the images pairs before and after these different registration modalities was calculated. The mutual information measures the statistical relationship between the intensities distributions of the two images. This quantification gives us numerical support to our

visual evaluation over the registration improvement.

To complement the assessment of the algorithmś performance, the Scale Invariant Feature Transform (SIFT) [Low04, CH09] was used. Sift has shown itself to be an useful tool for DIR evaluation as an automated way to identify correspondent features between images [PPR+13] using difference of Gaussian image filtering. The n-dimensional SIFT allows image registration methods assessment by landmark residual distance evaluation. After finding correspondent points between the CBCT and the transformed CT, the distance of each landmark pair was measured, allowing the quantification of residual errors for each axis (x, y, z).

The landmarks obtained by Sift feature extraction were distributed among soft and rigid tissue as shown in figure 2.10.

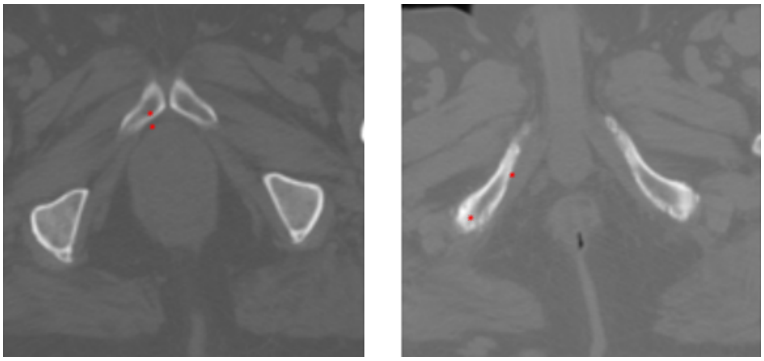

Figure 2.10: *Landmarks obtained with SIFT feature extraction for a pelvic region CT.*

2.4.2 Results

Correspondent points were identified and their distances measured for each pair of images. Their residual distances distribution can be seen in figures 2.11. After rigid registration, the residual errors and the number of outliers are higher than those from the deformable method. It can be noticed that after deformable registration the majority of the distances measured lay under 1-2 mm, with a negligible number of outliers.

Smaller distances between correspondent landmarks of the CT-CBCT pair were found after using the deformable registration algorithm. The mean values of the distances in mm can be seen in table 2.4.

After registering the images, their histograms were rescaled and matched in order to optimize their relation for extracting features with SIFT. The

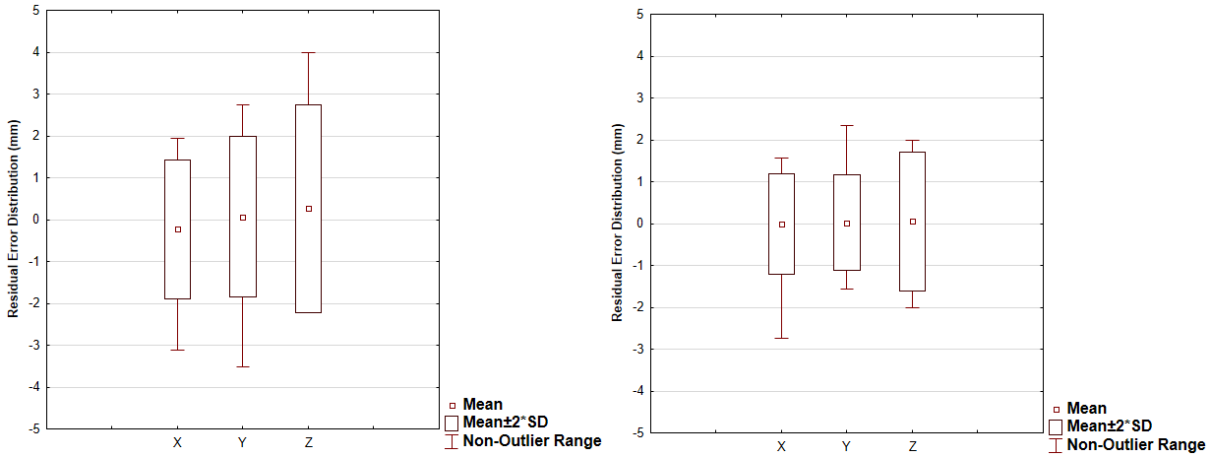

Figure 2.11: *Residual error distribution after rigid (left) and deformable (right) image registration.*

Mean Distance (mm)	Set 1	Set 2	Set 3	Set 4	Set 5
Rigid	1.690	1.866	1.426	1.525	1.390
Deformable	0.985	0.474	1.062	0.672	0.854

Table 2.4: *Mean values of the distance between landmarks after rigid and deformable registration of each set of patient images. Values expressed in mm.*

residual distance between the landmarks found by SIFT can be seen in figures 2.12 and 2.13 . Then, the mutual information (MI) was calculated in order to measure numerically the statistical relationship between the CBCT and the transformed CT after the two different procedures of image registration. The result of this measurement can be seen on table 2.5.

Mutual Information	Set 1	Set 2	Set 3	Set 4	Set 5
Rigid	1.024	1.091	1.094	1.087	1.088
Deformable	1.101	1.104	1.105	1.096	1.095

Table 2.5: *Mutual information measured after rigid and deformable registration for each set of patient images*

2.4.3 Discussion

After registering the CBCT images with the planning CT by means of rigid and deformable algorithms, the distance between landmarks iden-

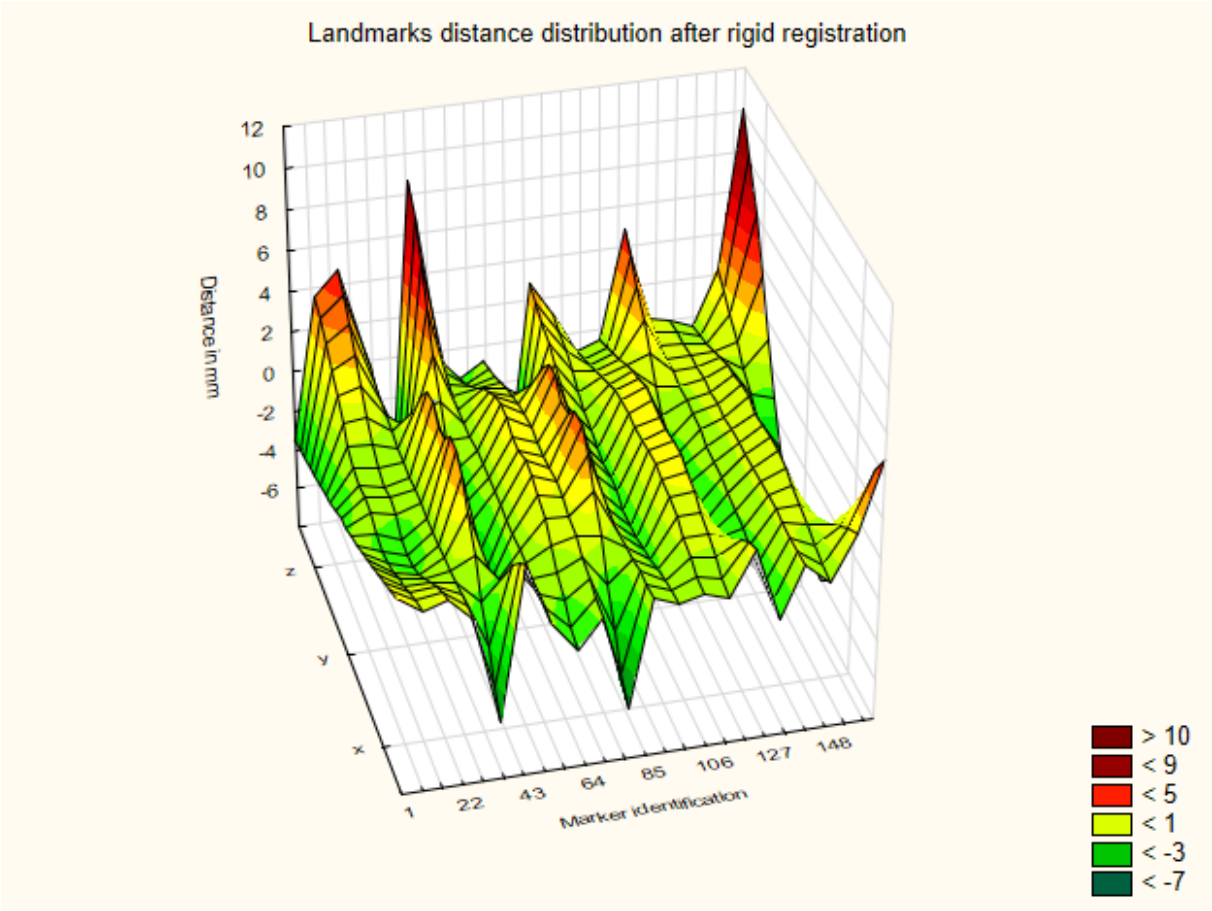

Figure 2.12: *Landmarks distance distribution after rigid registration in mm.*

tified by SIFT (around 35 per pair of image) were measured and those measurements show better performance of the deformable modality. The former assumption is also sustained by the calculated mutual information, which was always higher for our algorithm. The results presented for deformable image registration are derived from a landmark-based analysis used to validate CT deformations. The chosen method (SIFT) showed the residual distance of analogous points between the transformed CT and the fixed image. These identified landmarks are distributed over the 3D volume, thus SIFT represents an interesting tool for deformable registration evaluation, also to verify if rigid registration is enough or plan adaptation or re-planning are required.

Zhu et al. [ZGX12] used SIFT generated landmarks to orient DIR and obtained 85% of residuals errors bellow 2.0 mm. Rigaued et al.

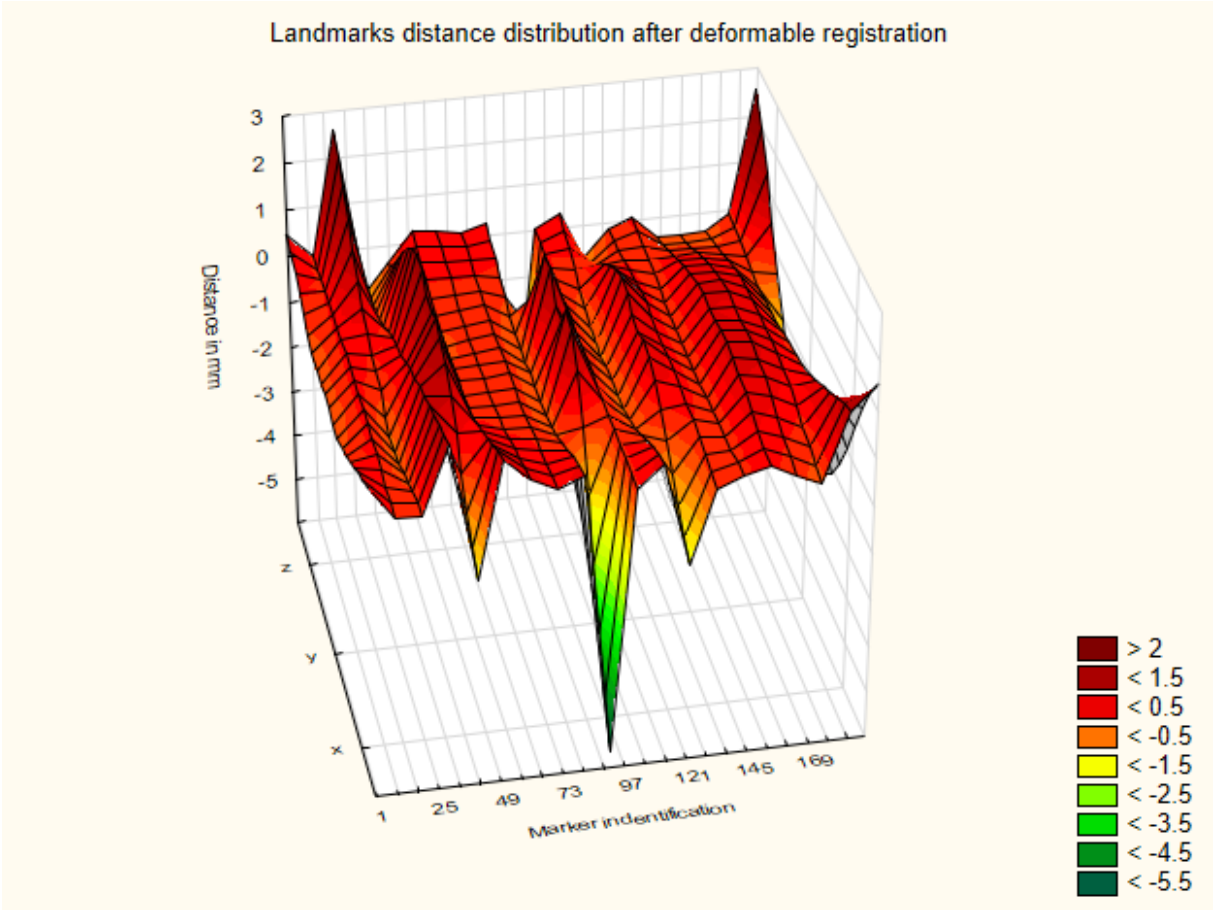

Figure 2.13: *Landmarks distance distribution after deformable registration in mm.*

[RSC+15] used observers detected landmarks and obtained a precision of 2.44mm±1.30 mm, while our results with automatic feature detection had all mean errors values withing the 1.0 mm threshold.

Previous studies for H&N cases show promising results for using CBCT as a support for dose recalculation and re-planning decisions. The results presented above for the DIR algorithm and recent bibliography [QSLY15, RAZ+16, STA+16, KOM+13] point out the potential of using CBCT and DIR for prostate cancer patients as well. With limited FoV CBCT, just the central part of the pelvis is taken into account (as seen on figure 2.9). This would then result in just an approximation for the actual anatomy of the patient. The region of interest (OAR + PTV) is contemplated, nevertheless areas adjacent to this region remain unchanged after the vector field correction. For radiotherapy, such

approximation might be valid, while it could lead to erroneous proton therapy dose distribution estimation due to the proton beam interactions, where range straggling is more significant than for photons regarding target tissues heterogeneities.

CHAPTER 3

Deformable image registration for adaptive radio and proton therapy

This chapter presents the application of deformable image registration algorithms, developed by the author, for adaptive therapy measures. DIR is proposed for such endeavor and tested for prostate and rectum cancer patients imaged with CBCT and CT-on-rail, respectively.

Image guided radiotherapy entails frequent imaging during treatment to enhance the accuracy in treatment delivery. The imaging workflow provides the ability to check changes occurring over the course of therapy, thus enabling potential treatment adaptation (adaptive radiotherapy - ART) [THT+16].

Cone-beam CT (CBCT) imaging has found widespread clinical application in recent years, in order to quantify volumetric changes which might influence CTV coverage and critical organ sparing [TBM+14]. Although it has lower image quality than CT, CBCT has the advantages of lower doses given to the patient and the possibility of imaging on the treatment couch. These benefits can be exploited to update the treatment plan [LNJ+13], following the ART concept [GYM13].

The basic requirement to implement ART is the ability to quantify the actually delivered dose in changing anatomy ("dose of the day" calculation), as a way to evaluate the need of a new CT image acquisition for treatment re-planning purposes [VJT+16]. Similar concepts can be potentially applied to proton therapy as well; at the current status, the implementation of treatment adaptation protocols is restrained by the reduced availability of volumetric imaging devices in proton therapy facilities [LND+15].

3.1 CBCT deformable image registration for prostate patients

This study proposes the use of CT-CBCT DIR for obtaining a CT-quality image with updated image of the patient for dose-of-the day evaluation.

The Image Registration (IR) process is used to quantify changes between daily CBCT images and the treatment planning CT. Deformable Image Registration (DIR) allows applying non-rigid transformation on the planning CT regarding any intra-fractional geometric change in patient's anatomy, thus enabling daily dose recalculation [VMM+14] and the evaluation of re-planning necessity.

Head and neck (H&N) and prostate cases have been studied and considered for the implementation of DIR using CBCT images. Recent works for H&N and prostate region show that deformable registration relying on CBCT-CT information could be useful for daily dose recalculation and dose accumulation analysis [VAA15, LND+15, FMM16, HCL+16].

The application of CBCT-CT DIR to prostate cases is extremely critical for the following reasons:

- Reduced field-of-view (FOV) CBCT might not include all the patient tissues traversed by the therapeutic beam, thus limiting the estimation of beam interaction with the new anatomy. This applies specifically to proton therapy, as large FOV CBCT are not yet available clinically. The first model with a 50 cm FOV (the previous standard was 26 cm) for proton therapy will soon be implemented [IBA]. A larger field will allow tracking changes in anatomical regions such as the pelvis.

- CBCT image quality in the pelvic region is a critical issue, due to the suboptimal image contrast in X-ray projections and to the significant scatter-to-primary ratio (SPR). Image quality is therefore expected to affect the performance of CBCT-CT DIR.
- Patient motion during image acquisition, x-ray scattering on the detectors, detectors efficiency and imaging artifacts, might result in inaccurate CT numbers [Per11].
- Large localized deformation for organs at risk around the prostate like (bladder and rectum , which is difficult to recover and might present large inter and intra fraction variability [HVP+11, LBH+06, SHR+14, AYF+13].
- Patient positioning takes a considerable time regarding the whole daily fraction delivery, as reproducibility in the pelvis region is hard to achieve [DTF+13]. Including acquisition of volumetric images and using them to estimate the occurred deformation (vector field) can be time consuming.

Treatment options for prostate cancer irradiation include both conventional X-ray radiotherapy and proton therapy. Radiotherapy with proton beam has brought promising when compared to conventional photons treatment [KKA+07, RDM+12, NHP+12, SM16], especially for sparing critical structures adjacent to the tumor [FND+15, SLM+14].To fully exploit the potential of proton therapy, submillimetric precision is required to avoid missing the target and overdosing healthy organs, which could drastically affect clinical outcomes.

Uncertainties of the proton beam dose deposition due to anatomy changes, regarding its dependency on the CT-based stopping power, can be addressed with repeated CT scans [LDZ+15], resulting, at least, in more dose delivered to the patient and elevation of time and costs to complete the treatment. DIR is an alternative to such issue. Due to differences between the patient position during the CT and when laid on the treatment couch, stands out the importance of in-room position techniques. Automated plan, contour adaptation and daily imaging for treatment update, result in therapeutic gains regardless of difficulties for these

methods implementation [MBF+14, LQL+13]. Contrasting the higher dose and the complexity of CT-on-rail, Cone-beam CT (CBCT) shows itself to be an interesting candidate for further investigation and development [VJT+16].

In this section, a CT to CBCT deformable registration method based on the ITK library is presented. An algorithm was developed to explore the soft tissue information of the CT-CBCT images to perform deformable registration, making efforts to overcome the poor signal-to-noise ratio that limits the CBCT usage for treatment planning purposes.

This present study proposes an overlook of the above-mentioned methods for prostate patients, due the evidence of positives outcomes from the treatment with protons [PMC+13, MHN+14]. As the prostate could move or presents deformations independently of the surroundings bone structure, taking into account soft tissue information could lead to a more precise treatment, since pelvic bone-based alignments may underdose the prostate in one-third of the fractions [FHS+13]. We specifically evaluated dosimetric results in 9 prostate cases undergoing repeated CBCT imaging, comparing the sensitivity of IMRT and IMPT treatment plans to anatomical changes. These analyses were based on QUANTEC (Quantitative Analysis of Normal Tissue Effects in the Clinic) guidelines, which summarize the dose/volume tolerance recommendations for treatment planning [MYJ+10].

To complement our visual assessment of performance, we use the Scale Invariant Feature Transform (SIFT) [Low04, CH09]. SIFT has shown itself to be an useful tool for DIR evaluation, as an automated way to find matching features between images and measure their residual distances following DIR application [PPR+13]. This study aims at DIR based on CBCT investigation as a clinical tool for radio and proton therapy.

3.1.1 Matherials and methods

3.1.1.1 Patient data

The planning CT from 9 patients and CBCT images acquired over the treatment course (28 in total) were selected from Hospital Albert Einstein

(SP-Brazil) database. The CT images were obtained with GE light speed multi slice, whereas CBCT images with Varian 23EX, both featuring a voxel size of 1.39, 1.39, 2.5 mm along RL, CC and AP directions, respectively. The PTV was defined with a 10 mm margin in anterior and lateral directions, and 7 mm expansion in the posterior direction with respect to the CTV. Patients were instructed to drink 500 ml of water 45 minutes before treatment and to follow a specific diet in order to avoid unintended increase in the rectum volume.

3.1.1.2 Deformable image registration

A C++ code based on the ITK Library [YAL+02] was developed by the author to create a method for deformable registration between CT-CBCT images of the same patient.

The first steps of the algorithm were rescaling the intensity of the CBCT image and applying a histogram-matching filter between both images to facilitate feature extraction with SIFT.

The selected metric was Mattes Mutual Information. As optimizer, we used the limited-memory Broyden-Fletcher-Goldfarb-Shanno (L-BFGS-B) [BLNZ95]. To handle the deformable transformation of the images, we configured the B-Spline interpolator in our algorithm. An example of DIR results can be seen in figure 3.1. Hereafter, vCT (virtual CT) stands for the deformed pCT (planning CT), i.e., the product of the DIR among the pCT and the CBCT. The virtual CT is meant to represent a CT image matching the anatomical features observed in the CBCT acquired during treatment.

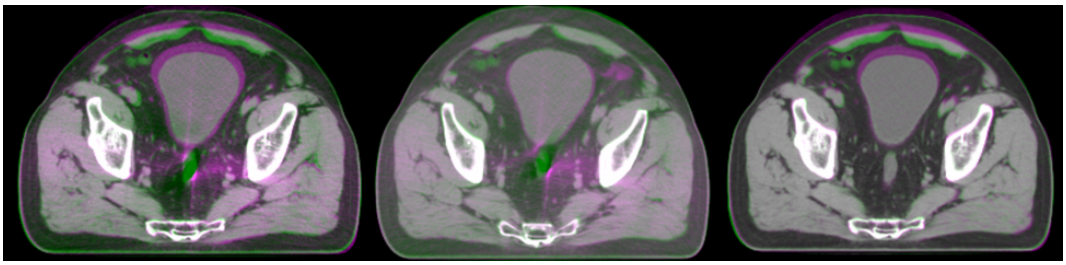

Figure 3.1: *Comparison in color overlay between: pCT-CBCT (left), vCT-CBCT (middle) and vCT-pCT(right).*

3.1.1.3 Scale Invariant Feature Transform (SIFT) for DIR validation

We used the n-dimensional scale invariant feature transform (SIFT) [CH09] method to extract and match features from each pair of fixed and moving images. SIFT allows the assessment of image registration results through residual errors evaluation at corresponding landmarks. After finding correspondent points between the CBCT and the transformed CT, the distance of each landmark pair was measured, thus providing the quantification of residual errors for each anatomical direction. The inverted vector field found during DIR was applied to matching points to measure their initial position at the planning CT, and quantify the similarity improvement through image registration. The landmarks obtained by SIFT feature extraction were distributed among soft and rigid tissue (figure 3.2). For the 9 patients, a delimited ROI (PTV+OAR) was used for SIFT measurements. Around 200 correspondent points were found for each pair of images (vCT-CBCT).

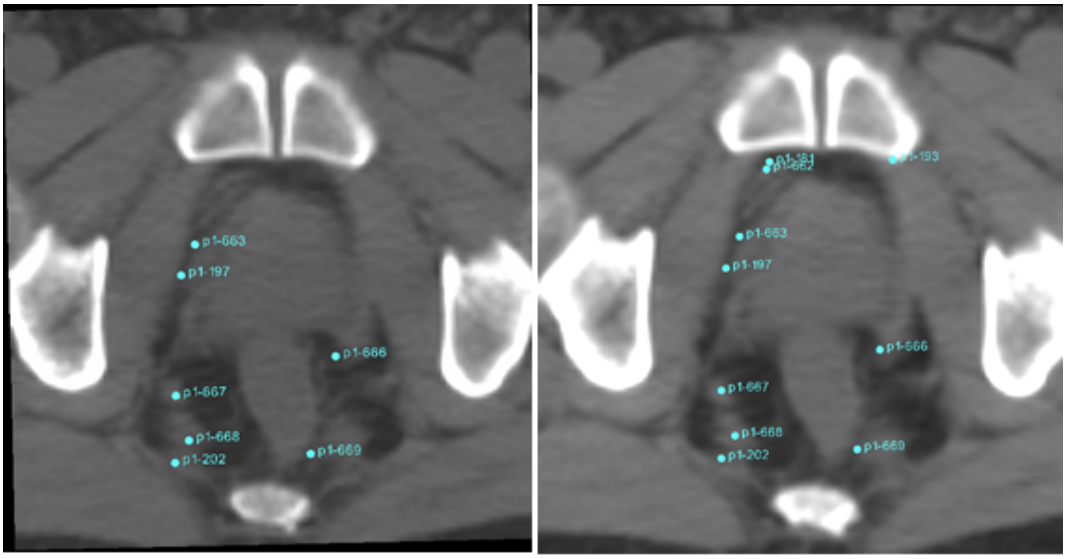

Figure 3.2: *Landmarks distributed over ROI: before DIR (left), after DIR (right).*

3.1.1.4 Planning CT warping

The vector fields obtained from the deformed registration were applied to the planning CTs and contours with the function warp of PLASTIMATCH [SSV+12b]. This procedure allowed the creation of a vCT with

new propagated contours, representing an updated anatomy of the patient.

3.1.1.5 Treatment planning and recalculation

We used 5-field IMRT plans for photons and 2 contralateral treatment fields IMPT plans for protons (figure 3.3). The dose prescription was 76 Gy, 2 Gy per fraction.

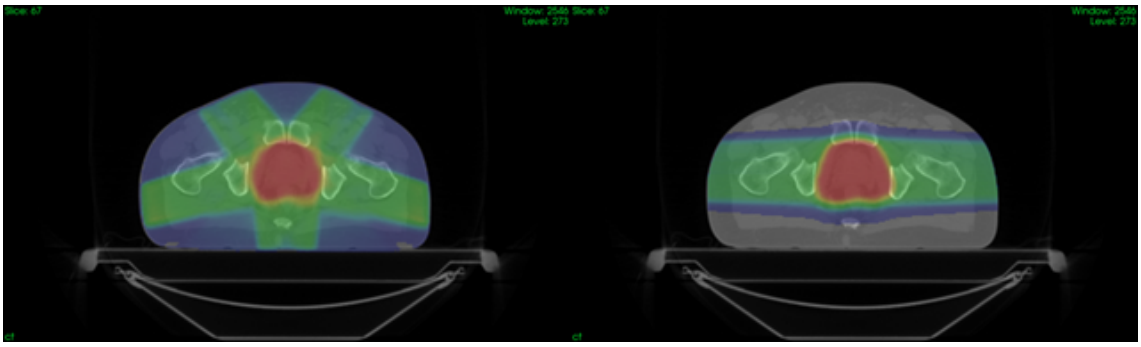

Figure 3.3: *IMRT plan (left), IMPT plan (right).*

The original plan was applied to the warped CTs to verify the delivered dose distribution in the deformed anatomy. For photons, the Eclipse (Varian Medical Systems - Palo Alto, CA) treatment planning software was used for IMRT planning and dose recalculation. For protons, RayStation6 (RaySearch Laboratories) was used for IMPT planning and dose recalculation.

Before IMRT dose recalculation, images were rigidly registered inside the TPS (treatment planning system) based on the PTV region, mimicking CBCT-guided inter-fraction adjustment for setup corrections.For IMPT recalculations, bone alignment was carried out to estimate change in the dose distribution after conventional rigid alignment (i.e. 2D-3D patient positioning without fiducials). The DVH (dose-volume histogram) evaluation was based on QUANTEC organs dose/volume tolerance summary [MYJ+10].

3.1.2 Results

3.1.2.1 Contour comparison (Dice coefficient)

A comparison bewteen planning CT and virtual CT contours was carried out. Dice coefficient measurements for PTV and rectum structures are presented in table 3.1. Automatically generated contours were, in general, adequate for DVH analysis since they followed the organ deformation (figures 3.4 and 3.5), requiring minor corrections for smoothing or as required from medical discretion. Patients 2 and 6 presented non full bladder during the planning CT acquisition, resulting in volumes differences up to 90 mL and 120 mL, respectively, compared to virtual CT bladder contours.

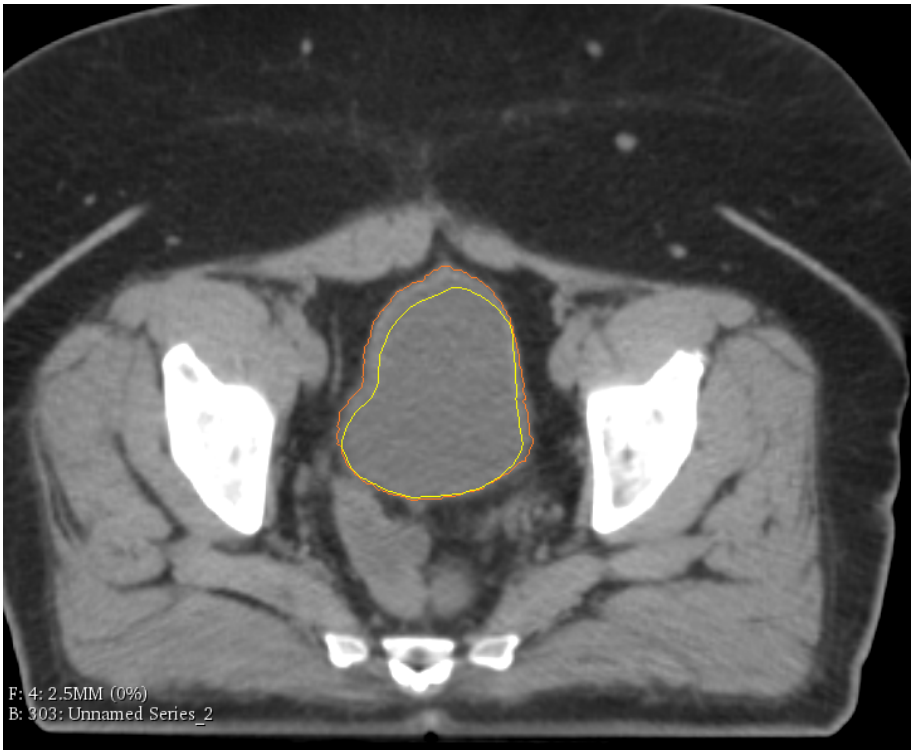

Figure 3.4: *Bladder volume variation from planning CT contour (yellow) to vCT automatically generated contour (orange).*

3.1.2.2 Deformable image registration validation

Correspondent points between CT and CBCT were identified and their distance calculated for each pair of images. Their distance distribution

Table 3.1: *Dice coefficient between planning CT and virtual CT contours.*

		CT 1	CT 2	CT 3	CT 4
		Dice coeff.	Dice coeff.	Dice coeff.	Dice coeff.
Patient 1	PTV	0,96	0,91	0,99	0,94
	Rectum	0,91	0,92	0,87	0,87
	Bladder	0,96	0,95	0,93	0,94
Patient 2	PTV	0,96	0,96	0,97	0,99
	Rectum	0,89	0,89	0,93	0,94
	Bladder	0,87	0,83	0,93	0,92
Patient 3	PTV	0,95	0,96	0,95	
	Rectum	0,87	0,90	0,89	
	Bladder	0,92	0,94	0,96	
Patient 4	PTV	0,97	0,97	0,97	
	Rectum	0,91	0,93	0,93	
	Bladder	0,97	0,97	0,96	
Patient 5	PTV	0,94	0,95	0,96	
	Rectum	0,84	0,87	0,92	
	Bladder	0,94	0,94	0,92	
Patient 6	PTV	0,95	0,95	0,95	
	Rectum	0,87	0,82	0,82	
	Bladder	0,9	0,86	0,78	
Patient 7	PTV	0,95	0,97	0,97	
	Rectum	0,91	0,88	0,92	
	Bladder	0,95	0,96	0,96	
Patient 8	PTV	0,96	0,97	0,96	
	Rectum	0,88	0,91	0,88	
	Bladder	0,95	0,94	0,91	
Patient 9	PTV	0,97	0,96		
	Rectum	0,93	0,92		
	Bladder	0,94	0,91		

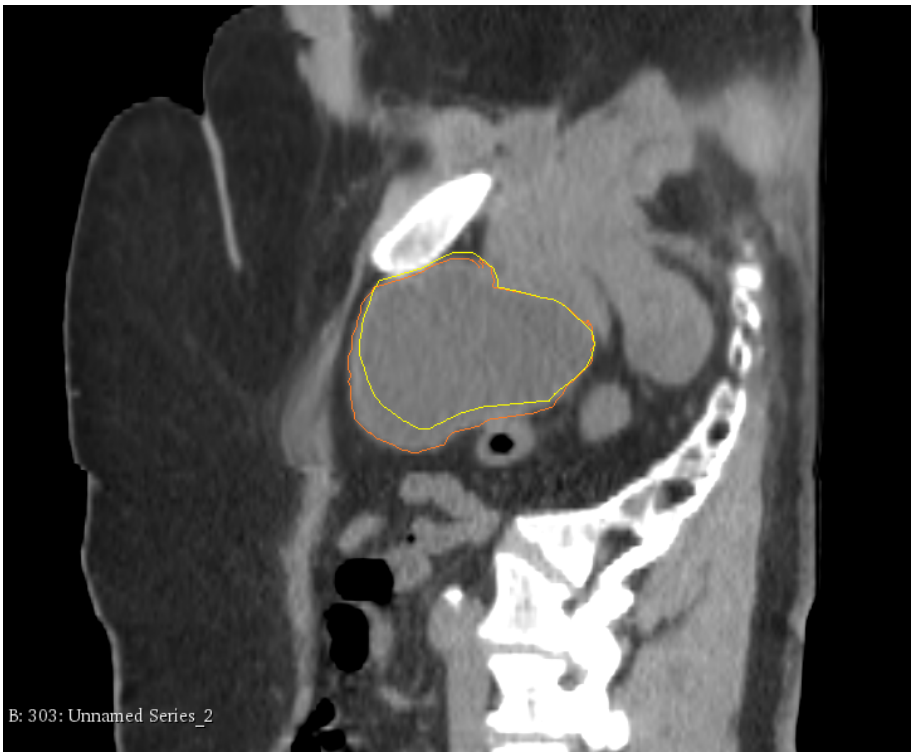

Figure 3.5: *Sagittal plane of vCT showing Bladder volume variation from planning CT contour (yellow) to vCT automatically generated contour (orange).*

before and after DIR can be seen in table 3.2. It can be noticed that after deformable registration most of the measured distances lay around the maximum voxel size (2.5 mm), with considerable corrections in comparison with initial position of landmarks.

3.1.2.3 Radiotherapy plan recalculation

For 8 patients, an increase in the rectum dose was observed: for 3 cases the increase was quantified as significant (QUANTEC constraints violation). The extreme case presented approximately (patient 6) V60 = 40%, V70 = 26% and V75 = 19% for rectum. This patient featured an elevated body mass, which implied more difficult position reproducibility and greater anatomical variations between fractions. The PTV presented loss of coverage in some cases, nevertheless the CTV was still receiving the prescribed dose, except for one case where the CTV DVH curve dropped to 75 Gy at 99% of the CTV volume.

Table 3.2: *Mean distance between landmarks before and after Deformable image registration.*

		CT 1		CT 2		CT 3		CT 4	
		Mean	Std	Mean	Std	Mean	Std	Mean	Std
Patient 1	Before	4,23	4,02	5,36	1,23	4,56	3,76	4,60	3,78
	After	2,33	1,30	1,72	1,48	1,69	1,04	2,07	1,18
Patient 2	Before	3,70	4,14	4,13	4,44	3,75	4,29	3,66	3,98
	After	1,87	1,02	1,62	1,02	1,84	1,46	2,09	2,05
Patient 3	Before	3,24	4,65	4,22	4,13	4,57	3,82		
	After	1,51	1,34	1,47	1,22	1,83	1,46		
Patient 4	Before	4,09	4,43	4,15	4,30	4,26	4,54		
	After	1,55	1,57	1,62	1,51	1,73	1,76		
Patient 5	Before	3,13	3,49	3,56	3,92	3,27	3,77		
	After	1,92	1,53	1,53	1,45	3,15	1,39		
Patient 6	Before	3,65	4,07	3,06	3,90	3,75	4,36		
	After	1,58	1,46	1,78	1,60	2,25	0,98		
Patient 7	Before	3,21	2,49	3,34	2,30	2,54	3,48		
	After	1,67	1,37	1,66	1,32	1,82	1,47		
Patient 8	Before	3,91	4,13	4,50	4,25	3,95	3,85		
	After	1,42	0,72	1,68	0,85	2,02	1,29		
Patient 9	Before	2,80	3,28	3,03	3,67				
	After	1,55	1,06	1,64	1,25				

Table 3.3: *DVH comparison at the rectum for figure 3.6 case.*

	IMRT		IMPT	
	Plan (%)	Recalc (%)	Plan (%)	Recalc (%)
V60	28,1	32,3	25,0	28,2
V65	22,4	27,1	19,9	23,3
V70	16,0	22,7	13,0	17,4
V75	10,3	15,1	4,4	7,0

3.1.2.4 Proton therapy plan recalculation

The tendencies of DVH modifications follow the above-mentioned results for IMRT. For contralateral proton treatments, patient weight loss and femoral head rotation affected directly the ranges of the beams. In figure 3.6 an example of dose difference between planned and recalculate dose due to weight loss is shown. The local tissue reduction along the beam line path was up to 8 mm. The differences in dose received by the rectum for this case is presented in table 3.3.

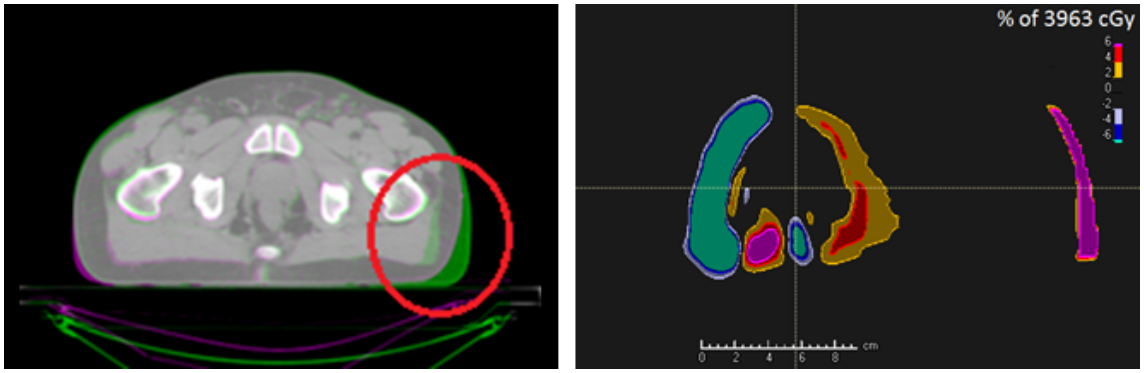

Figure 3.6: *Anatomy difference due to weight loss (left), shown in color overlay. Dose difference for plan recalculation on the correspondent vCT.*

Another noteworthy case presented rectum circumference reduction, resulting in prostate movement in posterior direction and PTV coverage loss (approx. 63 Gy at 99% of PTV volume). This PTV loss implied also a minimum dose reduction at CTV from 76 to 71 Gy (less than 95% of the prescribed dose). The DVH for this case's rectum is presented on table 3.4.

Assuming daily image guidance (soft-tissue target for photons and bony anatomy for protons), the PTV margin used in this study was still

Table 3.4: *DVH comparison at the rectum for independent prostate motion case.*

	IMRT		IMPT	
	Plan (%)	Recalc (%)	Plan (%)	Recalc (%)
V60	27,1	31,2	30,9	19,9
V65	19,3	22,6	20,9	10,8
V70	11,1	22,6	20,9	10,8
V75	3,5	5,1	3,8	0,2

Table 3.5: *Dose comparison (gamma test) between recalculated and planned dose. Pass fraction presented in % for the 9 patients.*

	Pass fract. (%) CT 1		Pass fract. (%) CT 2		Pass fract. (%) CT 3		Pass fract. (%) CT 4	
Pat.	Photon	Proton	Photon	Proton	Photon	Proton	Photon	Proton
1	97,31	97,52	94,45	93,70	97,23	80,70	93,00	86,67
2	98,33	92,32	93,05	92,93	96,31	93,06	90,76	99,40
3	96,53	94,00	97,13	96,08	97,25	81,90		
4	98,69	94,90	98,36	96,23	98,11	97,93		
5	92,66	94,13	92,92	94,06	93,76	94,06		
6	95,06	94,08	95,94	86,94	97,92	96,05		
7	96,59	90,37	92,83	95,38	97,89	91,40		
8	94,97	96,96	93,75	94,53	97,35	90,95		
9	94,88	96,28	97,08	94,78				

sufficient to assure the prescribed dose delivery to the CTV, except for one patient.

3.1.2.5 Dose comparison (gamma test)

Each recalculated dose was compared with its correspondent treatment plan dose. The distance-to-agreement criteria used was 3,00 mm, the dose difference criteria was 3,00 % and the threshold for gamma voxel values calculations was from 10,00 % of the maximum treatment planning dose. These results (table 3.5) might also represent another form of deformation quantification in the irradiated volume.

3.1.3 Discussion

A deformable registration algorithm based on ITK library was developed and tested in 9 prostate cancer cases: the code was validated for CT-CBCT DIR. The automatically propagated contours required small

or no corrections, therefore being, at least, a good starting point for fast recontouring the vCT, allowing online DVH verification. The lower Dice coefficients found for rectum and bladder structures comparisons are in agreement with the results obtained after dose recalculation, where differences in dose distribution were observed due to anatomical variations. When comparing vCT vs. treatment planning CT contours, difference were mostly local, i.e. limited to specific regions. This was also confirmed by Dice coefficient results, which were above 0.78 (Patient 6, bladder contour). Such a results justified the local measurement of the occurred deformation relying on landmarks, as reported for deformable image registration validation.

Residual mean errors, measured relying on automatically extracted landmarks, featured the same magnitude as the voxel size, as opposed to initial deformation exceeding 5 mm on average in worst cases 3.2. Image resolution is clearly a limiting factor in landmark localization, as landmark distances below 1 voxel cannot be determined. Such a result is optimal at the available image resolution, but it would require further assessment for proton therapy plans, since the 2.5 mm voxel size might be insufficient for accurate planning. Automatic landmark extraction should be therefore applied to higher resolution datasets to achieve adequate confidence on reported results for proton therapy plans. For both modalities (protons and photons), the rectum is susceptible to structural variations, which may result in early excessive damage of acute-responding component of rectal wall, and might contribute to the initiation of late rectal injury [WLC$^+$98, MGJ$^+$10]. Therefore, DIR and dose recalculation are important tools for dose distribution verification in organs at risk, in order to avoid future complications and lesions. For photons, IMRT plans with 5 treatment fields, recalculated on the vCTs, demonstrated robustness for PTV coverage, given the realisation of prostate position-based rigid alignment prior to each fraction. Such a results can be achieved relying on daily image guidance with volumetric CBCT, and/or with implanted landmarks/transponders. For protons, contralateral fields were used, assuming daily image guidance with bony anatomy matching, as currently available in the majority of treatment facilities. Patient anatomical changes on the beam path could result in

significant loss of PTV coverage and rectum dose increase, due to proton physical properties. For the studied cases, the used PTV margins were sufficient to assure the prescribed dose delivery to the CTV, except for one vCT, where prostate motion and femoral head rotation contributed to a significant difference in the dose given to the CTV. This suggests that the availability of CBCT imaging in proton therapy facilities may be beneficial, as this would allow soft tissue imaging in the treatment room. Yang et al. [YLA+14] proposed a method of combining online and offline strategies to address anatomical and weight changes as those verified in our study. This method allows comparable results to online plan adaptation with considerable less effort. Our approach presents vCT as an alternative to in-room CT for this type of plan adaptation, provided that CBCT imaging is available. Previous studies for H&N results shows promising results for using CBCT as a support for dose recalculation and re-planning decisions. Our results point out the potential of using CBCT and deformable registration for proton therapy prostate patients, despite limitations of CBCT imaging in the pelvic region.

3.2 CT-on-rail deformable image registration for rectum Patients

This study presents the use of a DIR method, developed by the author, to automatically propagate contours over CT-on-rail.

At Trento (Italy) proton therapy center, there is a CT-on-rail inside one treatment room. This gives the possibility of high quality image acquisition with the patient on the treatment couch. This image might be used for patient positioning also for anatomy changes verification. Due to structural changes, finite range particle beams, such as protons, might present significant dose distribution difference when compared to treatment plan after interacting with the new path.

Therefore, CT-on-rail can provide up-to-date information regarding patient anatomy, which can be used for online dose verification and serve as a useful tool for decisions over treatment following steps. DIR is an appropriate and time-saving method for contour propagation in repeated CTs [RPH+15]. To facilitate DVH analysis and online plan adaptation, a

method of automated contour propagation was developed and tested for CT-CT-on-rail rectum patients images.

3.3 Materials and methods

3.3.1 Dataset

In this study, sets of images from 3 rectum patients were included. For each patient, one planning CT and 2 CT-on-rail scans were available.

3.3.2 DIR and contour propagation

A self-developed deformable image registration code based on ITK library (same described on previous section) was used.

For speeding up and increase the performance of the image registration procedure, an ROI (region of interest) was defined, as depicted in figure 3.7, which comprehends the region traversed by the treatment beams. For rectum proton therapy, usually, the beams are contralateral and posterior directions or just oblique on posterior direction.

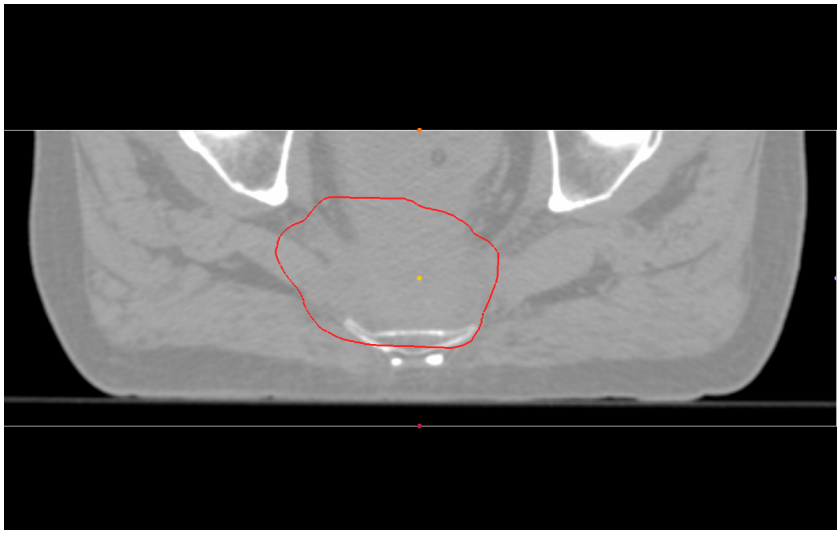

Figure 3.7: *Region of interest defined for performance enhancement of deformable image registration.*

The vector fields derived from the DIR between CT and CT-on-rail images were applied to the treatment planning contours with PLASTIMATCH [SSV+12b].

Table 3.6: *Gamma index comparison for planned and recalculated doses.*

Patient 1		Patient 2		
OR1/DEF1	OR2/DEF2	OR1/DEF1	OR2/DEF2	OR2/DEF3
100%	99,87%	99,27%	99,54%	99,99%
Plan/OR1	Plan/OR2	Plan/OR1	Plan/OR2	Plan/OR3
90,82%	88,40%	98,15%	98,04%	100%
Plan/DEF1	Plan/DEF2	Plan/DEF1	Plan/DEF2	Plan/DEF3
92,01%	90,02%	100%	99,18%	99,60%

3.3.2.1 DIR validation

To validate the DIR procedures, we investigated dose comparison by means of gamma analysis between the dose recalculated on CT-on-rail and the dose recalculated on the virtual CT (transformed CT after DIR between CT and CT-on-rail). The treatment plans were made on RayStation 6, based on a 53 Gy prescription distributed over 28 fractions, composed of two posterior and obliques beams (160° and 200°).

3.3.3 Results

3.3.3.1 DIR validation

The recalculated dose over the CT-on-rail and virtual CT were compared (figure 3.8) and are presented in table 3.6. The comparison was made between Plan (treatment planning dose), OR (dose derived from treatment plan recalculated on the CT-on-rail) and DEF (dose derived from treatment plan recalculated on the deformed planning CT). Gamma index was used with a 3mm/3% criteria. The good agreement (always greater than 99%) between the DER and OR demonstrates the similarity of anatomies. Even if the CTs where acquired with different scans and on different days, the DIR brought the planning CT to a similar geometry of the CT-on-rail scan.

3.3.3.2 Propagated contours

The vector fields obtained from the DIRs between the planning CTs and the CT-on-rail images where applied to the treatment planning contours to generate new sets which represent the updated anatomy of the patient.

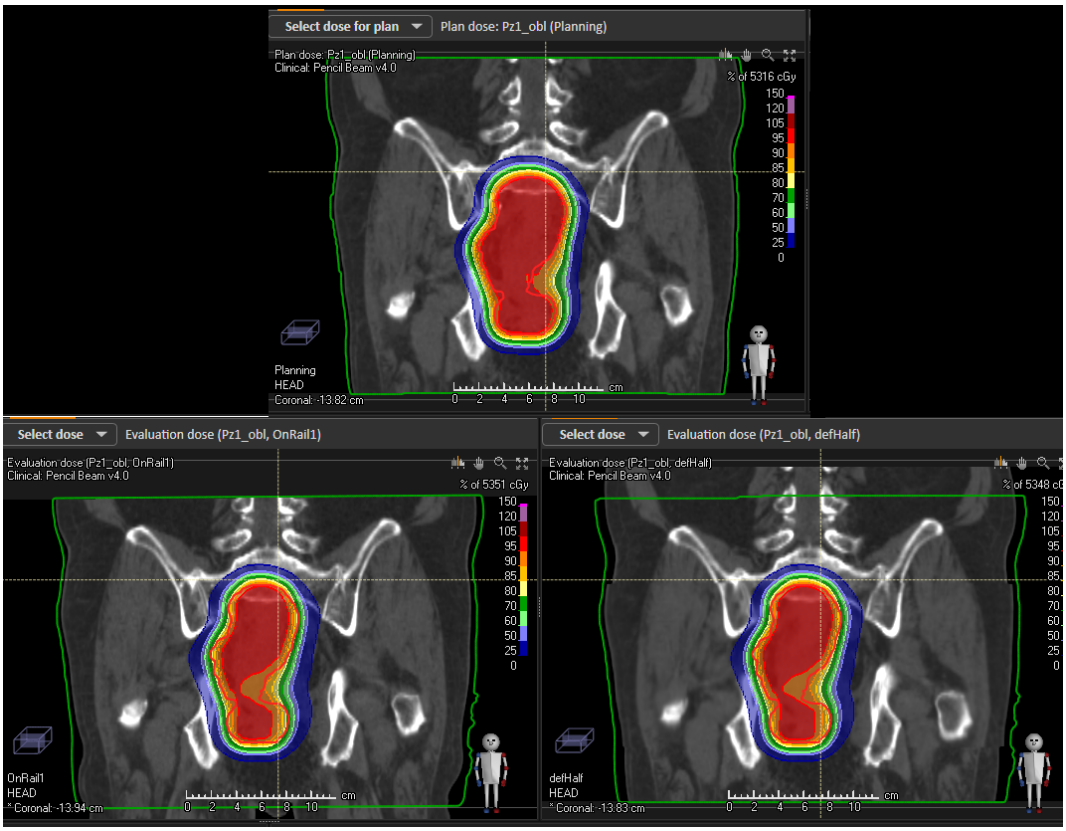

Figure 3.8: *Dose distribution comparison. Treatment planning CT (upper figure), CT-on-rail (bottom left) and virtual CT (bottom right).*

The contours where evaluated by a radiotherapist and judged as useful after few corrections, serving as a good starting point for online DVH verification and sparing lots of efforts with re-contouring.

3.3.4 Discussion

The described study points out the usefulness of CT-CT-on-rail DIR for automatic contour propagation for rectum patients. A geometric validations was not carried out, as visual and gamma index assessment proved to be sufficient. In proton therapy, changes in patient anatomy could result in disastrous dose distribution and target miss. By introducing the adaptive therapy concept, an online verification can be made prior to irradiation to verify target coverage and OAR sparing. To make the procedure faster, the automation of the re-contouring is an interesting alternative.

The new contours might present a few inconsistencies which can be easily corrected in a much faster fashion when compared to re-contouring (considering also time spent in DIR). These propagated contours can be used for DVH analysis of the recalculated dose on CT-on-rail to support online decisions made by the radiotherapist, contributing then to an adaptive proton therapy framework implementation.

3.4 Alternative IR methods

Different open-source methods for IR based on ITK library has been developed. For example, IR can be performer with: PLASTIMATCH [SSV+12a], 3D Slicer [KPV14] and Elastix [KSM+10]. Elastix features a great deal of algorithms that are frequently used to solve IR problems, allowing the user to configure and test different registration methods for a specific application. Due to its noteworthy range of possibilities and efficiency, a case from section 3.1 was chosen for a simple comparison between the code developed by the author and Elastix under similar configuration. This comparison is shown in figures 3.9, 3.10 and 3.11.

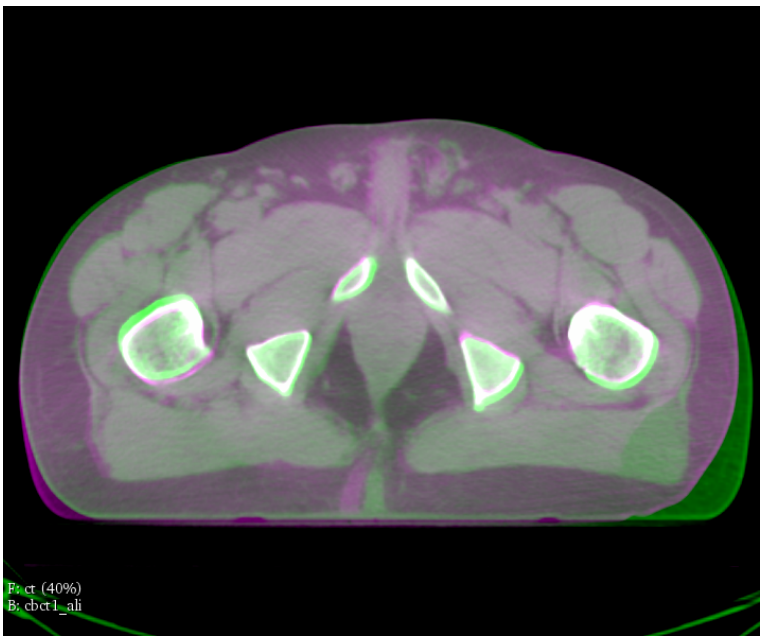

Figure 3.9: *Comparison of planning CT and CBCT before DIR.*

SIFT was applied to automatically detect landmarks and measure their residual distances after DIR as described on 3.1. Comparing the CBCT

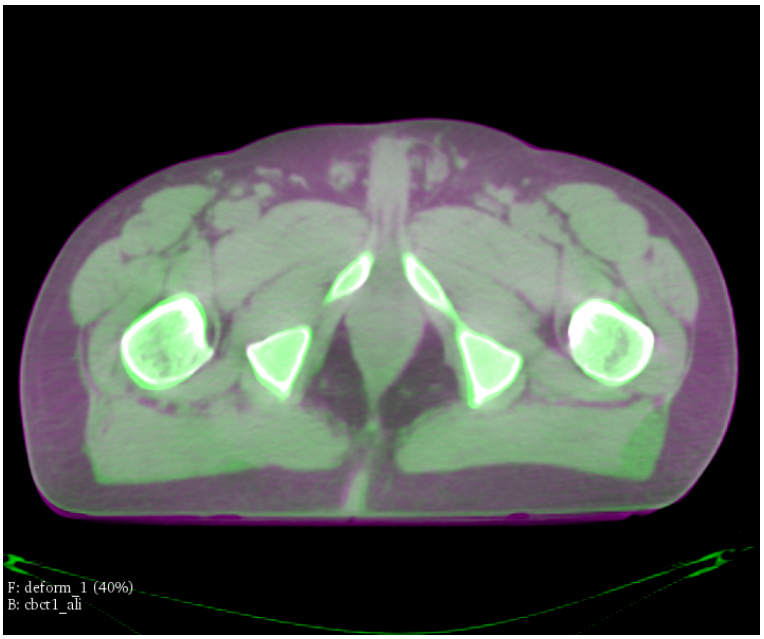

Figure 3.10: *Comparison of virtual CT produced by author's code and CBCT after DIR.*

and the virtual CT produced by the author's code, SIFT found 233 landmarks on each image with a mean distance of 2,33 and a std of 1,30 mm. For the Elastix output, SIFT found 121 landmarks and their mean distance was 2,27 with a std of 1,25 mm. The greater number of landmarks found by SIFT for the author's method might be due to increased anatomic similarity. The IR results found are similar, as both methods rely on ITK library. The advantage of self-developing a code is to have full control of every single step and the possibility of adding filters and visualization of images during the IR process.

During this PhD, besides basic DIR settings, the author added to his code:

- Histogram matching filter to improve SIFT outcomes and allow better IR depending on the optimizer.
- Diverse options for dealing with image intensity, such as: measuring, redefining minimum and maximum, rescaling and equalizing the histogram.
- Filters for image re-orientation in case of divergence between fixed

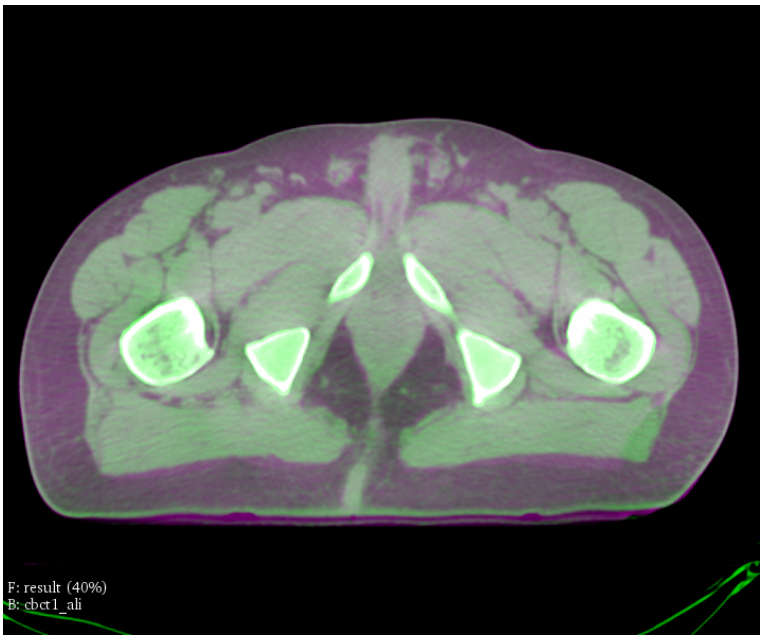

Figure 3.11: *Comparison of virtual CT produced by Elastix code and CBCT after DIR.*

and moving image coordinates.

- An option for changing DICOM origin, useful when a systematic difference is known.
- Integration with VTK [SML96] for image rendering and 3D visualization during any desired part of the IR procedure. Examples can be seen on figures 3.12, **??** and **??**.

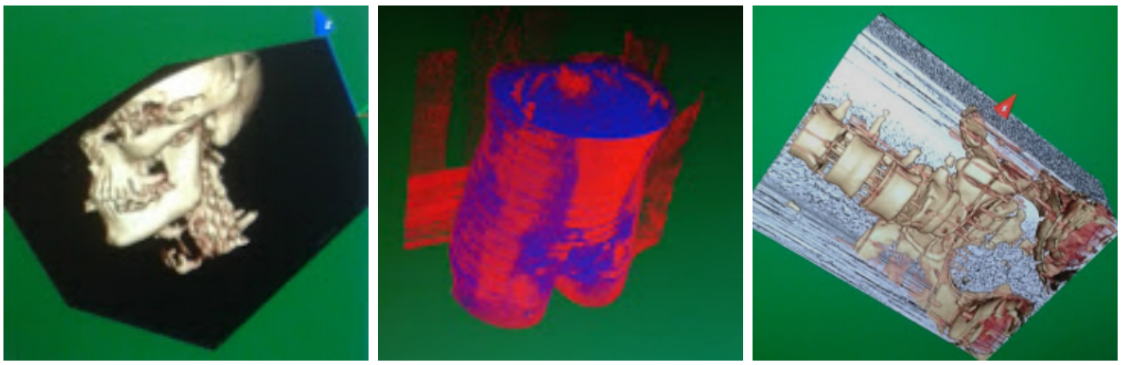

Figure 3.12: *Rendering of: planning CT image for a H&N patient (left), CT image of a phantom (middle) and CT-CBCT pre-alignment with bone visualization (right) inside author's code.*

CHAPTER 4

Image processing for proton CT

In this chapter, different methods were tested for pCT reconstruction pre and post-processing stages, allowing comparison of spatial resolution and RSP values for proton images reconstructed.

The prototype pCT scanner, built by the pCT collaboration, consists of a tracker system used to extrapolate the proton path before and after the object and a multi-stage scintillator (MSS) allowing the measurement of the proton residual energy, which is converted to water equivalent path length (WEPL) [HSB$^+$12]. The scanner is installed on a horizontal proton beam line and the object is positioned on a rotating stage. The tracker and MSS data of individual protons are read out by a custom high-speed data acquisition (DAQ) system, capable of handling data rates on the order of 1 million protons/second [CBH$^+$13, SJM$^+$13]. In order to determine WEPL, the MSS detector response is calibrated using a dedicated calibration phantom [Par14]. The reconstruction for a high quality pCT image can be achieved in under 7 minutes [KDOn$^+$13]. Conversely, images generated after FBP without further refinements of RSP values can be obtained within 1 minute, which is compatible with patient setup workflow.

For the reference pCT scan, ninety projections of a pediatric head phantom (model 715-HN, CIRS) were obtained with the prototype proton CT scanner built by the pCT Collaboration [SJM+13]. A total number of about 200 M protons entered the reconstruction process, which employed a filtered back projection (FBP) algorithm as the initial step, followed by 5 iterations of TVS-DROP [PSM+10]. These reconstructed images were then combined into a 3D DICOM image 4.13 with a voxel size of 0.58, 0.58 and 1.25 mm for LL, AP and CC respectively. The dose to the head phantom corresponding to 100% was estimated by scanning a 16-cm acrylic head phantom (Catphan model CTP 554) with a PTW Farmer ionization chamber inserted at its center while using a similar total number of proton triggers and scanning time. The dose to the phantom center was measured to be 1.45 $\pm$-0.3 mGy (mean value and standard deviation of two independent measurements) [GGZ+16].

4.1 Methods for evaluation of pCT image pre and post-processing

The FBP algorithm is used before the iterative proton CT reconstruction procedure as a fast tool to determine the object boundaries for the subsequent proton path estimations, but it gives rise to image artifacts, which remain even after many iteration cycles. Fast data processing and the inclusion of appropriate handling of the initial boundary image are two important aspects of raw data pre-processing. A detailed flowchart of pCT image reconstruction is presented in figure 4.1.

4.1.1 Threshold method

To reduce the artifacts induced by the initial FBP reconstruction, thresholds were used to obtain the initial boundary image, so that RSP values higher than this defined limit are set to 1, whereas lower values are set to 0 (figure 4.2).The comparisons of the output images and the RSP values of the Catphan CTP 404 phantom (Sensitom), for different thresholds and iterations are shown on figures 4.3 and 4.6, respectively.

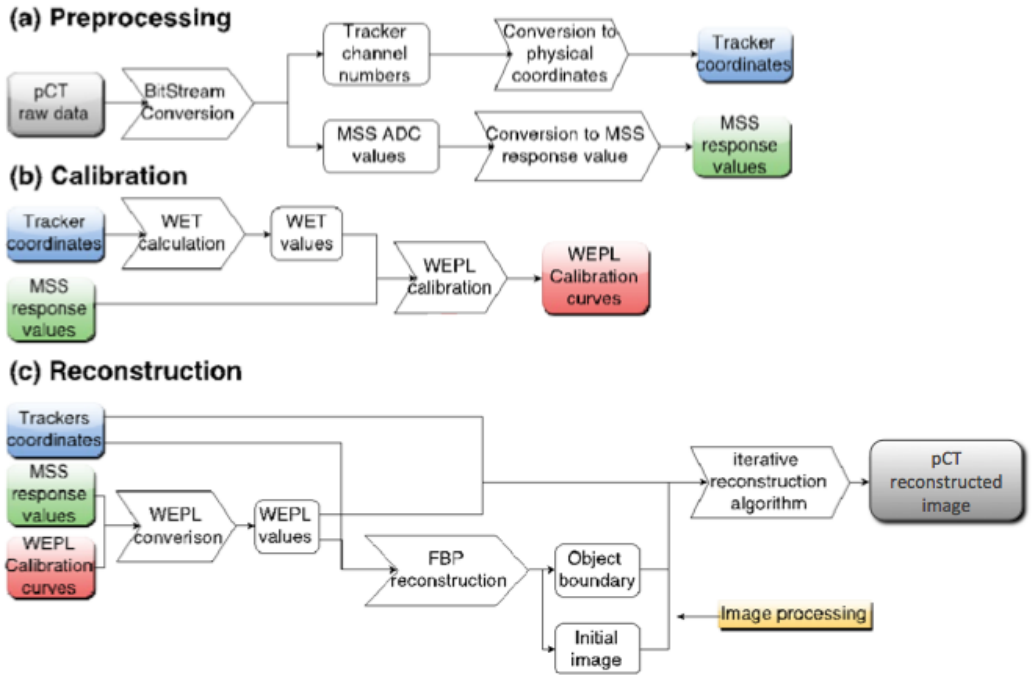

Figure 4.1: *Flowchart of pCT image reconstruction.*

4.1.2 Mean filter method

A mean filter was tested in order to reduce pCT image noise. Instead of checking only the RSP value of the single pixel, the 8 pixels around it were also taken into account. The mean filter is presented on the math expression 4.1, where (x,y) is the pixel of interest. If the values analyzed are under the defined threshold values for RSP (0.6, 0.65, 0.7) for all of the 9 pixels, the central pixel value goes to 0. If all surrounding values are above the threshold, the central pixel value goes to 1, otherwise the average value of all 9 pixels is used.

$$\begin{matrix} (x-1,y+1) & (x,y+1) & (x+1,y+1) \\ (x-1,y) & (x,y) & (x+1,y) \\ (x-1,y-1) & (x,y-1) & (x+1,y-1) \end{matrix} \tag{4.1}$$

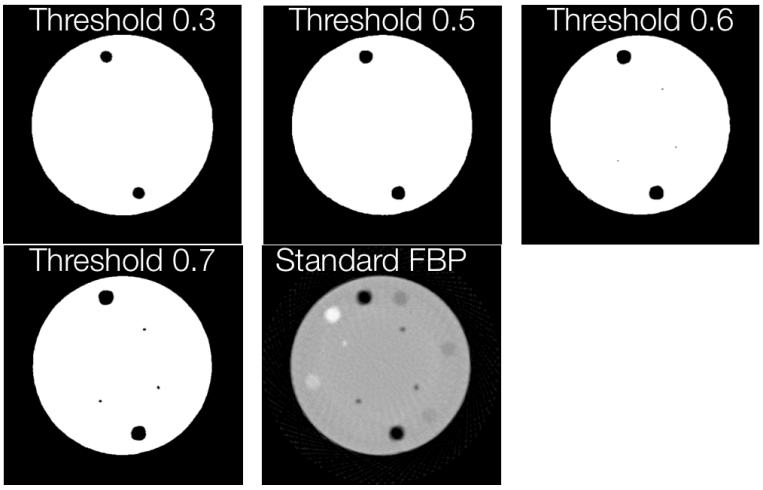

Figure 4.2: *CTP404 boundaries obtained with different RSP thresholds and the FBP standard method with no iterations.*

4.1.3 Gaussian blur filter method

The FBP projections for pCT, despite presenting good RSP values, result in noisy images. A Gaussian blur filter with a kernel of 7x7 and a sigma of 2.0 was implemented immediately after the FBP method as an attempt to reduce noise before the iteration processes for further image quality and RSP refinement.

4.1.4 Post-processing for FBP method with 10 iterations

The standard pCT reconstruction algorithm previously mentioned produces a string of images. It was changed in order to produce separated images for each slice of the scan. After creating the 3D volume of the scanned pediatric head phantom some post-processing steps were applied in order to reduce noise, re-orient to the standard CT orientation and convert the data format to float. Those steps contribute to more suitable images for treatment planning and image registration.

In this study a mask was created on the region of the head phantom, thus applied in order to eliminate the external noise. For the inner noise reduction, a Gaussian blur filter was used.

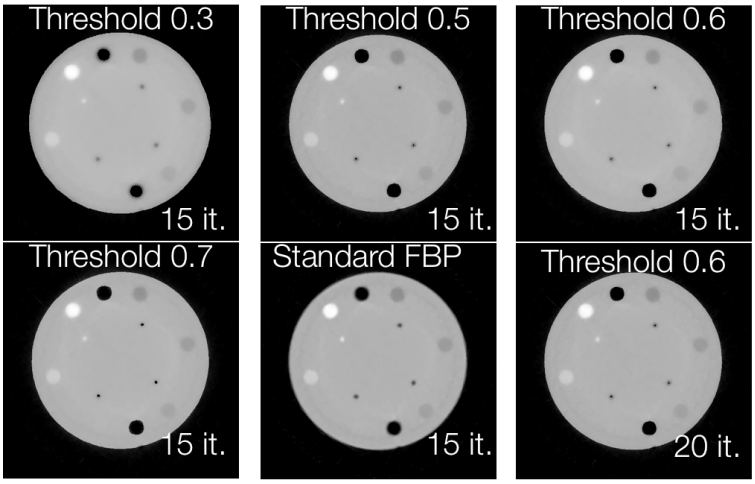

Figure 4.3: *CTP404 pCT reconstructed images with different threshold values compared with the FBP standard method with no filter.*

4.2 Results for pre and post processing methods

4.2.1 Threshold method

Figure 4.4 presents a slice of the pediatric head phantom (model 715-HN, CIRS) reconstructed with FBP and 10 iterations, the boundaries and the reconstructed images after 15 iterations can be seen in figure 4.5.

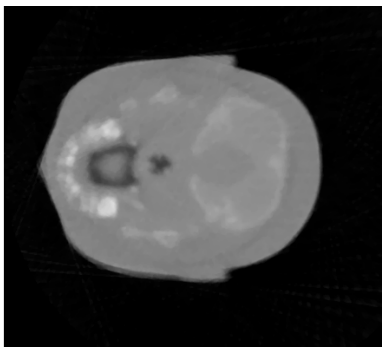

Figure 4.4: *Pediatric head phantom image reconstructed with the FBP algorithm and 10 iterations.*

This method presents artifacts reduction, although, to get acceptable RSP values many iterations are required (at least 15), resulting in a large computational time. Higher thresholds give better RSP values and lower thresholds give better contrast (outside artifacts practically disappear).

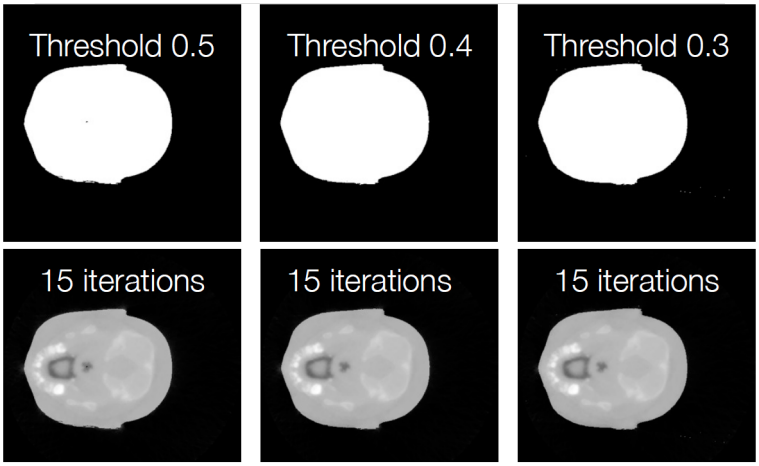

Figure 4.5: *Boundaries and reconstructed images of the pediatric head phantom using the threshold method.*

After using this threshold method, the cylindrical inserts inside the phantom assume non-rounded shapes.

The 0.6 threshold seems to be the optimal value, and after 20 iterations the RSP values show acceptable deviation from the reference values. With the standard FBP method the RSP values are closer to the reference values, but the image still presents artifacts even after 15 iterations.

4.2.2 Mean filter method

The Catphan images were evaluated using different 3 thresholds values for RSP (0.6, 0.65, 0.7) with 20 iterations in combination with the average filter (as visible in figure 4.3). The RSP values obtained were compared with those from the standard FBP method and the reference values. The comparison of RSP values is shown in figure 4.8. Figure 4.7, presenting images obtained with different thresholds and with or without mean filters.

The average discrepancy of the results obtained regarding the reference ones can be seen in table 6.1. This method results in smoother borders for both the Catphan and the head phantom (pediatric CIRS head phantom), and the RSP values are better than just using the threshold method. Nevertheless the RSP values are closer to the reference values with the standard FBP algorithm.

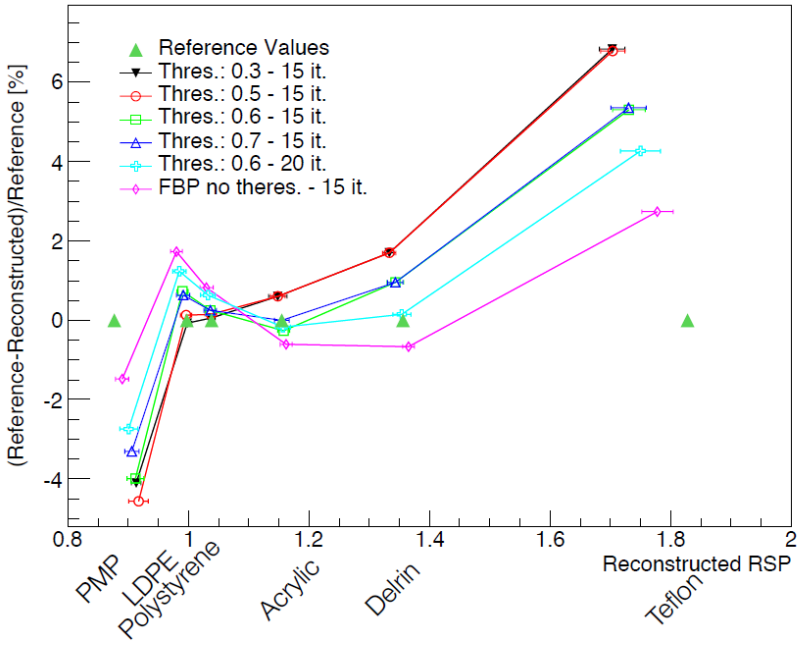

Material	RSP reference value
PMP	0.877
LDPE	0.9973
Polystyrene	1.0386
Acrylic	1.155
Delrin	1.356
Teflon	1.828

Figure 4.6: *RSP values obtained with the threshold method comparison with reference values.*

4.2.3 Gaussian blur filter method

The implementation of a Gaussian blur filter, as described, resulted in smoother FBP images, with less artifacts and RSP values comparable to those obtained by the Standard FBP method used so far(figure 4.9).

This filters allows significant artifacts reductions with less iterations (figure 4.10).

The RSP values were measured for different number of iterations, with and without the Gaussian filter, as shown in figure 4.11.

The average discrepancy of the RSP values with and without GB (Gaussian Blur) filter compared to the reference values can be seen on table 6.2.

4.2.4 Post-processing for FBP method with 10 iterations

The comparison of the image produced with the FBP method after 10 iterations and after the above mentioned post-processing can be seen in figure 4.12.

The 3D volumes of the reconstructed and post-processed pCT images

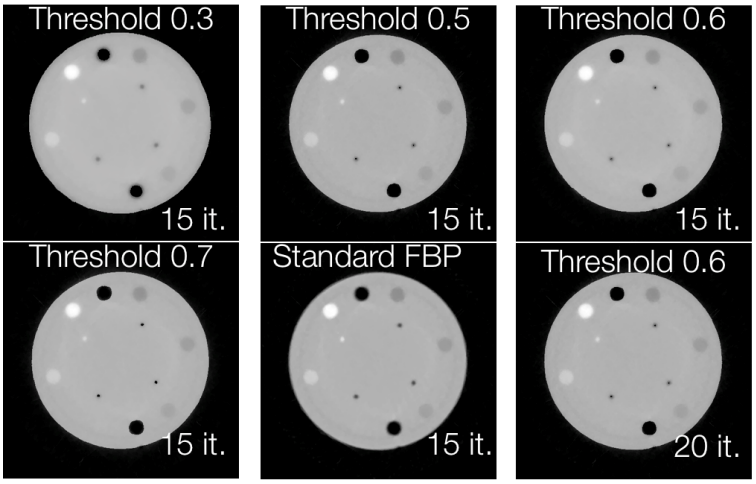

Figure 4.7: *CTP404 pCT reconstructed images with different thresholds and mean filter, compared with the FBP standard method with no filter.*

Threshold	Number of Iterations	Average Discrepancy
0.3	15	2.23%
0.5	15	2.32%
0.6	15	1.92%
0.7	15	1.75 %
- (FBP)	15	1.34%
0.6	20	1.53%
0.6+filter	20	1.34%
0.65+filter	20	1.35%
0.7+filter	20	1.37%

Table 4.1: *RSP % error for the mean filter method.*

are shown in figure 4.13.

Significant noise reduction and image quality improvement was observed with the implemented post processing steps The produced 3D Dicom images serve for subsequent studies of patient positioning and proton treatment planning directly on RSP pCT images.

4.3 Pre and post processing discussion

A few methods for pre and post-processing of pCT images were tested and the results serve as basis for later studies, aiming at future clinical implementation.

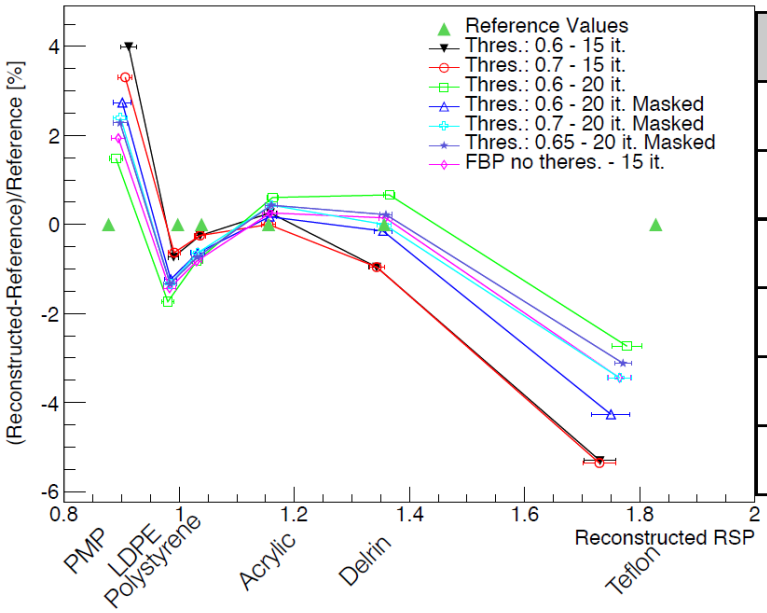

Material	RSP reference value
PMP	0.877
LDPE	0.9973
Polystyrene	1.0386
Acrylic	1.155
Delrin	1.356
Teflon	1.828

Figure 4.8: *Obtained RSP using the threshold method with average filter compared with reference values.*

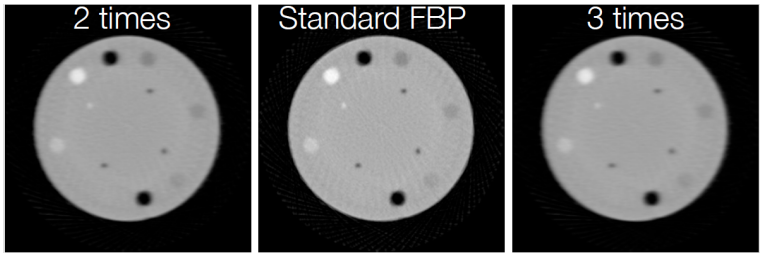

Figure 4.9: *Sensitom pCT images after aplying the gaussian filter 2 and 3 times, and with standard FBP without filtering, all with no iterations.*

The threshold method has the potential to create smooth images with reduced artifacts. On the other hand, it is time consuming when a correct RSP value (essential for treatment planning) is desired.

The Gaussian blur filter method showed interesting noise reduction levels and seems to be the most effective tested method to do so. It presented noticeable results after the FBP step, feeding the iterative reconstruction algorithm with better images. The presented results show that using the Gaussian blur filter twice combined with 5 image reconstruction iterations, could result in a suitable pCT image for treatment planning.

The post processing can be carried out as necessary, because, for the

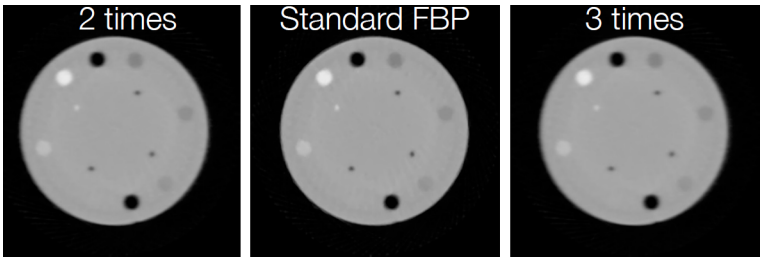

Figure 4.10: *Sensitom pCT images after applying the Gaussian filter 2 and 3 times, and with standard FBP without filtering, all after 5 iterations.*

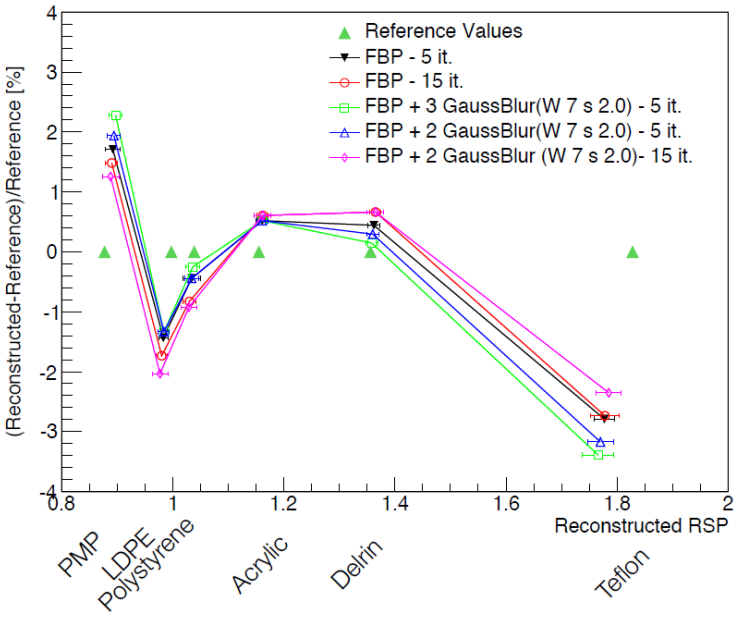

Material	RSP reference value
PMP	0.877
LDPE	0.9973
Polystyrene	1.0386
Acrylic	1.155
Delrin	1.356
Teflon	1.828

Figure 4.11: *Obtained RSP with different number of iterations, with and without the Gaussian filter, compared with reference values.*

moment, the treatment planning will not be executed in real time.

For fast patient positioning, the FBP pCT image with Gaussian blur filter could be used within few minutes for image registration.

Method	Number of Iterations	Average Discrepancy
FBP	5	1.22%
2 GB	5	1.32%
3 GB	5	1.28%
- (FBP)	15	1.34%
2 GB	15	1.31%

Table 4.2: *RSP % error for the Gaussian Bluer Filter method.*

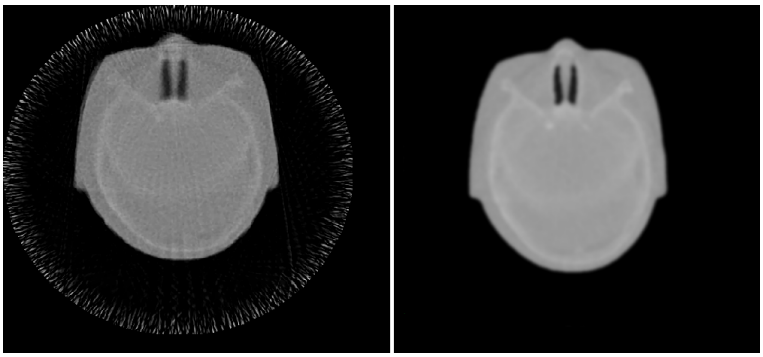

Figure 4.12: *Image reconstructed with the FBP method after 10 iterations (left) and after post-processing (right).*

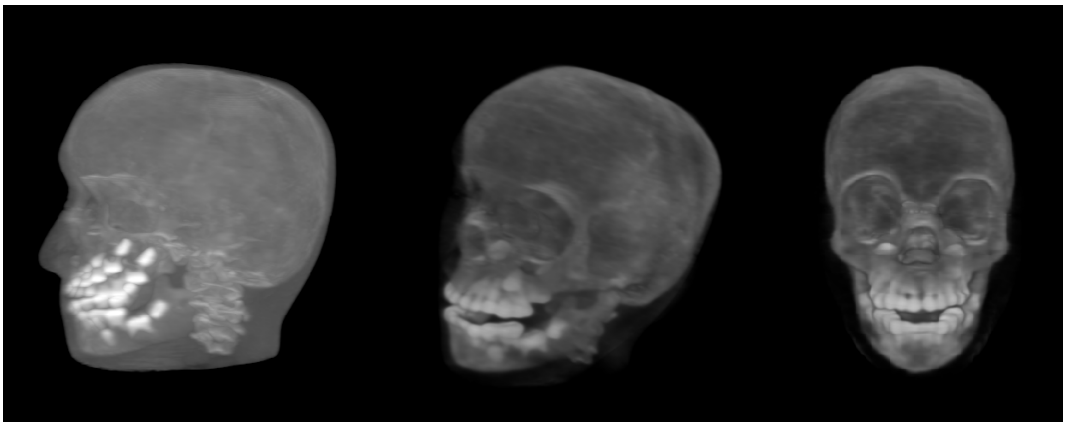

Figure 4.13: *3D pCT reconstructed and post-processed images for the pediatric head phantom.*

CHAPTER 5

Image registration algorithms for proton CT

This chapter evaluates the performance of 3D image registration algorithms, developed by the author, for realistic pediatric head phantom pCT images, analyzing results as a function of reconstruction quality and imaging dose. An experimental pCT scan of the phantom was modified by prescribing random 3D errors or deformation observed on a real H&N patient. The proton CT images were reconstructed with different number of protons to simulate low-dose imaging for patient setup. No other group have yet presented similar studies.

The development of image positioning techniques is important to minimize errors of particle therapy treatments, avoiding damage to healthy regions around the tumor and ensuring a sufficient dose deposition on the diseased region. In order to fully exploit the potential of particle therapy, submillimetric precision is required to avoid under or overshooting (figure 1.10), which could drastically affect clinical outcomes.

5.1 Rigid image registration algorithm

The accuracy of the developed rigid IR algorithm in recovering the applied rigid transformations was quantified as a function of imaging dose and image reconstruction quality.

5.1.1 Materials/Methods

5.1.1.1 Experimental Dataset

The pCT images used in this study were reconstructed as described previously on chapter 4.

To evaluate the 3D registration algorithm capability of successful patient positioning with low-dose images, pCT scans were reconstructed with a reduced number of protons. In this study we tested reconstructions done at 100%, 50%, 25% and 12.5% of the total dose of a standard pCT scan, where 100% corresponds to about 1.5 mGy. The high quality image, to be used for treatment planning, consists of an initial FBP plus iterations carried out to improve the reconstructed RSP values accuracy [PC15]. This planning pCT was registered with 10 cases (simulating setup errors) at each level of dose for the reconstruction. For registration purposes only (no need of accurate RSP values), FBP-only images were used in order to accelerate the process. In the following, these images will be referred to as FBP images associated with the percentage of dose used for its reconstruction, i.e. FBP_{100} stands for a pCT image reconstructed with full dose and FBP method without subsequent iterative refinements.

A visual comparison of the images used in this study can be seen in figure 5.1

5.1.1.2 Algorithm

A 3D registration algorithm was developed based on the Insight Segmentation and Registration Toolkit ITK library [YAL+02]. Mattes mutual information [MH01], commonly applied for multi-modality images was applied as the similarity metric. A regular-step gradient descent optimization method was used as the optimizer for the rigid image regis-

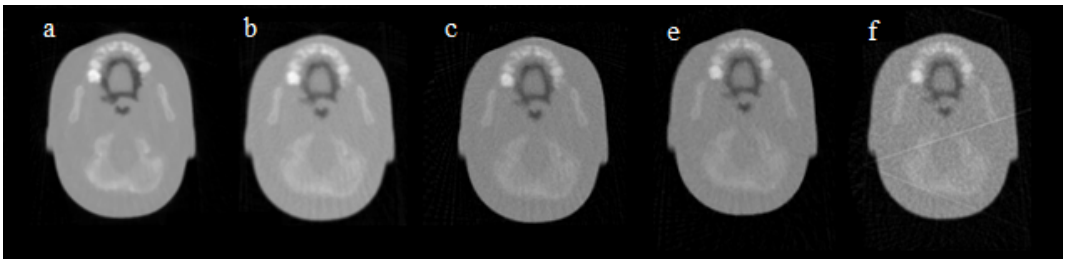

Figure 5.1: *Different image types used in this study: a) planning pCT, b) FBP_{100}, c) FBP_{50}, d) FBP_{25}, f) $FBP_{12.5}$.*

tration, in order to minimize the metric expression until the termination criterion set by the user, i.e., a minimum step length (0,001) or 200 iterations, was reached. The main features of the algorithm are summarized in table 5.1.

Component	Component Name	Notes
Optimizer	RegularStepGradientDescentOptimizer	Parameters are set based on time-precision trade-off
Metric	Mattes Mutual Information	
Transform	Euler 3D Transform	
Transform Initializer	Centered Transform Initializer	The computation of the center of mass decreases IR time significantly

Table 5.1: *Rigid registration algorithm's features.*

5.1.1.3 Performance Evaluation

To evaluate the rigid registration accuracy, 10 random 6-degree-of-freedom (DOF) transformations (translation and rotation) were created using orthogonal sampling [MBC79] and applied to each set of images to be registered. The images were then re-sampled using the Lanczos filter in the Amira 3D software platform (version 5.3.3, FEI Visualization Sciences Group). The transformations were within the clinically observed range of ± 3 mm for translations and ± 5 degrees for rotations. Ten different setup misalignments were thus simulated by using this procedure to all different levels of pCT image dose used in this study. Thus, we tested the rigid registration between the planning pCT and the FBP images reconstructed at 100%, 50%, 25% and 12.5% of the total dose of the standard

pCT scan.

After registering each pair of images, the residual distance between nominal and suggested corrections were measured to numerically confirm the visual registration assessment.

The registration procedures were carried out on a notebook with Intel Core i7-4710HQ 2.50GHz processor and 16.0 GB installed memory: the mean computational time was 2.5 minutes. By changing the stopping criteria or reducing the image size, the user can improve accuracy or reduce the computational time. The parameters can be changed; therefore, it is possible to decide how much similarity is enough to stop the IR process.

5.1.2 Results

After the registration procedure, the differences between imposed errors and suggested corrections were measured. The mean and standard deviation values of the residual distance calculated for the 10 different simulated shifts for each IR modality are summarized in table 5.2 for translation and in table 5.3 for rotations. Translations (T) are expressed in millimeters and rotations (R) in degrees for RL, AP and CC directions and axes, respectively. The residuals magnitudes found are similar, so they were grouped into anatomical directions and shown into box plots to illustrate their distribution on figures 5.2 and 5.3.

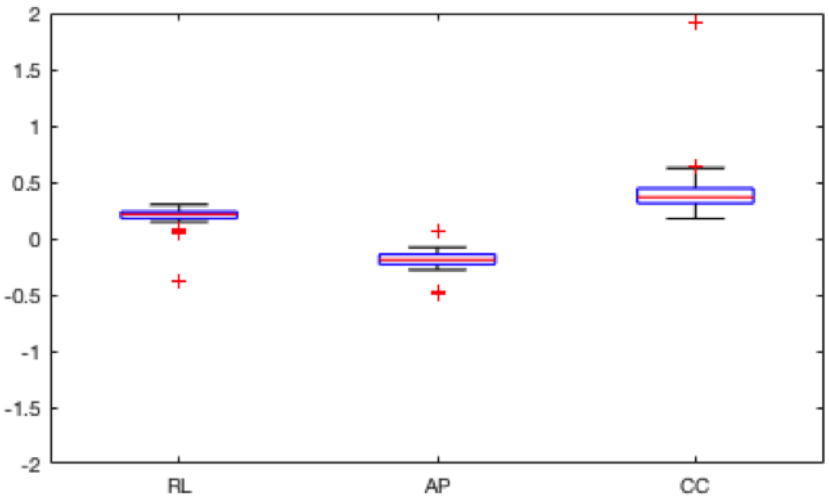

Figure 5.2: *Boxplot of translation residuals after IR.*

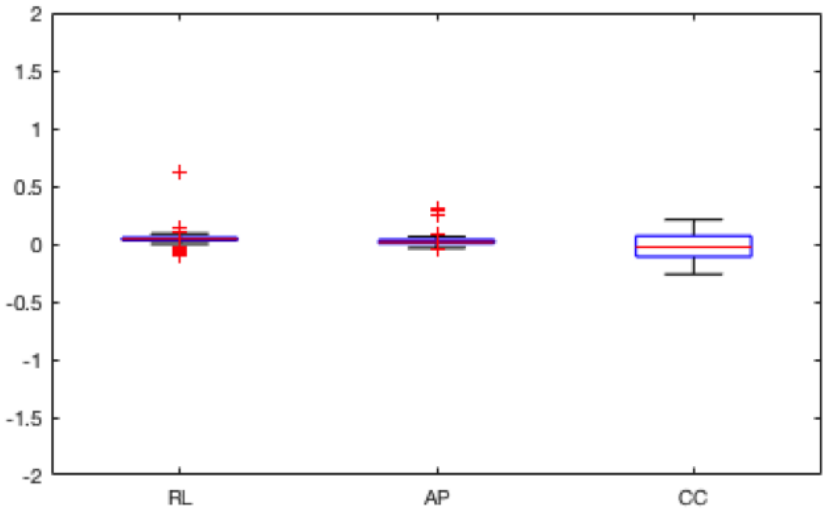

Figure 5.3: *Boxplot of rotation residuals after IR.*

Registration Modality	Tx (mm)	Ty (mm)	Tz (mm)
pCT - FBP_{100}	0.114 ± 0.185	-0.181 ± 0.135	0.507 ± 0.505
pCT - FBP_{50}	0.217 ± 0.063	-0.228 ± 0.093	0.367 ± 0.122
pCT - FBP_{25}	0.243 ± 0.037	-0.211 ± 0.052	0.347 ± 0.029
pCT - $FBP_{12.5}$	0.168 ± 0.078	-0.144 ± 0.068	0.438 ± 0.134

Table 5.2: *Residual translation errors after rigid registration.*

5.2 Deformable image registration algorithm

The present study evaluates the performance of a 3D registration algorithm in a realistic pediatric head phantom, analyzing results as a function of reconstruction quality and imaging dose. An experimental pCT scan of the phantom (figure 1) was modified by prescribing a deformation field for a real Head and Neck (H&N) case. The proton CT images were reconstructed with different number of protons to simulate low-dose imaging for patient setup. The accuracy of the IR algorithm

Registration Modality	Tx (mm)	Ty (mm)	Tz (mm)
pCT - FBP_{100}	0.084 ± 0.084	0.042 ± 0.099	-0.003 ± 0.129
pCT - FBP_{50}	0.041 ± 0.061	0.037 ± 0.096	-0.038 ± 0.128
pCT - FBP_{25}	0.024 ± 0.045	0.041 ± 0.087	-0.046 ± 0.126
pCT - $FBP_{12.5}$	0.038 ± 0.049	0.044 ± 0.083	-0.019 ± 0.133

Table 5.3: *Residual rotation errors after rigid registration.*

in recovering the applied deformable transformation was quantified as a function of imaging dose and image reconstruction quality.

5.2.1 Materials/Methods

5.2.1.1 Experimental Dataset

Ninety projections of a pediatric head phantom (model 715-HN, CIRS) were obtained with the phase II Proton CT Scanner (figure 5.4) built by the pCT Collaboration [SJM$^+$13] and reconstructed as described previously on section 6.1. These reconstructed text image files were converted then combined into a 3D DICOM image (fig. 4.13).

The registration accuracy was evaluated for the images produced as described in previous section for the rigid registration algorithm. The planning pCT was registered with 10 cases (simulating setup errors) at each level of dose used for the image reconstruction. The first registration assessment was for a similar quality image (FBP + 5 iterations): this specific case would provide dose recalculation directly in case of large discrepancies between fixed and moving image. Although the applied transforms to the pCT images were rigid, an algorithm capable of deformable registration was used to verify its performance with the lowest deformation cases (zero). This study was carried out envisioning a future implementation of an alike algorithm for all cases, thus providing correction for the smallest non-rigid changes on patient anatomy taking advantage of the low dose delivered from the pCT scan towards an optimal precision.

An X-ray CBCT-CT pair was used for the same cases to compare the results obtained with proton images to a well-established method for patient setup. The CBCT image was obtained with the On-Board ImagerÂ® (Varian) on the NovalisTX machine (BrainLab, Munich, Germany). The planning CT scan was obtained using Somatom Sensation Open scanner (Siemens, Forchheim, Germany), both at UCLA Department of Radiation Oncology and with the same voxel size as the pCT images. A visual comparison of the images used in this study can be seen in figure 5.5 .

A case of deformable image registration is also presented. A deforma-

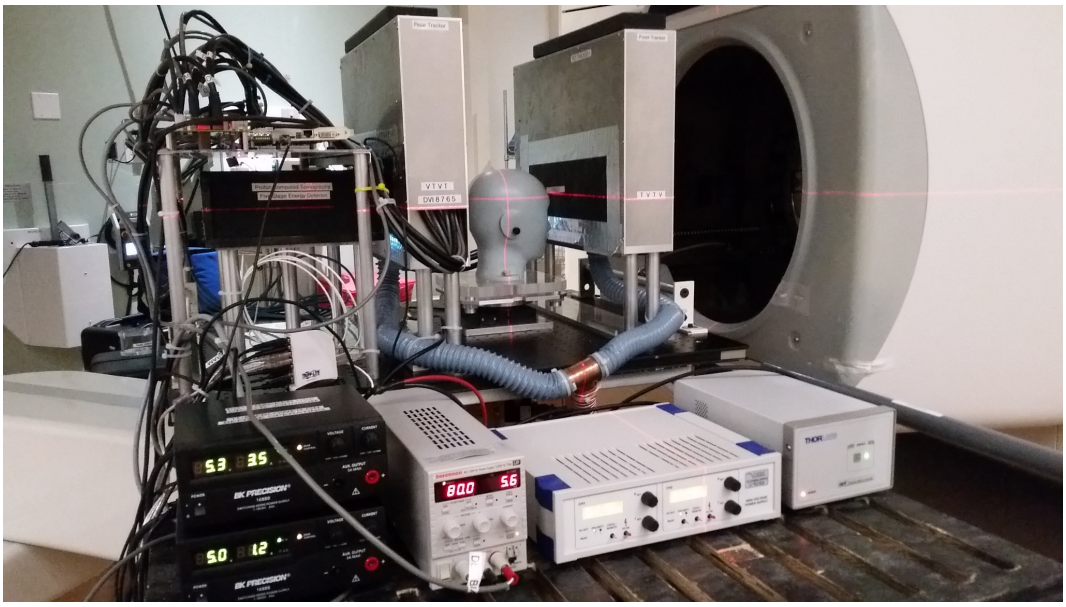

Figure 5.4: *Experimental setup for pCT image acquisition of a pediatric head phantom.*

tion field obtained from a real H&N patient was applied to all previously mentioned pCT images (example on figure 5.6), thus the algorithm was also tested for deformable image registration (DIR).

5.2.1.2 Algorithm

A 3D registration algorithm was developed based on the Insight Segmentation and Registration Toolkit ITK library [YAL+02]. Mattes mutual information [MH01] was used as the similarity metric. The limited-memory Broyden-Fletcher-Goldfarb-Shanno (L-BFGSBO) [BLNZ95] method was used as the optimizer for rigid and deformable image registration, in order to minimize the metric expression until termination criteria, e.g. the cost function convergence factor or gradient tolerance, are reached. The main components of the developed algorithm are presented in table 5.4.

Component	Component Name	Notes
Optimizer	LBFGS-B	Parameters are set based on time-precision trade-off
Metric	Mattes Mutual Information	
Interpolator	B-Spline	

Table 5.4: *Algorithm's features.*

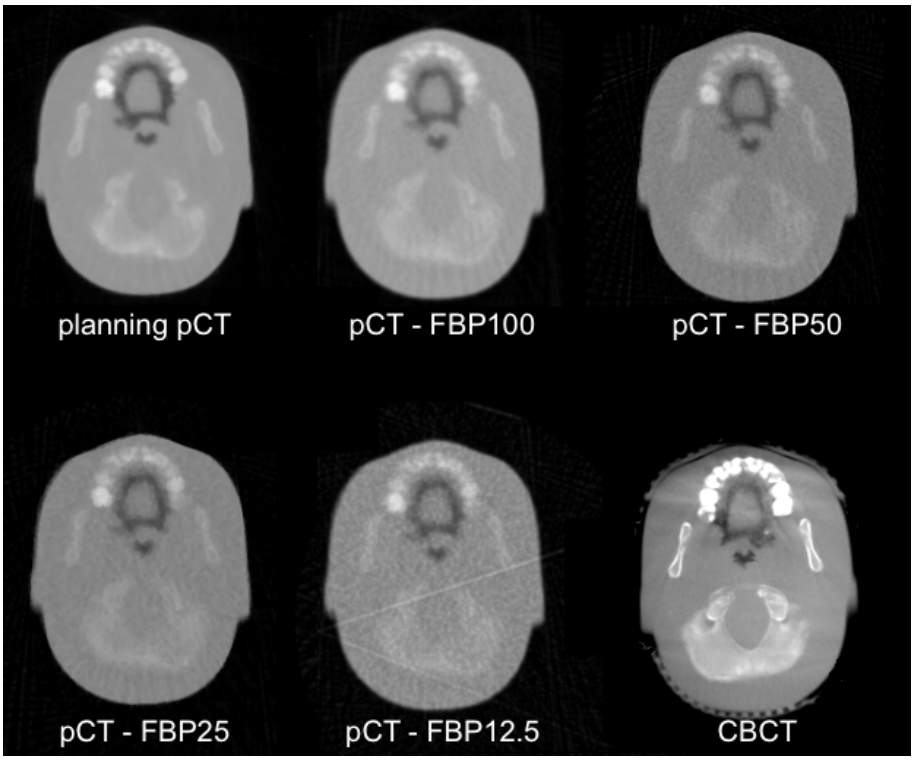

Figure 5.5: *Different images used in this study.*

5.2.2 Performance evaluation

To evaluate the deformable registration accuracy, a deformation field obtained from a real H&N patient was applied to all different levels of pCT images dose used in this study. Thus we tested the deformable registration between the planning pCT and a deformed version of itself and the FBP deformed images reconstructed at 100%, 50%, 25% and 12.5% of the total dose of the standard pCT scan. After registering each pair of images, the scale invariant feature transform (SIFT) [CH09] was used to extract features and to calculate the residual distance between corresponding histogram-based landmarks to numerically confirm the visual registration assessment (figure 5.7) [PPR$^+$13]. The registration procedures were carried out on a notebook with Intel Core i7-4710HQ 2.50GHz processor and 16.0 GB installed memory: the mean computational time was 6 minutes.

The user can improve accuracy or reduce the computational time by changing optimizer settings such as cost function convergence factor,

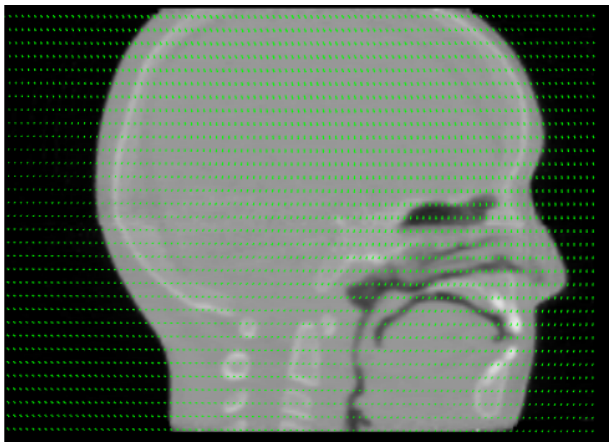

Figure 5.6: *Deformation Field applied to planning pCT.*

projected gradient tolerance, maximum number of evaluation and corrections, number of iterations, and number of grid nodes in one dimension. The convergence factor and gradient tolerance values were kept as those suggested by the ITK manual example. The number of evaluations was increased if further corrections were deemed necessary. A step to cache the B-Spline weights and indexes related to each sample used to compute the metric was implemented. This made the DIR faster while allocating more memory.

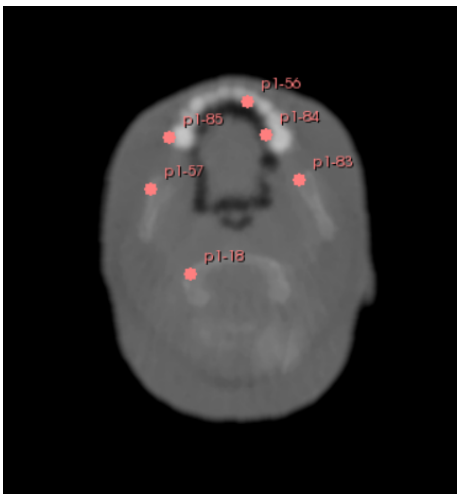

Figure 5.7: *Examples of landmarks used for distance calculation between fixed and transformed image.*

5.2.3 Results

5.2.3.1 Rigid alignment

After the registration procedure, on average, 35 corresponding markers between the fixed and the transformed image were identified using SIFT. The percentage of submillimetric errors calculated for each case are presented in table 5.5.

Registration Modality	Percentage of Submillimetric Errors
CT - CBCT	97.5
pCT - pCT	95.5
pCT - FBP_{100}	88.7
pCT - FBP_{50}	76.6
pCT - FBP_{25}	67.0
pCT - $FBP_{12.5}$	66.1

Table 5.5: *Submillimetric error distribution after rigid alignment.*

5.2.3.2 Deformable registration

After the deformable registration procedure (figure 5.8), on average, 44 corresponding markers between the fixed and the transformed image were identified using SIFT for pCT images. The percentage of submillimetric errors calculated calculated for each case after DIR are presented in table 5.6.

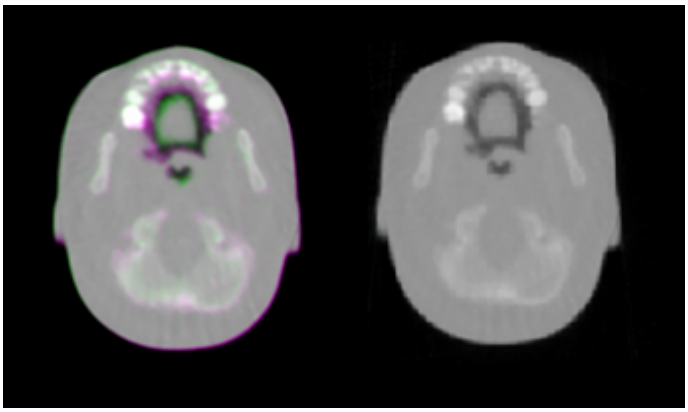

Figure 5.8: *Left: Deformed pCT image overlaid with the original image. Right: Same images following DIR.*

Registration Modality	Percentage of Submillimetric Errors
pCT - pCT	100
pCT - FBP_{100}	63.5
pCT - FBP_{50}	71.4
pCT - FBP_{25}	64.4
pCT - $FBP_{12.5}$	64.1

Table 5.6: *Submillimetric error distribution after deformable image registration.*

5.3 Proton CT image registration discussion

Two IR algorithms utilizing the ITK open software package were developed and tested for registration of experimental planning pCT images of a pediatric head phantom. The experimental dataset used in this study came from transformed images generated from a single pCT acquisition; the different number of protons used for image reconstruction eliminates false positive results due to noise and artifacts redundancy, which might facilitate the automatic IR process. Errors associated with these image processing procedures are expected well within the sub-millimeter scale, which should not bias the clinical interpretation of reported results. The actual performance of IR algorithm in the use of pCT for patient setup could be confirmed through experimental measurements where images are acquired after changing the position of the phantom with the 6-DOF patient positioner. Nevertheless, the implemented study provided the quantification of expected performance in a controlled scenario, where the amount of rigid mismatch is known and the results are believed to be representative of the clinical situation with random variations in the position of a patient. The image registration procedure was carried out automatically, following the selection of the two images in DICOM format, in order to test the performance of the implemented IR method in recovering misalignments in a clinically realistic range.

Our algorithm's results show efficient image registration with submillimetric residual errors as shown before for real patient data [CCF+16]. IR between CT-CBCT is a well-accepted and reliable method. Compared to this standard, the planning pCT IR presents at least equivalent results, since the percentage of submillimetric errors is similar. It has also to be

considered that for pCT images, the number of landmarks found with SIFT is twice the number of those found for the X-ray method due to images similarity. Moreover, low-dose FBP-only images, used for IR with the planning pCT, present larger SIFT-detected errors even if visually the images seem almost perfectly aligned. These errors are mostly due to image noise and the lower quality of images which would interfere in automatic feature detection, presenting around 44% of the errors between 1 and 2 mm (same magnitude of pixel size in craniocaudal direction).

An advantage of the pCT is the absence of image artifacts, as those due to metal implants, which contributes to much more precise dose estimation in patient tissues. The uncertainties derived from the conversion from CT numbers to RSP values are also eliminated.

Our algorithm presented good results for rigid and deformable image registration, since residual errors were more likely to be found with sub-millimeter magnitude. Usually, rigid transforms are easy to detect and correct, nevertheless the DIR results present similar error distribution. Moreover, $FBP_{12.5}$ images, used for IR with the planning pCT, still present low residual errors even if visually the images present reduced quality.

Proton CT has the potential to be a useful tool for patient setup in proton therapy. Due to the constant developments in image reconstruction, which would meet clinical promptness requirements and precise FBP values, planning pCT (FBP + 5 iterations) could be acquired on daily basis for dose recalculation, aiming ultimate treatment delivery effectiveness. For less sophisticated and faster plan adjustments, pCT_{FBP} images could be used for plan adaptation with DIR.

Compared to an estimated standard CBCT head dose of 10 mGy; a dose of about 1.45 mGy for the full planning pCT dose and best possible registration image led to superior registration results. Even for a histories reduction to 12.5% ($\tilde{0}$.18 mGy), corresponding to about 55-times dose reduction, the majority of residual errors were still found to have submillimeter magnitude. Proton CT images could be acquired on a daily basis for registration and dose recalculation, making pCT a very attractive modality for image-guidance.

CHAPTER 6

Conclusions and future prospects

This PhD thesis presented a detailed analysis of some currently used methods for image-guidance and adaptive radio and proton therapy. Tests were carried out and hypothesis for new methods were elaborated. The motivation and rationale for proton therapy was presented and basic proton interactions with matter described. These interactions present different sources of uncertainties, which require diverse mitigation strategies when compared to conventional radiotherapy. Image registration procedures are fundamental for photon and proton treatment success. The gains with technological developments in this area are noteworthy; more precision during patient setup allows expectation for better results and PTV margin reduction which, in turn, will spare patient healthy tissues.

Daily image-guidance strategies, for the methods evaluated in this dissertation, show:

- The presented method relying on stereoscopic X-rays (with the ExacTrac system) reduced the setup errors derived from skin-markers alignment with in-room laser. A reduced number of fractions is convenient for patients with reduced mobility and other health com-

plications, and is made possible, due to enhanced patient positioning and target localization techniques offered by image-guidance.

- Low residual errors for CT-CBCT rigid IR, assuming negligible deformation can be observed.
- Optical tracking system for proton therapy H&N patients at CNAO contributed to patient positioning, due to automatic rotation corrections before IR.
- DIR could be implemented for limited FoV CBCT to update the anatomical region of interest on the planning CT and give an estimation of the actual anatomy of the patient for conventional radiotherapy plan evaluation.
- Volumetric images, as well as for rigid alignment, could be used for deformable image registration and for internal organ motion or structural change verification. In prostate patients where large field-of-view CBCT is used, DIR allows evaluating anatomical changes and potential counter-measures. Registration between CBCT and planning CT images based on prostate position can be applied to assure prescribed dose deposition with IMRT or similar photon technique. The proposed virtual CT act as a surrogate of the re-planning CT, being demonstrated useful for treatment dose recalculation.
- Implementation of adaptive therapy measures by the developed DIR methods, such as contour propagation for online DVH analysis and decisions over treatment re-planning. The propagated generated contours give the possibility of online dose evaluation on CT-on-rail, therefore the treatment plan's adequacy can be verified daily and adjustments done faster, if necessary;
- Imaging processing methods for pCT are capable of spatial resolution and RSP values improvement, demonstrating a promising potential for systematic use in proton therapy;
- Accurate low-dose pCT rigid and deformable image registration for pretreatment verification, allowing accurate setup at minimal imaging dose in proton therapy.

The introduction of the adaptive therapy concept clinically is not trivial. It requires more time per patient and a detailed study of the best way for its implementation, evaluating the effort-benefit trade-off. New methods should be exhaustively tested to keep us from a 'black box' scenario, where the uncertainties might be significant and compromise the treatment. Studies of clinical routine practices are expected to ensure the adequacy of currently used methods or even suggest better decisions to take clinically. The presented virtual CT, derived from DIR, exhibit updated patient anatomy and is expected to serve as a quality surrogate for the re-planning CT.

The use of the Quantitative Analysis of Normal Tissue Effects in the Clinic (QUANTEC) table as a normal tissue dose/volume tolerance reference is a common and useful practice in radiotherapy. It presents limitations and should be used in a conscientious manner. When estimating the risks, some models take into account DVHs which ignore organs? spatial information that might have different functional importance and present different response to radiation. The studies evaluated to assemble these recommendations thresholds, are usually limited to a single planning CT, ignoring patient anatomic changes during treatment [MYJ+10]. DIR gives the possibility of tracking the dose distribution along the treatment by retrospectively recalculating the daily fraction dose, on a virtual or re-planning CT, and deforming it to the original planning CT. By doing this, we would have a much more realistic scenario to correlate local acute tissue reactions with received radiation. A large number of observations would serve as strong evidences to QUANTEC update or notes addition necessity.

An alternative method for proton therapy imaging, still in development, was tested for patient positioning. Pre and post processing techniques for proton CT (pCT) were compared and algorithms for IR developed envisioning pCT future applicability inside clinical context. Even with a dose reduction of up to 55 times, compared to a standard H&N CBCT, pCT images were still useful for 3D IR. Encouraging results were found and further developments are expected, aiming at useful volumetric images with low dose given to the imaged patient. Quality pCT images are envisioned to allow diagnostic, treatment planning, patient setup

and adaptive proton therapy measures.

Several future developments can be envisioned as a continuation of this work, combining recent research efforts toward the further development of adaptive image guidance methods.

6.1 Open-source adaptive IMPT for research

Open source codes have been contributing for the scientific development of proton therapy. Communities of researchers are committed to the constant improvement and working to create and expand interesting tools for research, such as ITK and PLASTIMATCH, mentioned before in this dissertation.

Maxime Desplanques described in his thesis an open source software for treatment planning [Des15]. By combining DIR and proton dose calculation, it is possible to update the stopping power maps after correcting setup errors actually observed in-room prior to the treatment.

An initial attempt to combine our works and make a platform for adaptive IMPT research can be seen in figure 6.1. After selecting the CBCT and CT images, the software prototype works as follows:

- The 'Register' button will perform a DIR with one of the developed codes presented in this dissertation;
- After assessing the DIR quality (SIFT might be integrated as well), the user can press the 'Adapt DICOM' button to propagate the contours by calling PLASTIMATCH function WARP and create a new DICOM with contours representing an updated CT of the patient;
- The button 'Range Verification' will trigger the pre-treatment proton beam range verification, using a fast ray tracer (RT) algorithm (described in [Des15]) as a "scout beam" on images derived from DIR (example on image 6.2);
- After verifying the proton beam range on the updated anatomy, if necessary, a new plan can be calculated with the button 'Adapt Plan'. Among the available algorithms used for dose calculation, the HGS (Hong Geometry dose Summation), the same used for XiO (ELEKTA) has been included.

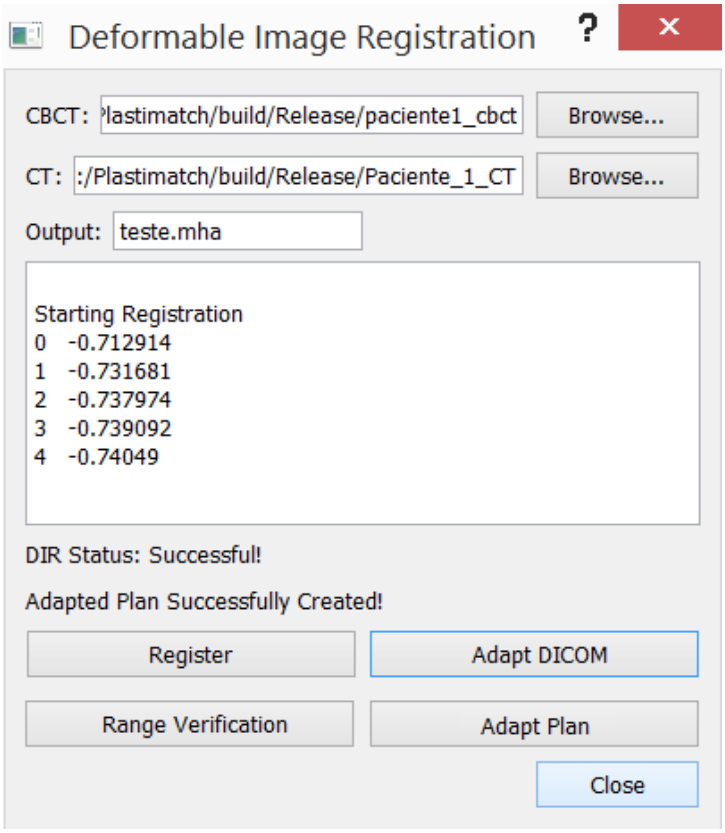

Figure 6.1: *Early GUI for open-source adaptive IMPT research.*

This open source module, once available, will enable dosimetric verification of delivered proton therapy at a research level, overcoming commercial treatment planning systems elevated costs and facilitating DIR implementation and verification .

6.2 Proton therapy imaging future prospects

The major promise of image guidance with cone beam CT in the proton treatment room is its potential for reducing the margins of high-dose planning target volumes (PTVs), which would lead to a reduction in complication rates and/or would allow higher doses to the tumour. Imaging capability using x-ray technology was at first 2D (planar radiographs), but quickly became 3D (volumetric CT) with the installation of cone beam CT scanners in proton treatment rooms. There is, however, a fundamental problem with the use of x-ray imaging for treatment planning and pre-treatment verification in proton therapy resulting in rela-

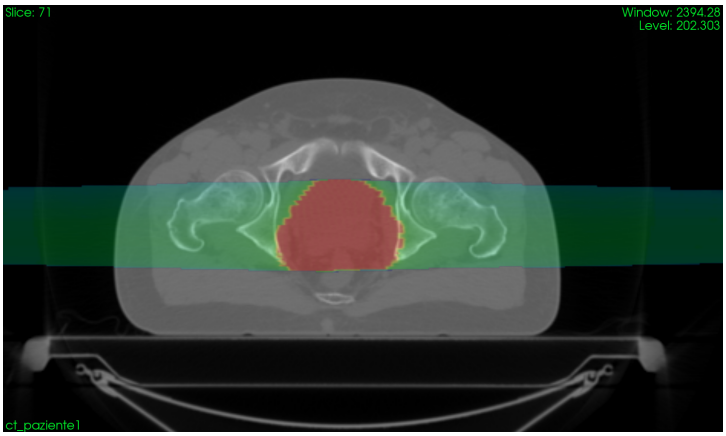

Figure 6.2: *Ray-tracing for prostate patient.*

tively large range uncertainties. This is due to the fact that the range information it provides in the form of a map of relative stopping power (RSP) of tissues with respect to water is inaccurate due to the differences in the dependence of x-ray attenuation and proton energy loss on tissue composition (electron density and atomic number). This yields an inherently inaccurate conversion of x-ray Hounsfield units to RSP. X-ray radiographs do not provide any information on the integrated RSP that could provide a range check of proton beams before treatment. There are additional sources of inaccuracy with x-ray CT imaging, including beam hardening and artifacts in the presence of compact bone and metal implants, the latter leading to particularly large range uncertainties when the x-ray CT scan is used for treatment planning. The quest for a better method of determining the stopping power has been an important area of research and development [KL13].

Recent solutions that have been proposed include the use of dual-energy CT (DECT) for proton treatment planning [BLR$^+$17], which allows a more accurate definition of RSP, but does not solve the problem of image artifacts nor provide an immediate check of range accuracy before treatment with the patient in treatment position. Other approaches to reducing range uncertainties in proton therapy are at various stages of development and include prompt gamma imaging [BLR$^+$17], ionoacoustic imaging [BLR$^+$17] during treatment, and positron emission tomography (PET) detecting proton-beam-induced positron emitters post-

treatment [CBS+16]. These approaches are not fully satisfactory for the following reasons reasons:

- They do not detect range inaccuracies before treatment but only during or after treatment. Thus, while range inaccuracies may be detected, they would need to be corrected after treatment. This may be problematic if the treatment is delivered as a few dose fractions or as a single fraction.

- These techniques do not mitigate the inaccuracy of proton treatment planning inherent in using x-ray CT, including the presence of CT artifacts.

Proton pencil beam scanning and intensity-modulated proton treatment (IMPT) plans are now commonly used for the treatment of head and neck cancer, including squamous cell carcinomas of the nasal cavity, the oral cavity, and paranasal sinuses. In children the head and neck is a common site for rhabdomyosarcomas. In IMPT, two or three proton beams are combined during each treatment that deliver individual dose distributions adding up to highly conformal dose to the target volume and respecting the tolerance doses of organs at risk (eyes, cranial nerves, parotid glands etc.) The steep distal dose gradient of proton beams is particularly helpful in protecting these organs at risk but the location of these gradients is subject to significant uncertainties due to changes in tissue and tumor anatomy over time between treatments and even during treatments [CBS+16]. Reduction of range uncertainties offers a great clinical advantage in these patients.

Proton imaging has progressed in recent years and the initial clinical focus is on head and neck cancer and brain tumors because the available proton energy in all clinical centers (230-250 MeV) is sufficient to image the involved anatomical regions that need to be included in the treatment planning scan. Proton imaging promises, in fact, a complete solution of the range inaccuracies in proton therapy. Proton CT (pCT) would substantially reduce the uncertainties of treatment planning by directly measuring RSP (the tissue property determining proton energy loss) without artifacts from metallic implants and much lower dose to the patient than

with comparable x-ray images. Proton radiography (pRad) would provide the capability to verify the range of individual proton beams before treatment. Therefore, proton imaging with pCT and pRad will enable clinicians to fully exploit the advantages of proton radiotherapy. Section 6.2.1 introduces the use of pRad for patient positioning. For a detailed review of the early approaches of imaging with protons the reader is referred to the recent comprehensive review article on this subject by Poludniowski et al. [PAE15].

The most advanced, and closest to clinical approach is the proton CT scanner (also able to do pRad) of the U.S.-based pCT collaborations [SBL$^+$04b, SPTS08, PSCR10, JBD$^+$16, Wil04, GGBC$^+$17], which was utilized in this research. The collaboration is now planning to advance this concept to the clinical phase with the design of a commercially available pCT and pRad system that will be tested in two pilot studies on 20 patients with head and neck cancer (R. Schulte, personal communication). Rather than mounting the imaging system on a rotating gantry the detectors will be positioned on a horizontal scanning beam line and the patient will rotate with a vertical-axis chair during exposure to a low-intensity, actively scanned proton pencil beam. These studies should demonstrate 1) the feasibility of integrating pCT (for planning) and pRad for pre-treatment verification and 2) the safety and efficiency of pCT and pRad imaging to treatment patient with reduced PTV margins taking into account the reduced range uncertainty.

Future expansion of proton imaging will involve mounting the detector on a gantry, which would allow imaging patients in the horizontal position. Current control systems would not allow beam delivery while the proton gantry is rotating. Therefore, this step would require a change in the control system. Imaging for other tumor sites (chest, abdomen, pelvis) would require proton energies higher than 250 MeV. There is already one proton vendor (ProTom International) providing a proton synchrotron with up to 330 MeV.

6.2.1 Proton radiography for patient positioning

Proton radiography can be acquired with the treatment gantry. The detectors described previously for the pCT scanner can be used for obtaining proton 2D projections to be used on a 2D-3D registration. An analogous procedure to the current largely use of registering DRRs from the planning CT to two orthogonal in-room X-ray projections. An example of proton DRR and projections are shown in figures 6.3 and 6.4 respectively.

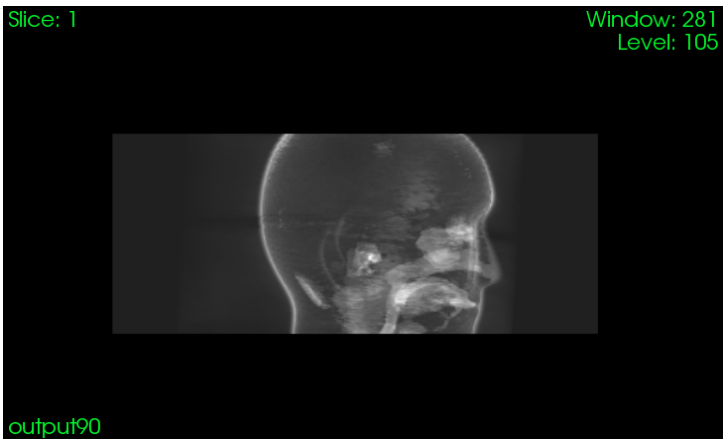

Figure 6.3: *Proton CT DRR.*

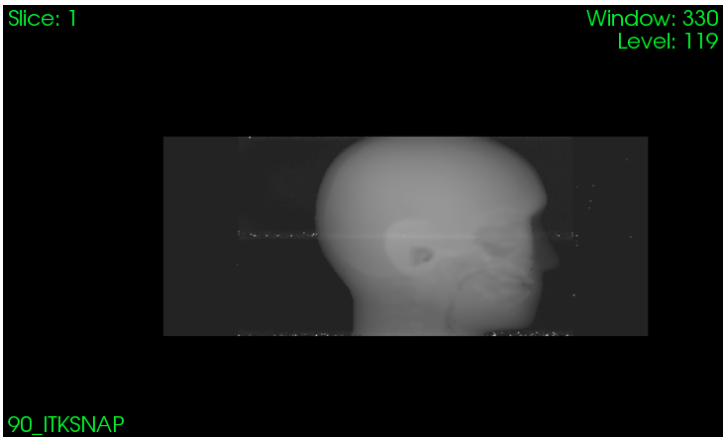

Figure 6.4: *Proton radiography.*

Further developments in proton imaging techniques will make this method of positioning available as a low-dose and efficient alternative for image guided proton therapy.

6.2.2 Proton CT for proton therapy treatment planning

The main goal in developing a proton CT scanner is probably to have a high quality volumetric image of the patient, with correct RSP values, to serve for diagnostic and proton treatment planning.

A few tests of proton therapy planning using pCT were made with the open source code described previously in this chapter. The same plan was applied to a conventional CT and for a pCT scan (figure 6.5). Their dose comparison showed difference on the borders (figure **??**), probably due to the noisy pCT images (acquired in 2015). Newer images present much clearer appearance, with reduced artifacts and more reliable RSP values, thanks to the efforts of the pCT Group. Therefore, dose estimation is expected to improve according to calibrations and reconstruction methods refinements.

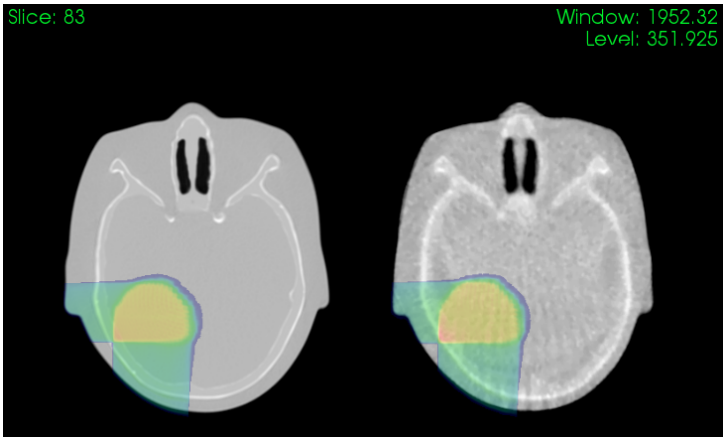

Figure 6.5: *Open source proton therapy planning for CT and pCT.*

Future steps will include the adaptation of the open source code to work with pCT RSP values images. Also the feasibility of using the current TPS (examples on figures 6.8 and 6.7) by inserting adequate calibration curves needs to be verified.

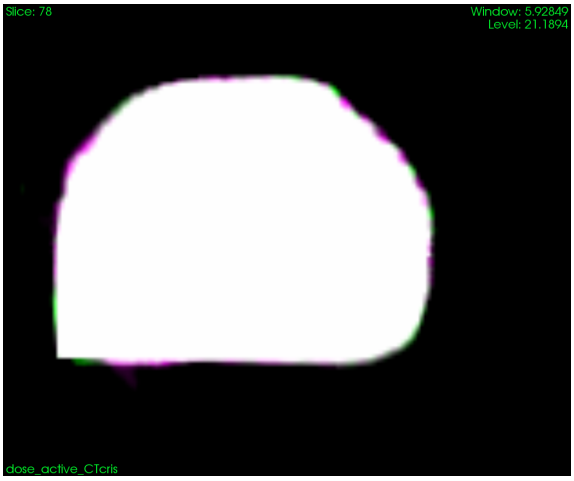

Figure 6.6: *Dose comparison on PTV for plans shown on figure 6.5. White means same intensity and the colored on borders means different dose.*

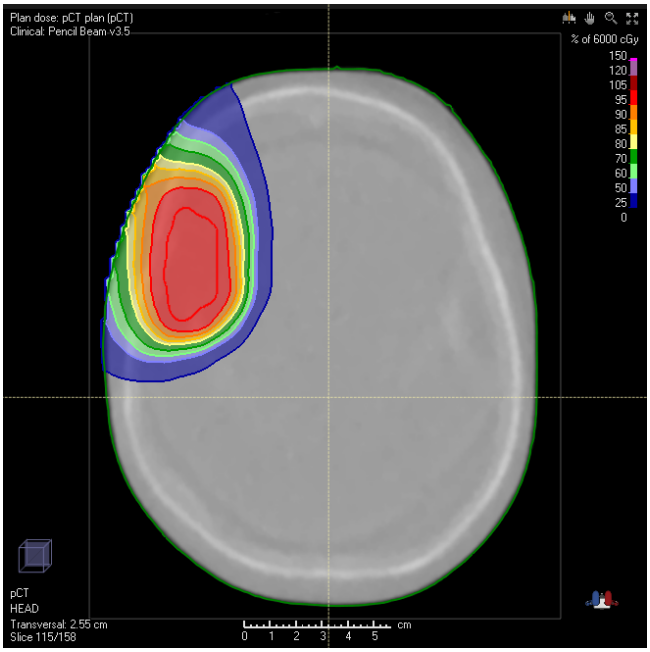

Figure 6.7: *Treatment plan simulation on a pCT image inside RAYSTATION TPS.*

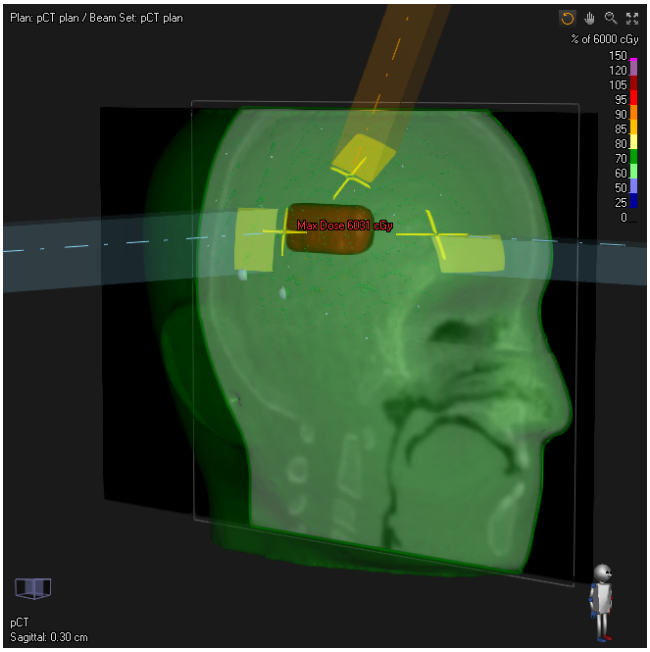

Figure 6.8: *Treatment plan simulation on a pCT image inside RAYSTATION TPS.*

Bibliography

[AAA+03] S. AGOSTINELLIi, J. Allison, K. Amako, J. Apostolakis, H. Araujo, P. Arce, M. Asai, D. Axen, S. Banerjee, G. Barrand, F. Behner, L. Bellagamba, J. Boudreau, L. Broglia, a. Brunengo, H. Burkhardt, S. Chauvie, J. Chuma, R. Chytracek, G. Cooperman, G. Cosmo, P. Degtyarenko, a. Dell'Acqua, G. Depaola, D. Dietrich, R. Enami, a. Feliciello, C. Ferguson, H. Fesefeldt, G. Folger, F. Foppiano, a. Forti, S. Garelli, S. Giani, R. Giannitrapani, D. Gibin, J.J. Gómez Cadenas, I. González, G. Gracia Abril, G. Greeniaus, W. Greiner, V. Grichine, a. Grossheim, S. Guatelli, P. Gumplinger, R. Hamatsu, K. Hashimoto, H. Hasui, a. Heikkinen, a. Howard, V. Ivanchenko, a. Johnson, F.W. Jones, J. Kallenbach, N. Kanaya, M. Kawabata, Y. Kawabata, M. Kawaguti, S. Kelner, P. Kent, a. Kimura, T. Kodama, R. Kokoulin, M. Kossov, H. Kurashige, E. Lamanna, T. Lampén, V. Lara, V. Lefebure, F. Lei, M. Liendl, W. Lockman, F. Longo, S. Magni, M. Maire, E. Medernach, K. Minamimoto, P. Mora de Freitas, Y. Morita, K. Murakami, M. Nagamatu, R. Nartallo, P. Nieminen, T. Nishimura, K. Ohtsubo, M. Okamura, S. O'Neale, Y. Oohata, K. Paech, J. Perl, a. Pfeiffer, M.G. Pia, F. Ranjard, a. Rybin, S. Sadilov, E. Di Salvo, G. Santin, T. Sasaki, N. Savvas, Y. Sawada, S. Scherer, S. Sei, V. Sirotenko, D. Smith, N. Starkov, H. Stoecker, J. Sulkimo, M. Takahata, S. Tanaka, E. Tcherniaev, E. Safai Tehrani, M. Tropeano, P. Truscott, H. Uno, L. Urban, P. Urban, M. Verderi, a. Walkden, W. Wander, H. Weber, J.P. Wellisch, T. Wenaus, D.C. Williams, D. Wright, T. Yamada, H. Yoshida, and D. Zschiesche. Geant4 a simulation toolkit. *Nuclear Instruments and Methods in Physics Research Section A: Accelerators, Spectrometers, Detectors and Associated Equipment*, 506(3):250–303, July 2003. URL: `http://linkinghub.elsevier.com/retrieve/pii/S0168900203013688`, `doi:10.1016/S0168-9002(03)01368-8`.

[ALM08] Luciana Correia Alves, Iúri Da Costa Leite, and Carla Jorge Machado. Health profile of the elderly in Brazil: analysis of the 2003 National Household Sample

Survey using the Grade of Membership method. *Cadernos de Saúde Pública*, 24(3):535–546, 2008. doi:10.1590/S0102-311X2008000300007.

[Alp90] Edward L. Alpen. *Radiation Biophysics*. Academic Press, 1990. doi:10.1016/0020-708X(62)90125-4.

[APA12] Marta Adamczyk, Tomasz Piotrowski, and Ewa Adamiak. Evaluation of combining bony anatomy and soft tissue position correction strategies for IMRT prostate cancer patients. *Reports of Practical Oncology and Radiotherapy*, 17(2):104–109, 2012. URL: http://dx.doi.org/10.1016/j.rpor.2012.01.005, doi:10.1016/j.rpor.2012.01.005.

[AYF+13] Yuichi Akino, Yasuo Yoshioka, Shoichi Fukuda, Shintaroh Maruoka, Yutaka Takahashi, Masashi Yagi, Hirokazu Mizuno, Fumiaki Isohashi, and Kazuhiko Ogawa. Estimation of rectal dose using daily megavoltage cone-beam computed tomography and deformable image registration. *International Journal of Radiation Oncology Biology Physics*, 87(3), 2013. doi:10.1016/j.ijrobp.2013.06.2054.

[BC04] E. BLAKELY and P. Chang. Late effects from hadron therapy. *Radiotherapy and Oncology*, 2004.

[BCC+14] T.T. Böhlen, F. Cerutti, M.P.W. Chin, A. Fassò, A. Ferrari, P.G. Ortega, A. Mairani, P.R. Sala, G. Smirnov, and V. Vlachoudis. The FLUKA Code: Developments and Challenges for High Energy and Medical Applications. *Nuclear Data Sheets*, 120:211–214, jun 2014. URL: http://linkinghub.elsevier.com/retrieve/pii/S0090375214005018, doi:10.1016/j.nds.2014.07.049.

[BET30] H. BETHE. Zur Theorie des Durchgangs schneller Korpuskularstrahlen durch Materie. *Annalen der Physik*, 397:325–400, 1930. doi:10.1002/andp.19303970303.

[BLNZ95] Richard H. Byrd, Peihuang Lu, Jorge Nocedal, and Ciyou Zhu. A Limited Memory Algorithm for Bound Constrained Optimization. *SIAM Journal on Scientific Computing*, 16(5):1190–1208, 1995. doi:10.1137/0916069.

[BLR+17] Esther Bär, Arthur Lalonde, Gary Royle, Hsiao Ming Lu, and Hugo Bouchard. The potential of dual-energy CT to reduce proton beam range uncertainties. *Medical Physics*, 44(6):2332–2344, jun 2017. URL: http://www.ncbi.nlm.nih.gov/pubmed/28295434http://doi.wiley.com/10.1002/mp.12215, doi:10.1002/mp.12215.

[Buc15] Jeffrey C Buchsbaum. Pediatric proton therapy in 2015: Indications, applications and considerations. *APPLIED RADIATION ONCOLOGY*, (September), 2015.

[BYWW+12] I BUZUROVIC, Y Yu, M Werner-Wasik, T Biswas, P R Anne, a P Dicker, and T K Podder. Implementation and experimental results of 4D tumor tracking using robotic couch. *Medical physics*, 39(11):6957–67, November

2012. URL: http://www.ncbi.nlm.nih.gov/pubmed/23127089, doi:10.1118/1.4758064.

[CBH+13] G. Coutrakon, V. Bashkirov, F. Hurley, R Johnson, V Rykalin, H. Sadrozinski, and Reinhard W Schulte. Design and construction of the first proton CT scanner, 2013.

[CBS+16] P Cambraia Lopes, J Bauer, A Salomon, I Rinaldi, V Tabacchini, T Tessonnier, P Crespo, K Parodi, and D R Schaart. First in situ TOF-PET study using digital photon counters for proton range verification. *Physics in Medicine and Biology*, 61(16):6203–6230, aug 2016. URL: http://stacks.iop.org/0031-9155/61/i=16/a=6203?key=crossref.2663089321a89962d8c854fac2ae47ed, doi:10.1088/0031-9155/61/16/6203.

[CCF+16] Francisco Roberto Cassetta Jr., Delia Ciardo, Giovanni Fattori, Marco Riboldi, Roberto Orecchia, Barbara Jereczek-Fossa, and Guido Baroni. Virtual CT for adaptive prostate radiotherapy based on CT-CBCT deformable image registration. In *ESTRO 35 Proceedings*, 2016.

[CH09] Warren Cheung and Ghassan Hamarneh. n-SIFT: n-Dimensional scale invariant feature transform. *IEEE Transactions on Image Processing*, 18(9):2012–2021, 2009. doi:10.1109/TIP.2009.2024578.

[CJCOA11] C. CANDELA Juan, M. Crispin-Ortuzar, and M. Aslaninejad. Depth-dose distribution of proton beams using inelastic-collision cross sections of liquid water. *Nuclear Instruments and Methods in Physics Research Section B: Beam Interactions with Materials and Atoms*, 269(2):189–196, January 2011. URL: http://linkinghub.elsevier.com/retrieve/pii/S0168583X10007962, doi:10.1016/j.nimb.2010.10.013.

[Cle12] Elizabeth Clements. A new kind of detector technology that could lead to discoveries in particle physics may also lead to better 3D images of the human body and help cancer patients. *Http://Www.Symmetrymagazine.Org/Cms/?Pid=1000942*, page Accessed: June 1, 2012.

[CSZ+09] George CIANGARU, Narayan Sahoo, X Ronald Zhu, Gabriel O Sawakuchi, and Michael T Gillin. Computation of doses for large-angle coulomb scattering of proton pencil beams. *Physics in medicine and biology*, 54(24):7285–300, December 2009. URL: http://www.ncbi.nlm.nih.gov/pubmed/19926912, doi:10.1088/0031-9155/54/24/003.

[CYM+14] Andrew L. Chang, Toruun I. Yock, Anita Mahajan, Christine Hill-Kaiser, Sameer Keole, Lilia Loredo, Oren Cahlon, Kevin P. McMullen, William Hartsell, and Daniel J. Indelicato. Pediatric Proton Therapy: Patterns of Care across the United States. *International Journal of Particle Therapy*, 1(2):XX–XX, 2014. URL: http://theijpt.org/doi/abs/10.14338/IJPT.13.00009.1, doi:10.14338/IJPT.13.00009.1.

Bibliography

[DEA94] JOE DEASY. Icru report 49, stopping powers and ranges for protons and alph particles. *Medical Physics*, 21:709–710, 1994. doi:10.1118/1.597176.

[Des15] Maxime Desplanques. *AN OPEN SOURCE SOFTWARE FOR PROTON TREATMENT PLANNING*. PhD thesis, Politecnico di Milano, 2015.

[DFIF14] Yusuke Demizu, Osamu Fujii, Hiromitsu Iwata, and Nobukazu Fuwa. Carbon Ion Therapy for Early-Stage Non-Small-Cell Lung Cancer. *Biomed Research International*, 2014(727962):9, 2014.

[DPS+11] V.V. DENYAK, S.a. Paschuk, H.R. Schelin, R.L. Rocha, J.a.P. Setti, M.C.L. Klock, I.G. Evseev, and O.I. Yevseyeva. Dose energy dependence in proton imaging. *Nuclear Instruments and Methods in Physics Research Section A: Accelerators, Spectrometers, Detectors and Associated Equipment*, 652(1):747–750, October 2011. URL: http://linkinghub.elsevier.com/retrieve/pii/S0168900210021418, doi:10.1016/j.nima.2010.09.108.

[DTF+13] Maxime Desplanques, Barbara Tagaste, Giulia Fontana, Andrea Pella, Marco Riboldi, Giovanni Fattori, Andrea Donno, Guido Baroni, and Roberto Orecchia. A comparative study between the imaging system and the optical tracking system in proton therapy at CNAO. *Journal of Radiation Research*, 54, 2013. doi:10.1093/jrr/rrt043.

[Fat13] Giovanni Fattori. *Image-guided management of uncertainties in scanned particle therapy*. PhD thesis, Politecnico di Milano, 2013.

[FHS+13] Samah Ferjani, Guangshun Huang, Qingyang Shang, Kevin L. Stephans, Yahua Zhong, Peng Qi, Rahul D. Tendulkar, and Ping Xia. Alignment focus of daily image guidance for concurrent treatment of prostate and pelvic lymph nodes. *International Journal of Radiation Oncology Biology Physics*, 87(2):383–389, 2013. URL: http://dx.doi.org/10.1016/j.ijrobp.2013.06.003, doi:10.1016/j.ijrobp.2013.06.003.

[FKAEC09] Emmanouil Fokas, Gerhard Kraft, Hanxiang An, and Rita Engenhart-Cabillic. Ion beam radiobiology and cancer: Time to update ourselves. *Biochimica et Biophysica Acta (BBA) - Reviews on Cancer*, 1796(2):216–229, 2009.

[FMM16] Daniel Foley, Brendan McClean, and Peter McBride. Adaptation of daily dose using CBCT imaging. *Physica Medica*, 32(7):950, jul 2016. URL: http://linkinghub.elsevier.com/retrieve/pii/S1120179716300552, doi:10.1016/j.ejmp.2016.05.017.

[FND+15] Anna M. Flejmer, Petra Witt Nyström, Frida Dohlmar, Dan Josefsson, and Alexandru Dasu. Potential Benefit of Scanned Proton Beam versus Photons as Adjuvant Radiation Therapy in Breast Cancer. *International Journal of Particle Therapy*, 1(4):845–855, 2015. URL: http://theijpt.org/doi/10.14338/IJPT-14-00013.1, doi:10.14338/IJPT-14-00013.1.

[FRO09] Piero Fossati, Umberto Ricardi, and Roberto Orecchia. Pediatric medulloblastoma: Toxicity of current treatment and potential role of protontherapy. *Cancer Treatment Reviews*, 35(1):79–96, 2009. URL: http://linkinghub.elsevier.com/retrieve/pii/S0305737208002831, doi:10.1016/j.ctrv.2008.09.002.

[FRP+14] G Fattori, M Riboldi, A Pella, M Peroni, P Cerveri, and M Desplanques. Image guided particle therapy in CNAO room 2 : Implementation and clinical validation. *Physica Medica*, pages 1–7, 2014. URL: http://dx.doi.org/10.1016/j.ejmp.2014.10.075, doi:10.1016/j.ejmp.2014.10.075.

[FS04] Matthias FIPPEL and Martin Soukup. A Monte Carlo dose calculation algorithm for proton therapy. *Medical Physics*, 31(8):2263, 2004. URL: http://link.aip.org/link/MPHYA6/v31/i8/p2263/s1&Agg=doi, doi:10.1118/1.1769631.

[GGBC+17] V. Giacometti, S. Guatelli, M. Bazalova-Carter, A. B. Rosenfeld, and R. W. Schulte. Development of a high resolution voxelised head phantom for medical physics applications, jan 2017. URL: http://www.ncbi.nlm.nih.gov/pubmed/28108101http://www.pubmedcentral.nih.gov/articlerender.fcgi?artid=PMC5532057http://linkinghub.elsevier.com/retrieve/pii/S1120179717300078, doi:10.1016/j.ejmp.2017.01.007.

[GGZ+16] V. Giacometti, S. Guatelli, R. Zatserklyaniy, A. Johnson, H. Sadrozinski, T. Plautz, P. Piersimoni, C. Ordoñez, V. Bashkirov, A. Rosenfeld, and R. Schulte. Dosimetric Evaluation of Proton CT using a Prototype Proton CT Scanner. In *IEEE Nuclear Science Symposium and Medical Imaging Conference (NSS/MIC)*, Strasbourg, FR, 2016.

[GHG+14] Dietmar Georg, Johannes Hopfgartner, Joanna Gòra, Peter Kuess, Gabriele Kragl, Daniel Berger, Neamat Hegazy, Gregor Goldner, and Petra Georg. Dosimetric considerations to determine the optimal technique for localized prostate cancer among external photon, proton, or carbon-ion therapy and high-dose-rate or low-dose-rate brachytherapy. *International Journal of Radiation Oncology Biology Physics*, 88(3):715–722, 2014. doi:10.1016/j.ijrobp.2013.11.241.

[Gle14] Ian Gleeson. Calculation of planning margins for different verification techniques in radical prostate radiotherapy. *Journal of Radiotherapy in Practice*, 13(2):149–158, 2014. URL: http://www.embase.com/search/results?subaction=viewrecord{&}from=export{&}id=L372997817{%}5Cnhttp://dx.doi.org/10.1017/S1460396913000101{%}5Cnhttp://sfxhosted.exlibrisgroup.com/medtronic?sid=EMBASE{&}issn=14671131{&}id=doi:10.1017{%}2FS1460396913000101{&}atitle=Calculati, doi:http://dx.doi.org/10.1017/S1460396913000101.

Bibliography

[GRE11] L GREVILLOT. *Monte Carlo simulation of active scanning proton therapy system with Gate/Geant4: Towards a better patient dose quality assurance*. PhD thesis, Institut National des Sciences Appliquées de Lyon, 2011. URL: http://hal.archives-ouvertes.fr/tel-00735746/.

[GYM13] M Ghilezan, D Yan, and A Martinez. Adaptive Radiation Therapy for Prostate Cancer. *Semin Radiat Oncol*, 20(2):130–137, 2013. doi:10.1016/j.semradonc.2009.11.007.Adaptive.

[HBS12a] Roger a HALG, Jurgen Besserer, and Uwe Schneider. Systematic measurements of whole-body dose distributions for various treatment machines and delivery techniques in radiation therapy. *Medical physics*, 39(12):7662–76, December 2012. URL: http://www.ncbi.nlm.nih.gov/pubmed/23231314, doi:10.1118/1.4767773.

[HBS12b] Roger a HALG, Jurgen Besserer, and Uwe Schneider. Systematic measurements of whole-body imaging dose distributions in image-guided radiation therapy. *Medical physics*, 39(12):7650–61, December 2012. URL: http://www.ncbi.nlm.nih.gov/pubmed/23231313, doi:10.1118/1.4758065.

[HCL+16] P. Hinault, F. Compagnon, T. Lacaze, J.M. Bachaud, and E. Graulieres. 6. Adaptive radiotherapy: Evaluation of the dose actually delivered to the patient in a treatment of prostate cancer radiotherapy. *Physica Medica*, 32:344, 2016. URL: http://linkinghub.elsevier.com/retrieve/pii/S1120179716310341, doi:10.1016/j.ejmp.2016.11.057.

[HSB+12] R F Hurley, R. W. Schulte, V. A. Bashkirov, A. J. Wroe, A. Ghebremedhin, H. W. F. Sadrozinski, V. Rykalin, G. Coutrakon, P. Koss, and B. Patyal. Water-equivalent path length calibration of a prototype proton CT scanner. *Medical Physics*, 39(5):2438–2446, 2012. doi:10.1118/1.3700173.

[HUG04] EB HUG. Protons versus photons: a status assessment at the beginning of the 21st century. *Radiotherapy and Oncology*, pages 35–37, 2004. URL: http://ukpmc.ac.uk/abstract/MED/15971306.

[HVP+11] Marie a D Haverkort, Jeroen B. Van De Kamer, Bradley R. Pieters, Geertjan Van Tienhoven, Esther Assendelft, Andrea L. Lensing, Marcel Van Herk, Theo M. De Reijke, Jaap Stoker, and Caro C E Koning. Position verification for the prostate: Effect on rectal wall dose. *International Journal of Radiation Oncology Biology Physics*, 80(2):462–468, 2011. doi:10.1016/j.ijrobp.2010.02.016.

[IBA] IBA. World's first large-field-of-view Cone Beam CT for proton therapy ready for commissioning | IBA. URL: https://iba-worldwide.com/content/pt/world-s-first-large-field-view-cone-beam-ct-proton-therapy-ready-co

[JBD+16] Robert P. Johnson, Vladimir Bashkirov, Langley Dewitt, Valentina Giacometti, Robert F. Hurley, Pierluigi Piersimoni, Tia E. Plautz, Hartmut

F.-W. Sadrozinski, Keith Schubert, Reinhard Schulte, Blake Schultze, and Andriy Zatserklyaniy. A Fast Experimental Scanner for Proton CT: Technical Performance and First Experience with Phantom Scans. *IEEE Transactions on Nuclear Science*, 63(1):52–60, feb 2016. URL: http://www.ncbi.nlm.nih.gov/pubmed/27127307http://www.pubmedcentral.nih.gov/articlerender.fcgi?artid=PMC4844465http://ieeexplore.ieee.org/document/7352382/, doi:10.1109/TNS.2015.2491918.

[Jer14] Martin Jermann. Particle Therapy Statistics in 2013. *International Journal of Particle Therapy*, 1(1):40–43, 2014. URL: http://theijpt.org/doi/abs/10.14338/IJPT.14-editorial-2.1, doi:10.14338/IJPT.14-editorial-2.1.

[JMIC13] Hans J Johnson, Matt Mccormick, Luis Ibanez, and Insight Software Consortium. The ITK Software Guide Third Edition - Updated for ITK version 4.5, 2013. URL: http://itk.org/ItkSoftwareGuide.pdf.

[KDOn+13] Nicholas T. Karonis, Kirk L. Duffin, Caesar E. Ordoñez, Bela Erdelyi, Thomas D. Uram, Eric C. Olson, George Coutrakon, and Michael E. Papka. Distributed and hardware accelerated computing for clinical medical imaging using proton computed tomography (pCT). *Journal of Parallel and Distributed Computing*, 73(12):1605–1612, 2013. URL: http://dx.doi.org/10.1016/j.jpdc.2013.07.016, doi:10.1016/j.jpdc.2013.07.016.

[KHA09] Faiz M. KHAN. *The Physics of Radiation Therapy*. Wolters Kluwer | Lippincott Willians & Wilkins, Philadelphia, fourth edition, 2009.

[KKA+07] Kevin R KOZAK, Lisa a Kachnic, Judith Adams, Elizabeth M Crowley, Brian M Alexander, Harvey J Mamon, Carlos Fernandez-Del Castillo, David P Ryan, Thomas F DeLaney, and Theodore S Hong. Dosimetric feasibility of hypofractionated proton radiotherapy for neoadjuvant pancreatic cancer treatment. *International journal of radiation oncology, biology, physics*, 68(5):1557–66, August 2007. URL: http://www.ncbi.nlm.nih.gov/pubmed/17544599, doi:10.1016/j.ijrobp.2007.02.056.

[KL13] Antje-Christin Knopf and Antony Lomax. In vivo proton range verification: a review. *Physics in Medicine and Biology*, 58(15):R131–R160, aug 2013. URL: http://www.ncbi.nlm.nih.gov/pubmed/23863203http://stacks.iop.org/0031-9155/58/i=15/a=R131?key=crossref.a4dce585277cdd2c3b0331cb1d3e7322, doi:10.1088/0031-9155/58/15/R131.

[KOM+13] Motoki Kumagai, Tohru Okada, Shinichiro Mori, Susumu Kandatsu, and Hiroshi Tsuji. Evaluation of the dose variation for prostate heavy charged particle therapy using four-dimensional computed tomography. *Journal of Radiation Research*, 54(December 2012):357–366, 2013. doi:10.1093/jrr/rrs106.

Bibliography

[KPV14] Ron Kikinis, Steve D. Pieper, and Kirby G. Vosburgh. 3D Slicer: A Platform for Subject-Specific Image Analysis, Visualization, and Clinical Support. In *Intraoperative Imaging and Image-Guided Therapy*, pages 277–289. Springer New York, New York, NY, 2014. URL: http://link.springer.com/10.1007/978-1-4614-7657-3{_}19, doi:10.1007/978-1-4614-7657-3_19.

[KSM+10] Stefan Klein, Marius Staring, Keelin Murphy, Max a. Viergever, and Josien P W Pluim. Elastix: A toolbox for intensity-based medical image registration. *IEEE Transactions on Medical Imaging*, 29(1):196–205, 2010. doi:10.1109/TMI.2009.2035616.

[LBF+05] Catherine T Lee, Stephen D Bilton, Robin M Famiglietti, Beverly A Riley, Anita Mahajan, Eric L Chang, Moshe H Maor, Shiao Y Woo, James D Cox, and Alfred R Smith. Treatment planning with protons for pediatric retinoblastoma, medulloblastoma, and pelvic sarcoma: how do protons compare with other conformal techniques? *International journal of radiation oncology, biology, physics*, 63(2):362–72, oct 2005. URL: http://www.sciencedirect.com/science/article/pii/S0360301605002890, doi:10.1016/j.ijrobp.2005.01.060.

[LBH+06] Dale W. Litzenberg, James M. Balter, Scott W. Hadley, Howard M. Sandler, Twyla R. Willoughby, Patrick a. Kupelian, and Lisa Levine. Influence of intrafraction motion on margins for prostate radiotherapy. *International Journal of Radiation Oncology Biology Physics*, 65(2):548–553, 2006. doi:10.1016/j.ijrobp.2005.12.033.

[LDU+04] W H S T C LAIR, J A A Dams, M B Ues, B C F Ullerton, S E A N L A S Hell, H M K Ooy, J S L Oeffler, and N J T Arbell. Advantage of protons compared to conventional x-ray or imrt in the treatment of pediatric patient with medulloblastoma. *Int. J. Radiation Oncology Biol. Phys.*, 58(3):727–734, 2004. doi:10.1016/S0360-3016(03)01574-8.

[LDZ+15] Guillaume Landry, George Dedes, Christoph Zöllner, Josefine Handrack, Guillaume Janssens, Jonathan Orban de Xivry, Michael Reiner, Chiara Paganelli, Marco Riboldi, Florian Kamp, Matthias Söhn, Jan J Wilkens, Guido Baroni, Claus Belka, and Katia Parodi. Phantom based evaluation of CT to CBCT image registration for proton therapy dose recalculation. *Physics in Medicine and Biology*, 60(2):595–613, 2015. URL: http://stacks.iop.org/0031-9155/60/i=2/a=595?key=crossref.67d675928de6c7001f2da3c872381148, doi:10.1088/0031-9155/60/2/595.

[LHS+00] Ray L LIN, E Ugen B H Hug, Rosemary A S Schaefer, W M Iller, J Ames M S Later, and J Erry D S Later. Conformal proton radiation therapy of the posterior fossa: a study comparing prtons with three-dimensional planned photons in limiting dose to auditory structuresa. *Int. J. Radiation Oncology Biol. Phys.*, 48(4):1219–1226, 2000.

[LKP11] Áshildur Logadóttir, Stine Korreman, and Peter Meidahl Petersen. Comparison of the accuracy and precision of prostate localization with 2D-2D and 3D images. *Radiotherapy and Oncology*, 98:175–180, 2011. doi:10.1016/j.radonc.2010.11.012.

[LND+15] Guillaume Landry, Reinoud Nijhuis, George Dedes, Josefine Handrack, Christian Thieke, Guillaume Janssens, Jonathan Orban de Xivry, Michael Reiner, Florian Kamp, Jan J Wilkens, Chiara Paganelli, Marco Riboldi, Guido Baroni, Ute Ganswindt, Claus Belka, and Katia Parodi. Investigating CT to CBCT image registration for head and neck proton therapy as a tool for daily dose recalculation. *Medical physics*, 42(3):1354–66, 2015. URL: http://scitation.aip.org/content/aapm/journal/medphys/42/3/10.1118/1.4908223, doi:10.1118/1.4908223.

[LNJ+13] Yifei Lou, Tianye Niu, Xun Jia, Patricio a. Vela, Lei Zhu, and Allen R. Tannenbaum. Joint CT/CBCT deformable registration and CBCT enhancement for cancer radiotherapy. *Medical Image Analysis*, 17(3):387–400, 2013. URL: http://dx.doi.org/10.1016/j.media.2013.01.005, doi:10.1016/j.media.2013.01.005.

[Low04] David G Lowe. Distinctive Image Features from Scale-Invariant Keypoints DAVID. *International Journal of Computer Vision*, 60(2):91–110, 2004.

[LQL+13] Xiaoqiang Li, Enzhuo M. Quan, Yupeng Li, Xiaoning Pan, Yin Zhou, Xiaochun Wang, Weiliang Du, Rajat J. Kudchadker, Jennifer L. Johnson, Deborah A. Kuban, Andrew K. Lee, and Xiaodong Zhang. A fully automated method for ct-on-rails-guided online adaptive planning for prostate cancer intensity modulated radiation therapy. *International Journal of Radiation Oncology Biology Physics*, 86(5):835–841, 2013. doi:10.1016/j.ijrobp.2013.04.014.

[LZZ+08] Heng Li, X. Ronald Zhu, Lifei Zhang, Lei Dong, Sam Tung, Anesa Ahamad, K. S Clifford Chao, William H. Morrison, David I. Rosenthal, David L. Schwartz, Radhe Mohan, and Adam S. Garden. Comparison of 2D Radiographic Images and 3D Cone Beam Computed Tomography for Positioning Head-and-Neck Radiotherapy Patients. *International Journal of Radiation Oncology Biology Physics*, 71(3):916–925, 2008. doi:10.1016/j.ijrobp.2008.01.008.

[Mah14] Anita Mahajan. Proton Craniospinal Radiation Therapy: Rationale and Clinical Evidence. *International Journal of Particle Therapy*, 1(2):140822133400007, 2014. URL: http://theijpt.org/doi/abs/10.14338/IJPT.14.00005.1, doi:10.14338/IJPT.14.00005.1.

[MBC79] M. D. McKay, R. J. Beckman, and W. J. Conover. A comparison of three methods for selecting values of input variables in the analysis of output from a computer code. *Technometrics*, 21(2):239–245, 1979. URL: http://www.jstor.org/stable/1268522.

Bibliography

[MBF+14] I. F. Maund, R. J. Benson, J. Fairfoul, J. Cook, R. Huddart, and A. Poynter. Imageguided radiotherapy of the prostate using daily CBCT: The feasibility and likely benefit of implementing a margin reduction. *British Journal of Radiology*, 87(1044), 2014. doi:10.1259/bjr.20140459.

[MGJ+10] Jeff M. Michalski, Hiram Gay, Andrew Jackson, Susan L. Tucker, and Joseph O. Deasy. Radiation Dose-Volume Effects in Radiation-Induced Rectal Injury. *International Journal of Radiation Oncology Biology Physics*, 76(3 SUPPL.):123–129, 2010. doi:10.1016/j.ijrobp.2009.03.078.

[MH01] David Mattes and Dr Haynor. Nonrigid multimodality image registration. *Medical ...*, 4322:1609–1620, 2001. URL: http://dx.doi.org/10.1117/12.431046$\delimiter"026E30F$nhttp://proceedings.spiedigitallibrary.org/data/Conferences/SPIEP/35163/1609_1.pdf, doi:10.1117/12.431046.

[MHN+14] Nancy P. Mendenhall, Bradford S. Hoppe, Romaine C. Nichols, William M. Mendenhall, Christopher G. Morris, Zuofeng Li, Zhong Su, Christopher R. Williams, Joseph Costa, and Randal H. Henderson. Five-year outcomes from 3 prospective trials of image-guided proton therapy for prostate cancer. *International Journal of Radiation Oncology Biology Physics*, 88(3):596–602, 2014. URL: http://dx.doi.org/10.1016/j.ijrobp.2013.11.007, doi:10.1016/j.ijrobp.2013.11.007.

[MOL47] G MOLIÈRE. Theorie der streuung schneller geladener teilchen.i. einzelstreuung am abgeschirmten coulomb-feld. ii. mehrfach undd vielfachstreuung. *Z. Naturforsch. A*, 2:133–145, 1947.

[MST+11] Yuki MIYABE, Akira Sawada, Kenji Takayama, Shuji Kaneko, Takashi Mizowaki, Masaki Kokubo, and Masahiro Hiraoka. Positioning accuracy of a new image-guided radiotherapy system. *Medical Physics*, 38(5):2535, 2011. URL: http://link.aip.org/link/MPHYA6/v38/i5/p2535/s1&Agg=doi, doi:10.1118/1.3578607.

[MTC+09] Reshma Munbodh, Hemant D Tagare, Zhe Chen, David a Jaffray, Douglas J Moseley, Jonathan P S Knisely, and James S Duncan. 2D-3D registration for prostate radiation therapy based on a statistical model of transmission images. *Medical physics*, 36:4555–4568, 2009. doi:10.1118/1.3213531.

[MYJ+10] Lawrence B Marks, Ellen D Yorke, Andrew Jackson, Randall K Ten Haken, Louis S Constine, Avraham Eisbruch, Søren M Bentzen, Jiho Nam, and Joseph O Deasy. Use of Normal Tissue Complication Probability Models in the Clinic. *International Journal of Radiation Oncology Biology Physics*, 76(3 SUPPL.):S10–9, mar 2010. URL: http://linkinghub.elsevier.com/retrieve/pii/S036030160903288Xhttp://www.ncbi.nlm.nih.gov/pubmed/20171502http://www.pubmedcentral.nih.gov/articlerender.fcgi?artid=PMC4041542, doi:10.1016/j.ijrobp.2009.07.1754.

[NHD+02] Aart J. Nederveen, Uulke a Van Der Heide, Homan Dehnad, R. JeroenA Van Moorselaar, Pieter Hofman, and Jan J W Lagendijk. Measurements and clinical consequences of prostate motion during a radiotherapy fraction. *International Journal of Radiation Oncology Biology Physics*, 53(1):206–214, 2002. doi:10.1016/S0360-3016(01)02823-1.

[NHP+12] Romaine C NICHOLS, Soon N Huh, D Ph, Karl L Prado, Byong Y Yi, Navesh K Sharma, Meng W Ho, Bradford S Hoppe, Nancy P Mendenhall, Zuofeng Li, D Sc, William F Regine, and M D. Protons offer reduced normal-tissue exposure for patients receiving postoperative radiotherapy for resected pancreatic head cancer. *Radiation Oncology Biology*, 83(1):158–163, 2012. URL: http://dx.doi.org/10.1016/j.ijrobp.2011.05.045, doi:10.1016/j.ijrobp.2011.05.045.

[NSF15] O Barbosa Neto, L Souhami, and S Faria. Hypofractionated radiation therapy for prostate cancer : The McGill University Health Center experience Radiothérapie hypofractionnée pour le cancer de la prostate : expérience du centre universitaire de santé McGill. *Cancer / Radiotherapie*, 19(6-7):431–436, 2015. URL: http://dx.doi.org/10.1016/j.canrad.2015.05.015, doi:10.1016/j.canrad.2015.05.015.

[PAE15] G Poludniowski, N M Allinson, and P M Evans. Proton radiography and tomography with application to proton therapy, sep 2015. URL: http://www.ncbi.nlm.nih.gov/pubmed/26043157http://www.pubmedcentral.nih.gov/articlerender.fcgi?artid=PMC4743570http://www.birpublications.org/doi/10.1259/bjr.20150134, doi:10.1259/bjr.20150134.

[Pag12] H Paganetti. *Proton therapy physics (Series in medical physics and biomedical engineering)*. Lavoisier, 2012. URL: http://www.lavoisier.fr/livre/notice.asp?id=RK2W6SA2XKKOWQ.

[Par14] K. Parodi. Heavy ion radiography and tomography. *Physica Medica*, 30(5):539–543, 2014. URL: http://dx.doi.org/10.1016/j.ejmp.2014.02.004, doi:10.1016/j.ejmp.2014.02.004.

[PBG+16] Tia E Plautz, V Bashkirov, V Giacometti, R F Hurley, R P Johnson, P Piersimoni, W Sadrozinski, R W Schulte, and A Zatserklyaniy. An evaluation of spatial resolution of a prototype proton CT scanner. *Medical Physics Med. Phys*, 43(36), 2016. URL: http://dx.doi.org/10.1118/1.4966028http://scitation.aip.org/content/aapm/journal/medphys/43/12?ver=pdfcov, doi:10.1118/1.3096706.

[PC15] Scott Penfold and Yair Censor. Techniques in Iterative Proton CT Image Reconstruction. 2015. URL: http://arxiv.org/abs/1510.08559http://dx.doi.org/10.1007/s11220-015-0122-3, arXiv:1510.08559, doi:10.1007/s11220-015-0122-3.

Bibliography

[Per11] Marta Peroni. Methods and algorithms for image guided adaptive radio- and hadron- therapy. 2011. URL: https://www.politesi.polimi.it/handle/10589/56740.

[PET92] P. L. PETTI. Differential-pencil-beam dose calculations for charged particles. *Medical Physics*, 19:137–149, January 1992. doi:10.1118/1.596887.

[PFC+13] Nita Patel, Sergio Faria, Fabio Cury, Marc David, Marie Duclos, George Shenouda, Russell Ruo, and Luis Souhami. Hypofractionated Radiation Therapy (66 Gy in 22 Fractions at 3 Gy per Fraction) for Favorable-Risk Prostate Cancer: Long-term Outcomes. *International Journal of Radiation Oncology*Biology*Physics*, 86(3):534–539, 2013. URL: http://linkinghub.elsevier.com/retrieve/pii/S0360301613001715, doi:10.1016/j.ijrobp.2013.02.010.

[PKL+10] Jean L. Peng, Darren Kahler, Jonathan G. Li, Sanjiv Samant, Guanghua Yan, Robert Amdur, and Chihray Liu. Characterization of a real-time surface image-guided stereotactic positioning system. *Medical Physics*, 37(10):5421–5433, 2010. URL: http://doi.wiley.com/10.1118/1.3483783, doi:10.1118/1.3483783.

[PMC+13] Thomas J. Pugh, Mark F. Munsell, Seungtaek Choi, Quyhn Nhu Nguyen, Benson Mathai, X. Ron Zhu, Narayan Sahoo, Michael Gillin, Jennifer L. Johnson, Richard a. Amos, Lei Dong, Usama Mahmood, Deborah a. Kuban, Steven J. Frank, Karen E. Hoffman, Sean E. McGuire, and Andrew K. Lee. Quality of life and toxicity from passively scattered and spot-scanning proton beam therapy for localized prostate cancer. *International Journal of Radiation Oncology Biology Physics*, 87(5):946–953, 2013. URL: http://dx.doi.org/10.1016/j.ijrobp.2013.08.032, doi:10.1016/j.ijrobp.2013.08.032.

[PPP+07] M. Esmeralda Ramos Poli, William Parker, Horacio Patrocinio, Luis Souhami, George Shenouda, Leticia Lucente Campos, and Ervin B. Podgorsak. An Assessment of PTV Margin Definitions for Patients Undergoing Conformal 3D External Beam Radiation Therapy for Prostate Cancer Based on an Analysis of 10,327 Pretreatment Daily Ultrasound Localizations. *International Journal of Radiation Oncology Biology Physics*, 67(5):1430–1437, 2007. doi:10.1016/j.ijrobp.2006.11.004.

[PPR+13] Chiara Paganelli, Marta Peroni, Marco Riboldi, Gregory C Sharp, Delia Ciardo, Daniela Alterio, Roberto Orecchia, and Guido Baroni. Scale invariant feature transform in adaptive radiation therapy: a tool for deformable image registration assessment and re-planning indication. *Physics in medicine and biology*, 58:287–99, 2013. URL: http://www.ncbi.nlm.nih.gov/pubmed/23257263, doi:10.1088/0031-9155/58/2/287.

[PSCR10] S N Penfold, R W Schulte, Y Censor, and a B Rosenfeld. Total variation superiorization schemes in proton computed tomography image reconstruction. *Medical physics*, 37:5887–5895, 2010. arXiv:1010.1663, doi:10.1118/1.3504603.

[PSM+10] Scott N Penfold, Reinhard W Schulte, Scott Mcallister, Keith E Schubert, and Anatoly B Rosenfeld. Block-Iterative and String-Averaging Projection Algorithms in Proton Computed Tomography Image Reconstruction. Technical report, University of Wollogong, 2010.

[QSLY15] An Qin, Ying Sun, Jian Liang, and Di Yan. Evaluation of online/offline image guidance/adaptation approaches for prostate cancer radiation therapy. *International Journal of Radiation Oncology Biology Physics*, 91(5), 2015. doi:10.1016/j.ijrobp.2014.12.043.

[RAZ+16] Adam C. Riegel, Jeffrey G. Antone, Honglai Zhang, Prachi Jain, Jagdeep Raince, Anthony Rea, Angelo M. Bergamo, Ajay Kapur, and Louis Potters. Deformable image registration and interobserver variation in contour propagation for radiation therapy planning. *Journal of Applied Clinical Medical Physics*, 17(3), 2016.

[RCZ+14] Suresh Rana, ChihYao Cheng, Yuanshui Zheng, Dina Risalvato, Nancy Cersonsky, Eric Ramirez, Li Zhao, Gary Larson, and Carlos Vargas. Proton Therapy vs. VMAT for Prostate Cancer: A Treatment Planning Study. *International Journal of Particle Therapy*, 1(1):22–33, 2014. URL: http://theijpt.org/doi/abs/10.14338/IJPT.13-00003.1, doi:10.14338/IJPT.13-00003.1.

[RDM+12] Barbara ROMBI, Thomas F DeLaney, Shannon M MacDonald, Mary S Huang, David H Ebb, Norbert J Liebsch, Kevin a Raskin, Beow Y Yeap, Karen J Marcus, Nancy J Tarbell, and Torunn I Yock. Proton radiotherapy for pediatric ewing's sarcoma: initial clinical outcomes. *International journal of radiation oncology, biology, physics*, 82(3):1142–8, March 2012. URL: http://www.ncbi.nlm.nih.gov/pubmed/21856094, doi:10.1016/j.ijrobp.2011.03.038.

[RPH+15] Ihab S Ramadaan, Karsten Peick, David a Hamilton, Jamie Evans, Douglas Iupati, Anna Nicholson, Lynne Greig, and Robert J W Louwe. Validation of Varian's SmartAdapt® deformable image registration algorithm for clinical application. *Radiation Oncology*, 10(1):73, 2015. doi:10.1186/s13014-015-0372-1.

[RRLV02] Peter Remeijer, Coen Rasch, Joos V. Lebesque, and Marcel Van Herk. Margins for translational and rotational uncertainties: A probability-based approach. *International Journal of Radiation Oncology Biology Physics*, 53(2):464–474, 2002. doi:10.1016/S0360-3016(02)02749-9.

[RSC+15] Bastien Rigaud, Antoine Simon, Joël Castelli, Maxime Gobeli, Juan David Ospina Arango, Guillaume Cazoulat, Olivier Henry, Pascal Haigron, and Renaud De Crevoisier. Evaluation of deformable image registration methods for dose monitoring in head and neck radiotherapy. *BioMed Research International*, 2015, 2015. doi:10.1155/2015/726268.

Bibliography

[RT14] Barbara Rombi and Beate Timmermann. Proton Beam Therapy for Pediatric Chordomas: State of the Art. *International Journal of Particle Therapy*, 1(2):368–385, 2014. URL: http://theijpt.org/doi/abs/10.14338/IJPT.13.00008.1, doi:10.14338/IJPT.13.00008.1.

[SAB+04] W H St Clair, J A Adams, M Bues, B C Fullerton, Sean La Shell, H M Kooy, J S Loeffler, and N J Tarbell. Advantage of protons compared to conventional X-ray or IMRT in the treatment of a pediatric patient with medulloblastoma. *International journal of radiation oncology, biology, physics*, 58(3):727–34, mar 2004. URL: http://www.sciencedirect.com/science/article/pii/S0360301603015748, doi:10.1016/S0360-3016(03)01574-8.

[SBB+03] H.F.-W. SANDROZINSKI, V. Bashkirov, M. Bruzzi, L.R. Johnson, B. Keeney, G. Ross, R.W. Schulte, a. Seiden, K. Shahnazi, D.C. Williams, and L. Zhang. Issues in Proton Computed Tomography. *Nuclear Instruments and Methods in Physics Research Section A: Accelerators, Spectrometers, Detectors and Associated Equipment*, 511(1-2):275–281, September 2003. URL: http://linkinghub.elsevier.com/retrieve/pii/S0168900203018060, doi:10.1016/S0168-9002(03)01806-0.

[SBL+04a] R. SCHULTE, V. Bashkirov, T. Li, Z. Liang, K. Mueller, J. Heimann, L.R. Johnson, B. Keeney, H.F.W. Sadrozinski, A. Seiden, D. C. Willliams, L. Zhang, Z. Li, S. Peggs, T. Satogata, and C. Woody. Conceptual design of a proton computed tomography system for applications in proton radiation therapy. *IEEE Trans.Nuclear Sciencer*, 2004.

[SBL+04b] Reinhard Schulte, Vladimir Bashkirov, Tianfang Li, Zhengrong Liang, Klaus Mueller, Jason Heimann, Leah R Johnson, Brian Keeney, Hartmut F Sadrozinski, Abraham Seiden, David C Williams, Lan Zhang, Zhang Li, Steven Peggs, Todd Satogata, and Craig Woody. Conceptual Design of a Proton Computed Tomography System for Applications in Proton Radiation Therapy. 51(3):866–872, 2004.

[SBMT09] J R Sykes, D S Brettle, D R Magee, and D I Thwaites. Investigation of uncertainties in image registration of cone beam CT to CT on an image-guided radiotherapy system. *Physics in medicine and biology*, 54:7263–7283, 2009. doi:10.1088/0031-9155/54/24/002.

[SCH11] M. SCHWARZ. Treatment planning in proton therapy. *The European Physical Journal Plus*, 126(7):67, July 2011. URL: http://www.springerlink.com/index/10.1140/epjp/i2011-11067-y, doi:10.1140/epjp/i2011-11067-y.

[SDG+10] Herman SUIT, Thomas DeLaney, Saveli Goldberg, Harald Paganetti, Ben Clasie, Leo Gerweck, Andrzej Niemierko, Eric Hall, Jacob Flanz, Josh Hallman, and Alexei Trofimov. Proton vs carbon ion beams in the definitive radiation treatment of cancer patients. *Radiotherapy and oncology : journal of the European Society for Therapeutic Radiology and Oncology*, 95(1):3–22, April

2010. URL: http://www.ncbi.nlm.nih.gov/pubmed/20185186, doi:10.1016/j.radonc.2010.01.015.

[SH02] Joep C. Stroom and B. J M Heijmen. Geometrical uncertainties, radiotherapy planning margins, and the ICRU-62 report. *Radiotherapy and Oncology*, 64:75–83, 2002. doi:10.1016/S0167-8140(02)00140-8.

[SHR+14] J. Scaife, K. Harrison, M. Romanchikova, A. Parker, M. Sutcliffe, S. Bond, S. Thomas, S. Freeman, R. Jena, A. Bates, and N. Burnet. Random variation in rectal position during radiotherapy for prostate cancer is two to three times greater than that predicted from prostate motion. *British Journal of Radiology*, 87(1042), 2014. doi:10.1259/bjr.20140343.

[SJM+13] H. F W Sadrozinski, R. P. Johnson, S. MacAfee, A. Plumb, D. Steinberg, A. Zatserklyaniy, V. A. Bashkirov, R. F. Hurley, and R. W. Schulte. Development of a head scanner for proton CT. In *Nuclear Instruments and Methods in Physics Research, Section A: Accelerators, Spectrometers, Detectors and Associated Equipment*, 2013. doi:10.1016/j.nima.2012.04.029.

[SKB+14] Cody D Schlaff, Andra Krauze, Arnaud Belard, John J O'Connell, and Kevin a Camphausen. Bringing the heavy: carbon ion therapy in the radiobiological and clinical context. *Radiation oncology (London, England)*, 9(1):88, 2014. URL: http://www.pubmedcentral.nih.gov/articlerender.fcgi?artid=4002206&tool=pmcentrez&rendertype=abstract, doi:10.1186/1748-717X-9-88.

[SLM+14] Jerry M. Slater, Ted C. Ling, Rachel Mifflin, Prashanth Nookala, Roger Grove, Anh M. Ly, Baldev Patyal, Jerry D. Slater, and Gary Y. Yang. Protons Offer Reduced Tissue Exposure for Patients Receiving Radiation Therapy for Pancreatic Cancer. *International Journal of Particle Therapy*, 1(3):702–710, 2014. URL: http://theijpt.org/doi/abs/10.14338/IJPT-14-00008.1, doi:10.14338/IJPT-14-00008.1.

[SM16] Marco Schwarz and Silvia Molinelli. What can particle therapy add to the treatment of prostate cancer? *Physica Medica*, 32(3):485–491, 2016. URL: http://dx.doi.org/10.1016/j.ejmp.2016.03.017, doi:10.1016/j.ejmp.2016.03.017.

[SML96] Will Schroeder, Kenneth Martin, and Bill Lorensen. *The Visualization Toolkit: An Object-Oriented Approach to 3-D Graphics*. 1996. URL: https://www.researchgate.net/profile/William{_}Schroeder3/publication/200034772{_}The{_}Visualization{_}Toolkit{_}An{_}Object-Oriented{_}links/57dfcfa708ae1dcfea865e57/The-Visualization-Toolkit-An-Object.pdf.

[SPTS08] R. W. Schulte, S. N. Penfold, J. T. Tafas, and K. E. Schubert. A maximum likelihood proton path formalism for application in proton computed tomography. *Medical Physics*, 35(11):4849–4856, 2008. arXiv:1312.3977, doi:10.1118/1.2986139.

Bibliography

[SSV+12a] James a Shackleford, Nadya Shusharina, Joost Verberg, Brian Winey, Markus Neuner, Philipp Steininger, Polina Golland, Yifei Lou, Chiara Paganelli, Marta Peroni, Marco Riboldi, Guido Baroni, Paolo Zaffino, Maria Francesca Spadea, Aditya Apte, Ziad Saleh, Joseph O Deasy, and Shinichro Mori. Plastimatch 1 . 6 ? Current Capabilities and Future Directions. (January), 2012.

[SSV+12b] JamesA Shackleford, Nadya Shusharina, Joost Verberg, Guy Warmerdam, Brian Winey, Markus Neuner, Philipp Steininger, Amelia Arbisser, Polina Golland, Yifei Lou, Chiara Paganelli, Marta Peroni, Marco Riboldi, Guido Baroni, Paolo Zaffino, MariaFrancesca Spadea, Aditya Apte, Ziad Saleh, JosephO Deasy, Shinichro Mori, Nagarajan Kandasamy, and GregoryC Sharp. Plastimatch 1.6 - current capabilities and future directions. *Int Conf Med Image Comput Comput Assist Interv*, 15(WS), 10 2012.

[STA+16] Ziad Saleh, Maria Thor, Aditya P Apte, Gregory Sharp, Xiaoli Tang, Harini Veeraraghavan, Ludvig Muren, and Joseph Deasy. A multiple-image-based method to evaluate the performance of deformable image registration in the pelvis. *Physics in Medicine and Biology*, 61(16):6172–6180, 2016. URL: http://stacks.iop.org/0031-9155/61/i=16/a=6172?key=crossref.05fd3d15ac2acfe792bb31f9537f2ed6, doi:10.1088/0031-9155/61/16/6172.

[TBM+14] Rachel Tuohy, Courtney Bosse, Panayiotis Mavroidis, Zheng Shi, Richard Crownover, Niko Papanikolaou, and Sotirios Stathakis. Deformable image and dose registration evaluation using two commercial programs. *International Journal of Cancer Therapy and Oncology*, 2(2), 2014.

[THT+16] Sara Thörnqvist, Liv B Hysing, Laura Tuomikoski, Anne Vestergaard, Kari Tanderup, Ludvig P Muren, and Ben J M Heijmen. Adaptive radiotherapy strategies for pelvic tumors - a systematic review of clinical implementations. *Acta oncologica (Stockholm, Sweden)*, (April):1–16, 2016. URL: http://www.tandfonline.com/doi/full/10.3109/0284186X.2016.1156738, doi:10.3109/0284186X.2016.1156738.

[TKSN14] H Tsujii, T Kamada, T Shirai, and K Noda. *Carbon-Ion Radiotherapy, principles, practices and treatment planning*. Springer, 2014.

[TX10] Robert D. Timmerman and Lei. Xing. *Image-guided and adaptive radiation therapy*. Lippincott Williams & Wilkins/Wolters Kluwer Health, 2010.

[VAA15] Catarina Veiga, Jailan Alshaikhi, and Richard Amos. Cone-Beam Computed Tomography and Deformable Registration-Based ' Dose of the Day " Calculations for Adaptive Proton Therapy. *International Journal of Particle Therapy*, 2(2):1–11, 2015. doi:10.14338/IJPT-14-00024.1.

[Van04] Marcel Van Herk. Errors and Margins in Radiotherapy. *Seminars in Radiation Oncology*, 14(1):52–64, 2004. doi:10.1053/j.semradonc.2003.10.003.

[VJT+16] Catarina Veiga, Guillaume Janssens, Ching-Ling Teng, Thomas Baudier, Lucian Hotoiu, Jamie R. McClelland, Gary Royle, Liyong Lin, Lingshu Yin, James Metz, Timothy D. Solberg, Zelig Tochner, Charles B. Simone, James McDonough, and Boon-Keng Kevin Teo. First Clinical Investigation of Cone Beam Computed Tomography and Deformable Registration for Adaptive Proton Therapy for Lung Cancer. *International Journal of Radiation Oncology*Biology*Physics*, 95(1):549–559, 2016. URL: http://www.sciencedirect.com/science/article/pii/S0360301616001085, doi:10.1016/j.ijrobp.2016.01.055.

[VMM+14] Catarina Veiga, Jamie McClelland, Syed Moinuddin, Ana Lourenço, Kate Ricketts, James Annkah, Marc Modat, Sébastien Ourselin, Derek D'Souza, and Gary Royle. Toward adaptive radiotherapy for head and neck patients: Feasibility study on using CT-to-CBCT deformable registration for "dose of the day" calculations. *Medical physics*, 41(2014):031703, 2014. URL: http://www.ncbi.nlm.nih.gov/pubmed/24593707, doi:10.1118/1.4864240.

[WHO17] World Health Organization WHO. WHO | Cancer, 2017. URL: http://www.who.int/mediacentre/factsheets/fs297/en/.

[Wil04] D C Williams. The most likely path of an energetic charged particle through a uniform medium. *Physics in Medicine & Biology*, 49(13):2899, jul 2004. URL: http://www.ncbi.nlm.nih.gov/pubmed/15285255http://stacks.iop.org/0031-9155/49/i=13/a=010, doi:10.1088/0031-9155/49/13/010.

[WLC+98] Chong Jong Wang, Stephen Wan Leung, Hui Chun Chen, Li Min Sun, Fu Min Fang, Eng Yen Huang, Ching Yeh Hsiung, and Chan Chao Changchien. The correlation of acute toxicity and late rectal injury in radiotherapy for cervical carcinoma: Evidence suggestive of consequential late effect (CQLE). *International Journal of Radiation Oncology Biology Physics*, 40(1):85–91, jan 1998. URL: http://www.ncbi.nlm.nih.gov/pubmed/9422562, doi:10.1016/S0360-3016(97)00560-9.

[WMT12] Dongxu WANG, T Rockwell Mackie, and Wolfgang a Tome. On proton CT reconstruction using MVCT-converted virtual proton projections. *Medical physics*, 39(6):2997–3008, June 2012. URL: http://www.ncbi.nlm.nih.gov/pubmed/22755684, doi:10.1118/1.4711752.

[WS01] W WIESZCZYCKA and W Scharf. *Proton radiotherapy accelerators*. World Scientific Publishing Co. Pte. Ltd., 2001. URL: http://www.worldscientific.com/doi/pdf/10.1142/9789812811646_0001.

[WSPB10] Marcin Wierzbicki, Bryan Schaly, Terry Peters, and Rob Barnett. Automatic image guidance for prostate IMRT using low dose CBCT. *Medical physics*, 37:3677–3686, 2010. doi:10.1118/1.3446800.

Bibliography

[YAL+02] Terry S Yoo, Michael J Ackerman, William E Lorensen, Will Schroeder, Vikram Chalana, Stephen Aylward, Dimitris Metaxas, and Ross Whitaker. Engineering and algorithm design for an image processing Api: a technical report on ITK–the Insight Toolkit. *Studies in health technology and informatics*, 85:586–592, 2002. doi:10.3233/978-1-60750-929-5-586.

[YLA+14] Chengliang Yang, Feng Liu, Ergun Ahunbay, Yu Wen Chang, Colleen Lawton, Christopher Schultz, Dian Wang, Selim Firat, Beth Erickson, and X. Allen Li. Combined online and offline adaptive radiation therapy: A dosimetric feasibility study. *Practical Radiation Oncology*, 4(1):e75–e83, 2014. URL: http://dx.doi.org/10.1016/j.prro.2013.02.012, doi:10.1016/j.prro.2013.02.012.

[YSF+05] Torunn YOCK, Robert Schneider, Alison Friedmann, Judith Adams, Barbara Fullerton, and Nancy Tarbell. Proton radiotherapy for orbital rhabdomyosarcoma: clinical outcome and a dosimetric comparison with photons. *International journal of radiation oncology, biology, physics*, 63(4):1161–8, November 2005. URL: http://www.ncbi.nlm.nih.gov/pubmed/15950401, doi:10.1016/j.ijrobp.2005.03.052.

[ZGX12] Qingsong Zhu, Jia Gu, and Yaoqin Xie. Deformable Image Registration with Inclusion of Autodetected Homologous Tissue Features. *The Scientific World Journal*, 2012:1–8, 2012. URL: http://www.hindawi.com/journals/tswj/2012/913693/, doi:10.1100/2012/913693.

[ZIE99] J F ZIEGLER. The stopping of energetic light ions in elemental matte. *Journal of Applied Physics*, 1272:1249–1272, 1999.

[ZP08] Christina ZACHARATOU JARLSKOG and Harald Paganetti. Physics Settings for Using the Geant4 Toolkit in Proton Therapy. *IEEE Transactions on Nuclear Science*, 55(3):1018–1025, June 2008. URL: http://ieeexplore.ieee.org/lpdocs/epic03/wrapper.htm?arnumber=4545238, doi:10.1109/TNS.2008.922816.